

Piezoelectric Nanostructures - Synthesis, Alignment, and Electrical Response to Strain

A DISSERTATION
SUBMITTED TO THE FACULTY OF THE
UNIVERSITY OF MINNESOTA
BY

Ren Zhu

IN PARTIAL FULFILLMENT OF THE REQUIREMENTS
FOR THE DEGREE OF
DOCTOR OF PHILOSOPHY

Adviser: Dr. Rusen Yang

May 2015

© Ren Zhu 2015

Acknowledgements

First of all, I would like to thank my advisor, Professor Rusen Yang, for his unconditional support throughout my Ph.D. study. I did not have much research experience before joining his group. Professor Yang has been providing me with guidance on every aspect of the research in great details and patience, from synthesizing nanostructures, configuring electrical measurement, and selecting fabrication processes, to writing papers, giving technical presentations, and networking with people in academia. In addition, Professor Yang is enthusiastic, and his energy and encouragement has helped me get through many hard times in the past five years. Without his help I would not be able to make an original contribution to this research field.

I am also grateful to my colleagues in the group - Dr. Chao Li, Mr. Wengui Zhang, Mr. Vu Nguyen, Mr. Yicong Lai, and Mr. Kory Jenkins. We have been collaborating in many projects, and I am always amazed on how everyone has his or her unique expertise and perspective and therefore could contribute to different parts of the project.

Of course, I would not be able to work on those exciting projects without the financial support from the Department of Mechanical Engineering at the University of Minnesota and the National Science Foundation.

Finally, I would like to thank my parents, Mr. Yuepin Zhu and Mrs. Yajun Zhang, and my beloved Miss Lujie Zhi. Although they are far away in China, they have been keeping me company and holding me up.

Abstract

Piezoelectric nanostructures can convert mechanical deformation into electrical signal, and have applications in mechanical energy harvesting and strain sensing. While nanostructures have unique advantages compared with bulk materials, their synthesis and assembly are more challenging, and their response to mechanical deformation is complex.

The objective of this research is to have a better control and a deeper understanding of piezoelectric nanostructures. The synthesis and assembly processes will be improved, and the electrical response to strain will be studied in details.

First, a new method to synthesize piezoelectric nanostructures is developed. Growth of nanostructures is similar to that of grasses - from the bottom up. Controlling the growth orientation is important for the optimization of device performance, and requires a highly engineered substrate in general. In this research, a textured polycrystalline film is used as an inexpensive substrate to fulfill that requirement. The textured film is coated conformally on various surface topographies and allows the epitaxial growth of nanostructures with vertical, tilted, or lateral orientations. The textured film can also be formed into three-dimensional structure for growing novel nanostructures.

Second, a new method to organize piezoelectric nanostructures is developed. Alignment and transfer of a large quantity of nanostructures at the same time is a critical step in the fabrication of energy harvesters, and has been achieved in this work through a *Spinning-Langmuir-Film* technique. In this method, a surfactant-enhanced shear flow aligns inorganic and organic nanostructures, which could be easily transferred to other

substrates and ready for device fabrication in less than 20 minutes. The areal density of the align nanostructures can be controlled in a wide range. Various factors that may affect the alignment process are studied systematically.

Third, a special type of piezoelectric nanostructures with semiconductivity is investigated in depth for the application in strain sensing. Mechanical strain induces multiple changes in the electrical property of those materials simultaneously - a *piezoresistive effect* from the semiconductor band structure change, and a *piezotronic effect* from the coupling between the piezoelectric polarization and the semiconductor interface. A general method to separate the piezotronic and piezoresistive effects is reported in this thesis based on modified four-point measurements. The piezotronic effect is found to be more sensitive to strain than the piezoresistive effect. Under a fixed bias, a 0.25% tensile strain can lead to a five-fold increase in the current through the piezotronic effect.

Table of Contents

LIST OF TABLES	VI
LIST OF FIGURES	VII
CHAPTER 1. INTRODUCTION	1
1.1. Piezoelectricity.....	1
1.2. Piezoelectric nanomaterials	2
1.3. Application of piezoelectric nanomaterials	4
1.4. Motivation.....	8
1.5. Thesis Contribution.....	11
CHAPTER 2. SYNTHESIS OF ZINC OXIDE NANOWIRES WITH UNIFORM ALIGNMENT AND ORIENTATION CONTROL	13
2.1. Introduction.....	13
2.2. Growth and characterization of a textured ZnO film.....	16
2.3. Epitaxial synthesis of ZnO nanowires	20
2.4. Tilted and lateral nanowires.....	24
2.5. Complex nanostructures.....	29
2.6. Discussion and future work	32
CHAPTER 3. ALIGNMENT AND TRANSFER OF NANOWIRES IN A SPINNING LANGMUIR FILM	37
3.1. Introduction.....	37
3.2. Overview of the alignment procedure.....	40
3.3. Alignment of piezoelectric nanowires	42
3.4. Control of array density	45
3.5. Effect of receiving substrates.....	47
3.6. Effect of surfactant.....	49
3.7. Effect of spin speed and spin duration.....	53
3.8. Discussion and future work	57

CHAPTER 4. SEPARATION OF THE PIEZOTRONIC EFFECT AND THE PIEZORESISTIVE EFFECT.....	64
4.1. Introduction.....	64
4.2. Principle.....	67
4.3. Device fabrication.....	68
4.4. Measurement system.....	73
4.5. Piezoresistive effect of ZnO nanowires.....	74
4.6. Isolation of the piezotronic effect.....	77
4.7. Finite element analysis of embedded nanowires.....	80
4.8. Discussion and future work.....	83
CHAPTER 5. CONCLUSION.....	89
REFERENCES.....	92
APPENDIX.....	101
A. MATLAB code for image processing in Chapter 3.....	101

List of Tables

Table 2-1. Process parameters of the tube furnace during the CVD synthesis.....	21
Table 4-1. Device fabrication procedure in details.....	73
Table 4-2. Mechanical properties of ZnO and polymer used in the finite element analysis.	81

List of Figures

Figure 1-1. Charge generation on a piezoelectric material under different strain conditions.	1
Figure 1-2. Scanning electron microscopy (SEM) images of piezoelectric nanowires.	2
Figure 1-3. Schematic diagram of an energy harvester based on piezoelectric nanowires encapsulated in polymer.	5
Figure 1-4. Principle of the piezotronic effect and its application.	7
Figure 1-5. Alignment of piezoelectric nanowires for energy harvesting.	10
Figure 1-6. Schematic diagram showing the combination of two piezotronic effects and a piezoresistive effect in a typical current-voltage measurement.	11
Figure 2-1. Wurtzite crystal structure of ZnO.	13
Figure 2-2. Epitaxial growth of ZnO nanowires on various single crystals.	15
Figure 2-3. Hydrothermal growth of ZnO nanorods.	17
Figure 2-4. SEM images of the textured ZnO film and the spatial confinement effect.	18
Figure 2-5. XRD characterization of the textured ZnO film.	19
Figure 2-6. CVD system.	21
Figure 2-7. CVD synthesis of ZnO nanowires.	23
Figure 2-8. Tilted growth of ZnO nanowire arrays.	26
Figure 2-9. KOH etching on (110) silicon to produce a vertical wall.	27
Figure 2-10. Lateral growth of ZnO nanowire arrays.	29
Figure 2-11. Nanowire growth on self-supported 3D textured film.	31
Figure 2-12. A possible design of a CVD system that can supply zinc vapor and oxygen vapor independently.	34
Figure 2-13. Thick wires with a thin segment on the tip, obtained in a single growth.	35
Figure 3-1. Examples of nanowire alignment in the literature.	37
Figure 3-2. Schematic illustration of the alignment process.	41
Figure 3-3. The PTFE funnel with a valve at the bottom.	42

Figure 3-4. Alignment of one-dimensional nanostructures.	44
Figure 3-5. Aligned nanotubes with different areal densities through compression.	46
Figure 3-6. Relatively high-density arrays obtained by two different methods.	47
Figure 3-7. FF PNT transferred onto different types of substrates after the alignment....	49
Figure 3-8. Shear effect on the nanotubes alignment.	51
Figure 3-9. Atomic Force Microscope images of the silicon surface.	52
Figure 3-10. Electrical test of aligned nanostructure after baking.....	53
Figure 3-11. Alignment of FF PNT with different spin speeds.	54
Figure 3-12. Nanotube array after different durations of spinning.....	56
Figure 3-13. “Stick-slip” behavior of the contact line when the water surface is descending.	58
Figure 3-14. The alignment of nanotubes on the entire water surface.....	62
Figure 3-15. Shear flow induced by a PTFE belt to provide unidirectional alignment. ...	63
Figure 4-1. SEM images of ZnO nanowire strain sensors in the literature.....	65
Figure 4-2. Current-voltage curves of a ZnO nanowire strain sensor under different strain conditions in the literature.	66
Figure 4-3. Schematic diagram of a four-point measurement circuit.	67
Figure 4-4. SEM images of ultra-long ZnO nanowires synthesized by CVD.	69
Figure 4-5. Fabrication of the multi-terminal device with a ZnO nanowire.....	70
Figure 4-6. Characterization of the SU-8 lifting layer.	71
Figure 4-7. Optical microscope image of a final device.	72
Figure 4-8. Measurement setup.....	74
Figure 4-9. Measurement of the piezoresistive effect in devices with Ohmic contacts. ..	75
Figure 4-10. Comparison of the piezotronic effect and the piezoresistive effect in devices with barrier contacts.....	78
Figure 4-11. Simulation of the non-uniform strain in ZnO nanowires.	82
Figure 4-12. A photoresist with undercut is desired for metal liftoff.	84

Figure 4-13. Damage on polymer caused by oxygen plasma.	86
Figure 4-14. Normal strain along the central axis of the polymer matrix and the embedded nanowire.....	88

CHAPTER 1. INTRODUCTION

1.1. Piezoelectricity

Piezoelectricity exists in crystalline materials without a centrosymmetry in the crystal structure. Figure 1-1 presents an archetypal piezoelectric crystal, in which a tensile or compressive strain separates the center of positive charges and the center of negative charges, inducing polarization charges on the surface of the material. Common piezoelectric materials include: (1) polycrystalline ceramics, such as barium titanate and lead zirconate titanate (PZT); (2) single crystals, such as quartz and lithium niobate; and (3) polymers, such as polyvinylidene fluoride (PVDF) and its copolymers. Some biological tissues like bone and wood also show weak piezoelectricity [1].

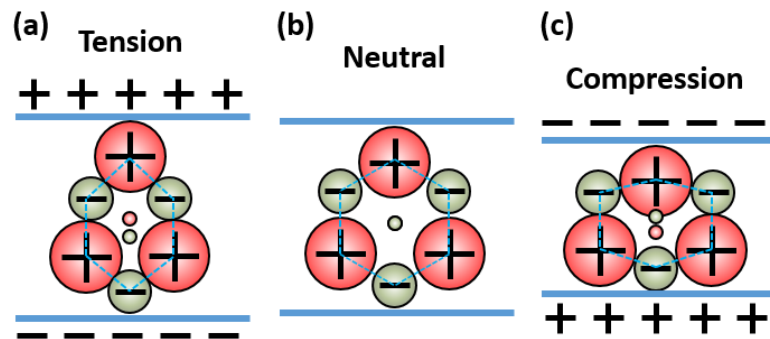


Figure 1-1. Charge generation on a piezoelectric material under different strain conditions.

The electromechanical interaction in piezoelectric materials drives a wide and increasing range of devices [2]. The *direct piezoelectric effect* (electric charge induced by mechanical stress) is utilized in gas ignition, mechanical energy harvesting, and force sensing. And the *inverse piezoelectric effect* (mechanical strain induced by electric field) is used in high-precision actuators and speakers. Combination of the two effects is the basis

of ultrasonic echo transducers, surface acoustic wave devices, and piezoelectric transformers.

1.2. Piezoelectric nanomaterials

Since the beginning of the 21st century, many piezoelectric nanostructures have been synthesized and studied, including ZnO [3], CdS [4], ZnS [5], GaN [6], PVDF [7], diphenylalanine peptide [8], PZT [9], BaTiO₃ [10], NaNbO₃ [11], Te [12], etc. Figure 1-2 shows the microscopic images of single crystalline ZnO nanowires and BaTiO₃ nanowires reported in the literature.

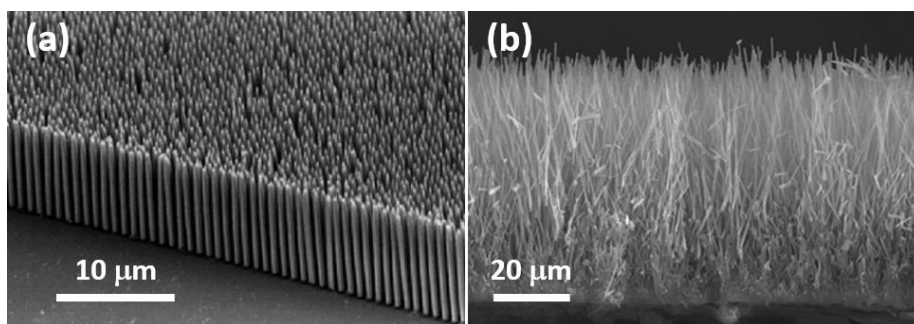


Figure 1-2. Scanning electron microscopy (SEM) images of piezoelectric nanowires. (a) ZnO nanowires on a GaN substrate. Reprinted with permission from [13]. Copyright 2008 American Chemical Society. (b) BaTiO₃ nanowires on an oxidized Ti substrate. Reprinted with permission from [14]. Copyright 2013 Nature Publishing Group.

With reduction in the dimension, piezoelectric nanomaterials have the following advantages compared with their bulk counterparts.

(1) Size

Nanostructures intrinsically have small size without patterning and can potentially be integrated in a microelectromechanical system (MEMS). In such a micro system, logic units have been scaled down to an extreme extent thanks to the development of microfabrication techniques. However, its energy source, usually a battery, and some 3D moving components remain bulky and limit the overall size of the system. On the other hand, the electromechanical coupling in piezoelectric nanostructures can provide functions of generators, sensors, and actuators. If those bulky components can be replaced with piezoelectric nanostructures, the micro system may be further miniaturized and even put inside living organisms.

(2) Flexibility

Nanowires are usually several tens to several hundreds of nanometers in diameter and much longer in length. Using a classical beam theory, some mechanical properties of a nanowire have the following dependence on its diameter:

$$EI \propto Er^4, \varepsilon_{peak} \propto \frac{r}{\rho}$$

where E is the elastic modulus, r is the radius of the nanowire, EI is the bending stiffness of the nanowire, ρ is radius of curvature of a bent nanowire, and ε_{peak} is the largest strain at that segment of the nanowire. As the diameter drops to the nanometer regime, the wire becomes very easy to bend, and the bending curvature could be very small without reaching the fracture strain of the material. Thus, compared with bulk materials, nanowires show larger response to small disturbance like an air flow [15], and have better mechanical impedance match with soft biomaterials [16].

(3) Single crystallinity

Piezoelectric nanowires synthesized by bottom-up methods are often single crystalline. Compared with polycrystalline materials, single crystals contain very few volume defects and therefore have a higher fracture strain and are less likely to fatigue. Molecular dynamic simulation predicted a fracture tensile strain of ZnO nanowires as high as 17.5%, while experimental results in different groups gave fracture strains from 2.3% to 15%, probably due to surface defects [17]. In another test, ZnO nanowire tolerated 1.8% cyclic bending strain for billions of times without fatigue [18]. In comparison, PZT-5H had a fracture tensile strain of less than 0.15% [19]. Although PVDF as a polymer can naturally accommodate large strain, its viscoelasticity is often undesirable and its piezoelectric property is susceptible to the heat and radiation in the environment.

1.3. Application of piezoelectric nanomaterials

The unique property of being small, flexible, and robust gives piezoelectric nanomaterials tremendous opportunities in energy harvesting [20], sensing [21], and actuation [22, 23]. Particularly, nanogenerators and strain sensors have been widely studied and covered by several review papers [24-26].

(1) Nanogenerator

Mechanical energy is ubiquitous in the form of sound, fluid flow, pressure variance, machine vibration, muscle movement, etc. Piezoelectric materials can convert mechanical energy in our surroundings into electricity to power personal electronics, wireless sensor systems, medical implants, etc. [27, 28]. Compared with batteries, they have a longer

lifetime and less environmental impact. Since 2006, piezoelectric nanostructures have been utilized for energy harvesting and called *nanogenerators* [20]. A single nanowire could produce several tens of millivolt voltage [29], and may serve as a sustainable energy source for the future nano systems.

Furthermore, multiple nanowires can be integrated for power scale-up. Figure 1-3 is a schematic diagram of a piezoelectric nanowire array encapsulated in polymer. Such a composite structure is widely adopted in the literature [30-33]. The whole structure is flexible and durable, and large fracture strain of nanowires allows high power density.

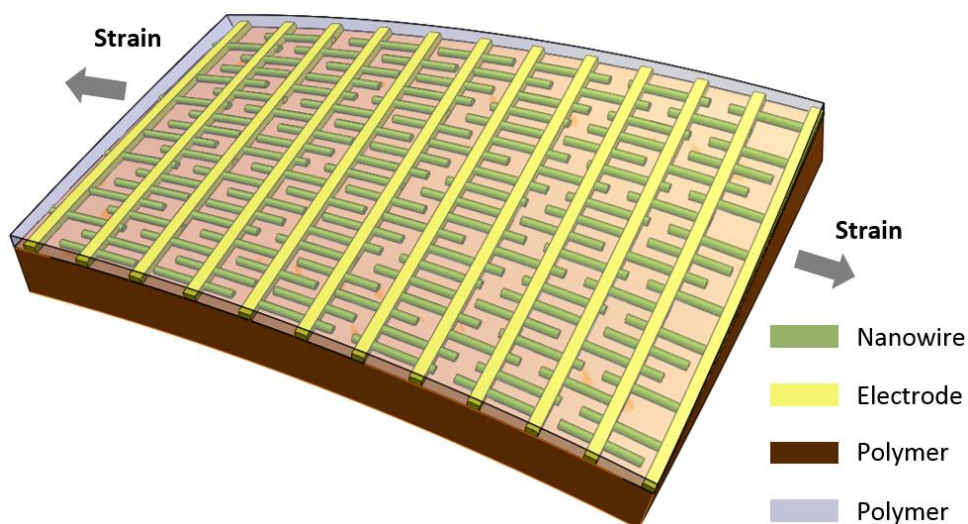


Figure 1-3. Schematic diagram of an energy harvester based on piezoelectric nanowires encapsulated in polymer.

(2) Strain sensor

Most commercial strain gauges utilize resistance change, and other types are based on capacitors, mechanical resonators, and optical fibers. Since 2006, a *piezotronic effect* has been reported on piezoelectric nanostructures with semiconductivity such as ZnO,

GaN, and single atomic layer of MoS₂, and it becomes a new mechanism of strain sensing [21]. Unlike the piezoelectric energy conversion, the piezotronic effect is a more recent discovery and will be explained below.

The piezotronic effect roots in the coupling between piezoelectric and semiconducting properties. In a piezotronic devices, strain-induced piezoelectric charges tailor the electronic properties of the semiconductor interface. Such an interface can be found between two semiconductors (heterojunction), between a semiconductor and a metal (Schottky contact), or between a semiconductor and an electrolyte [34]. Figure 1-4a and Figure 1-4b depict the piezotronic effect at a metal-semiconductor interface, which is the most common case for strain sensors. Without strain, the n-type semiconductor and the high work function metal form a Schottky barrier at the contact, which limits the electron transport from the metal to the semiconductor like a gate. Under strain, polarization charges appear at the metal-semiconductor interface. If the charges are negative, the barrier height will be raised from Φ_{SB} to Φ' and it will be more difficult for electrons to travel across the barrier. On the other hand, positive piezoelectric charges will lower the barrier and increase the electron flow from metal to semiconductor. Experiments and theories have shown that in a piezotronic device with a fixed bias, the current depends exponentially on the strain within some limits [35, 36]. Therefore this phenomenon may provide much higher strain sensitivity than other mechanisms.

The piezotronic effect is not limited to nanostructures; it has also been demonstrated on a polycrystalline ZnO thin film [37]. The advantage of nanostructures

mainly lies in their improved mechanical properties. Being extremely flexible, a nanowire responds to very small forces. Therefore, a vertical nanowire may find applications in sensing fluid flow, as illustrated in Figure 1-4c. If two electrodes could be formed around the root of the nanowire, piezoelectric charges from the bending force would modify the barrier height and consequently the current transport. Such a free-standing design resembles the stereocilia in an inner ear, Figure 1-4d.

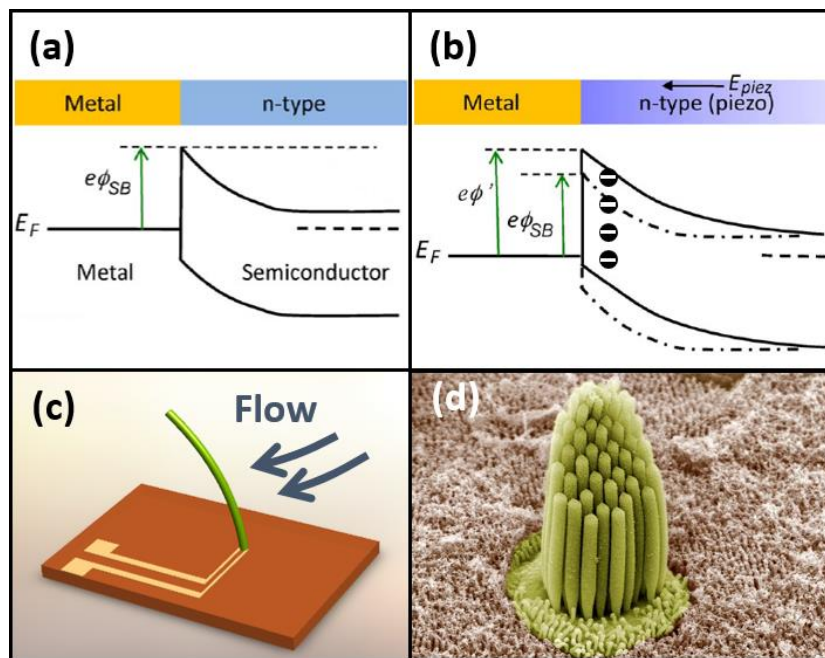


Figure 1-4. Principle of the piezotronic effect and its application. (a) and (b) The Schottky barrier between a high work function metal and a n-type piezoelectric nanowire, without and with piezoelectric charges. Reprinted with permission from [38]. Copyright 2010 Elsevier Ltd. (c) A proposed application of a free-standing ZnO nanowire to sense the flow. (d) SEM image showing the stereocilia of a frog inner ear. Image courtesy of Bechara Kachar at National Institute of Health.

1.4. Motivation

The performance of devices demonstrated in the literature is promising. Nanogenerators have high flexibility and energy density, and piezotronic strain sensors show great sensitivity. Yet, moving from those prototypes to real products needs more progress in different research fields. From the material science point of view, synthesis and assembly of piezoelectric nanostructures still have many limitations, and further investigation on the piezotronic effect is often inhibited by the measurement techniques available presently. Those challenges will be discussed in details below.

(1) Synthesis of piezoelectric nanowires

Piezoelectric nanostructures are manufactured either by a top-down approach or a bottom-up approach. Top-down methods involve deposition of piezoelectric thin film on a substrate followed by lithography process to pattern the film [39]. Nanomaterials from top-down methods are often polycrystalline and largely limited to planar structures. High quality single crystal 3D nanostructures are usually synthesized by a bottom-up approach, in which small components (molecules for instance) self-assemble into complex structures. Such a self-assembly process, however, can be difficult to control, which becomes a general and major obstacle in the commercialization of nanotechnology.

For the bottom-up growth of piezoelectric nanowires, controlling their orientation is important for both device fabrication and operation. Take the piezotronic device as an example, a vertical nanowire is sensitive to surface flow (Figure 1-4c), while a tilted nanowire responds better to a vertical contact force. Orientation control requires epitaxy in

general, in which the growth direction of the nanowire is defined by the crystallographic orientation of the substrate. Epitaxy substrates are usually single crystals with a similar crystal structure with the nanowires. For instance, crystals of ZnO, GaN, and sapphire are used for the well-defined growth of ZnO nanowires [40-44].

Those single crystal substrates are expensive, and nanowires can only take a fixed orientation on one type of substrate. It is necessary to develop a new substrate which has a low cost and can initiate the epitaxial growth of nanowires at an arbitrary direction.

(2) Alignment of piezoelectric nanowires

The small size of nanostructures causes great difficulty in the manipulation. Research laboratories can use sharp probes or even optical tweezers [45] to pick a nanowire and position it on another substrate for device demonstration, but such a manual manipulation cannot handle a large quantity of nanowires at the same time for the mass production in industry.

As illustrated in Figure 1-3 above, alignment and transfer of multiple piezoelectric nanowires onto flexible substrates is necessary to improve the power output of an energy harvester. In Figure 1-5 below, (a) is a nanowire array with poor alignment, and (b) is an array with uniform orientation along the strain direction. The energy harvester in Figure 1-5b will generate more electrical energy under the same strain. The main reason lies in the shear-lag model of composite materials [46], which shows that it is the easiest to transfer strain from the polymer matrix to fibers that are along the strain direction. Higher elastic energy in the nanowires leads to a higher converted electrical energy.

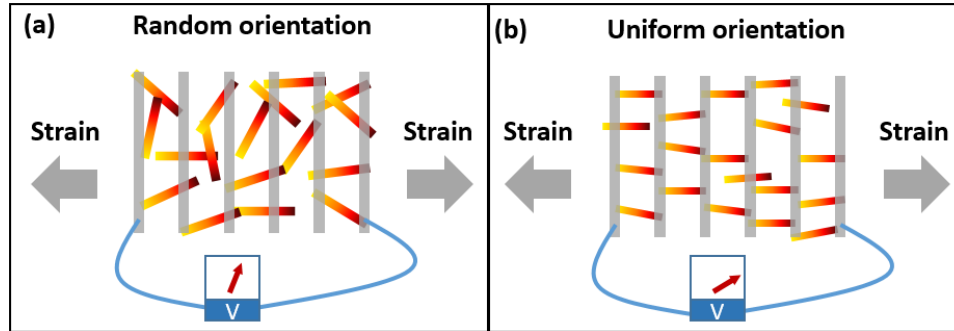


Figure 1-5. Alignment of piezoelectric nanowires for energy harvesting. (a) Nanowires that are randomly oriented generate lower energy. (b) Nanowires that are along the strain direction generate higher energy.

Many techniques have been reported in the literature to align nanowires with their own advantages and limitations. Some techniques only work for a specific type of nanowires; others are more general but require complex microfabrication process or expensive apparatus. An economic and simple method that aligns different types of piezoelectric nanowires is still lacking.

(3) Strain sensing property of a semiconducting piezoelectric nanowire

The third challenge is specifically about the application of semiconducting piezoelectric nanowires in strain sensing. Generally, strain can affect the carrier transport in a nanowire by three mechanisms - the geometric change, the piezoresistive effect that changes the material resistivity, and the piezotronic effect that changes the Schottky barrier height. Figure 1-6 shows a conventional current-voltage measurement circuit. As carriers travel across two metal contacts and the nanowire itself, each contact gives a piezotronic effect, and the nanowire gives a piezoresistive effect (the geometric effect is relatively

small and can be neglected). The measured signal comes from the combination of two piezotronic effects and a piezoresistive effect, and the relative contribution from each effect is not clear.

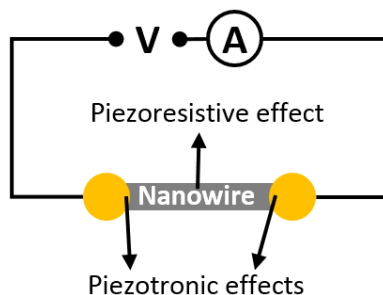


Figure 1-6. Schematic diagram showing the combination of two piezotronic effects and a piezoresistive effect in a typical current-voltage measurement.

In order to quantitatively compare the piezotronic effect and the piezoresistive effect and also to simplify the data analysis in real applications, it is necessary to separate those effects in a single nanowire.

1.5. Thesis Contribution

The overall objective of this study is to advance the research on piezoelectric nanostructures, in the direction towards real applications in energy harvesting and strain sensing. The three challenges introduced in the last section will be addressed in Chapter 2, 3, and 4 respectively.

Chapter 2: A new growth method for piezoelectric nanowires [47]

An inexpensive epitaxy substrate is demonstrated for the bottom-up synthesis of high-quality nanowires. This new method not only reduces the cost and keeps the good

alignment, but also provides much higher design flexibility on the orientation of piezoelectric nanowires for specific applications.

Chapter 3: A new alignment technique for piezoelectric nanowires [48]

The technique aligns nanowires to the same direction with a shear flow and transfers them onto flexible substrates for the fabrication of energy harvesters. It is low cost, fast, scalable, and contamination-free. Different types of nanowires can be aligned and the array density can be easily controlled in a wide range.

Chapter 4: A method to separate different strain sensing mechanisms in a piezoelectric nanowire with semiconductivity [49]

With a novel microfabrication process, multiple electrodes are deposited on a semiconducting piezoelectric nanowire. A classical four-point measurement is modified to isolate the piezotronic effect and the piezoresistive effect when the nanowire is under strain, so that these two effects can be directly compared.

CHAPTER 2. SYNTHESIS OF ZINC OXIDE NANOWIRES WITH UNIFORM ALIGNMENT AND ORIENTATION CONTROL

2.1. Introduction

ZnO has long been recognized as a piezoelectric material and a wide bandgap semiconductor. Over the last decade, its various nanostructures have been synthesized, such as wires, belts, rings, springs, combs, and cages [50]. So far it is the most widely studied piezoelectric nanomaterial. Many piezoelectric nano devices were first demonstrated on ZnO nanowires, including nanogenerators [20, 29], piezotronic strain sensors [21, 35], and nano actuators [22]. Piezoelectric ZnO nanowires have a wurtzite structure, as shown in Figure 2-1. Some other popular piezoelectric nanowires like CdS, ZnS, and GaN belong to this crystal structure as well. Growth mechanisms of those binary compound nanowires are also similar [5, 51, 52]. Therefore, although this chapter focuses on the growth of ZnO nanowires, the principle can be applied to many other piezoelectric nanowires.

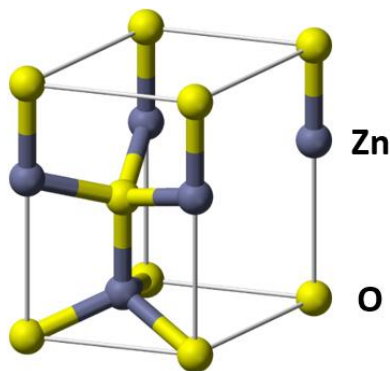


Figure 2-1. Wurtzite crystal structure of ZnO.

The objective of this chapter is to control the growth orientation of the ZnO nanowires, so that we can optimize the energy harvesters and strain sensors for mechanical stimuli from different directions. Moreover, alignment and orientation control will have a broader impact on other fields. For example, vertical nanowires with uniform spacing can improve the light trapping and charge separation in nanowire-polymer solar cells [53, 54]; the direction and distribution of the ZnO nanowire array significantly affect the field emission characteristics [55, 56]; many research efforts have been spent to obtain lateral ZnO nanowires to facilitate the electrodes fabrication [44, 57-60].

While many solution-phase [61] and gas-phase [3, 62, 63] methods have been studied for ZnO nanowire growth, uniform and well-aligned nanowire growth requires epitaxy in general. As shown in Figure 2-2, vertical nanowires can be grown on single crystal c-plane GaN [40] or a-plane sapphire [41], tilted nanowires can be grown on m-plane sapphire and form an angle of 30° with substrate normal [42, 43], and horizontal nanowires can be grown on single crystal ZnO ($2\bar{1}\bar{1}0$) surface [44]. However, those substrates have two limitations. First, they are very costly; sapphire wafers are much more expensive than silicon wafers, and GaN wafers are typically grown on sapphire wafers and thus have an even higher cost. Second, one single crystal substrate only allows one growth direction of ZnO nanowires.

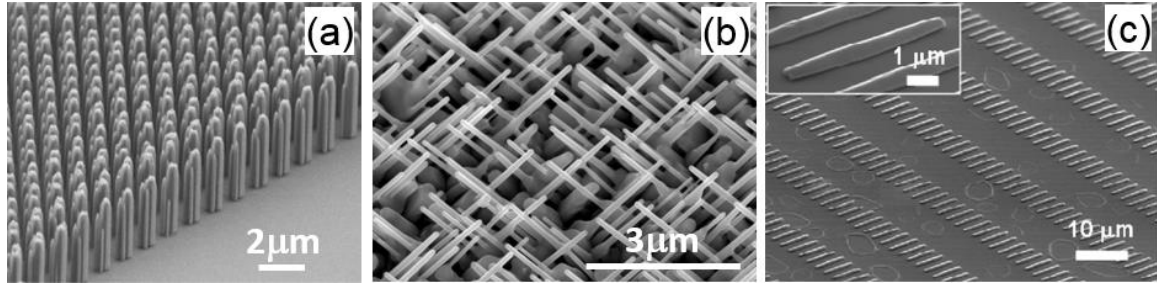


Figure 2-2. Epitaxial growth of ZnO nanowires on various single crystals. (a) Vertical ZnO nanowires on a c-plane GaN substrate. Reprinted with permission from [13]. Copyright 2008 American Chemical Society. (b) Tilted ZnO nanowires on an m-plane sapphire substrate. Reprinted with permission from [43]. Copyright 2007 IOP Publishing. (c) Horizontal ZnO nanowires on a ZnO ($2\bar{1}\bar{1}0$) surface. Reprinted with permission from [44]. Copyright 2009 American Chemical Society.

In order to obviate the needs for those expensive single crystals, a more economical and versatile route is to form a c-oriented ZnO seed layer on a non-epitaxial substrate [53]. Such a seed layer was observed at the early stage of nanowire growth [64], and it can also be introduced by pulsed laser deposition [65], zinc salt thermal decomposition [53], magnetron sputtering [66] before the nanowire growth. Nevertheless, the c-orientation of a single-layer ZnO seed is poor compared with single crystals. Recently, a better c-orientation was observed in a double-layer ZnO seed. The first layer is a polycrystalline film from zinc acetate decomposition or ZnO sputtering and the second layer is a textured film grown on the first layer by a hydrothermal process, and the vertical alignment of nanowires was significantly improved on the textured film [67-69]. The textured ZnO film is a promising and inexpensive alternative to the single crystal substrates, but studies in the

literature so far have been limited to the ZnO nanowire arrays normal to the substrate. In this chapter the textured film is further developed to initiate nanowire growth with a general orientation control [47].

2.2. Growth and characterization of a textured ZnO film

Preparation of the textured film started with the deposition of 5 nm Cr and 100 nm ZnO by magnetron sputtering on silicon. Then, an aqueous growth solution containing 175 mM hexamethylenetetramine (HMTA, Sigma-Aldrich) and $\text{Zn}(\text{NO}_3)_2$ (Sigma-Aldrich) was prepared by very slowly adding the HMTA solution into the $\text{Zn}(\text{NO}_3)_2$ solution. Upon mixing, the solution turned turbid, so it was filtered twice to remove the precipitation. Silicon substrates were placed floating on the growth solution, with the seeded side facing down. The growth was conducted at 95 °C for 6 hours in an oven. Possible reactions in the solution are listed in Figure 2-3a [61]. Similar hydrothermal process has been used for ZnO nanorod synthesis [70]; Figure 2-3b shows the growth of separated nanorods with a 40 mM solution. Here, much higher nutrition concentration of 175 mM resulted in a quasi-continuous film when densely packed nanorods eventually merged with each other.

(a)

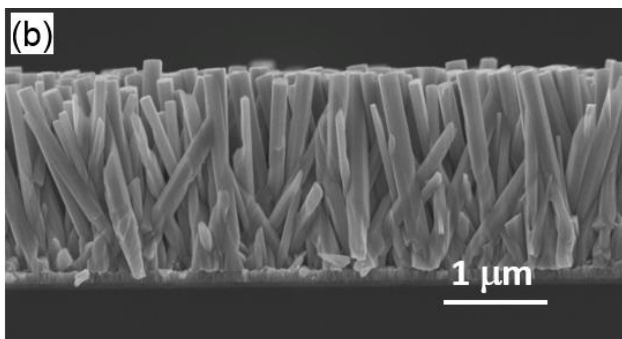
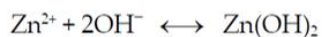
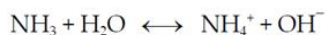


Figure 2-3. Hydrothermal growth of ZnO nanorods. (a) Some possible reactions during the hydrothermal growth. (b) ZnO nanorods grown from a 40 mM solution.

Scanning electron microscopy (SEM) image of the textured film in Figure 2-4a clearly shows that the film consists of closely-packed nanorods. And the cross-sectional view of the film in Figure 2-4b shows that texture was improved from bottom to top. As the growth was initiated at the bottom, the grains were relatively small and had various orientations due to the imperfect c-orientation of ZnO crystallites in the sputtered layer. As the growth continued the grains became larger nanorods. Because of the spatial confinement effect [67, 71], those nanorods perpendicular to the substrate surface dominated, yielding a strong out-of-plane texture. Figure 2-4c to 2-4e explain the spatial confinement effect in a 2D space. At the beginning of the growth, nanorods are short and randomly oriented. Assuming all nanorods grow at the same rate, they collide with each other as they become longer, and those with larger tilt angles are stopped after the collision. As more and more collisions happen, only those nanorods perpendicular to the substrate or at the edge can continue growing. Nanorods also grow laterally and merge with each other.

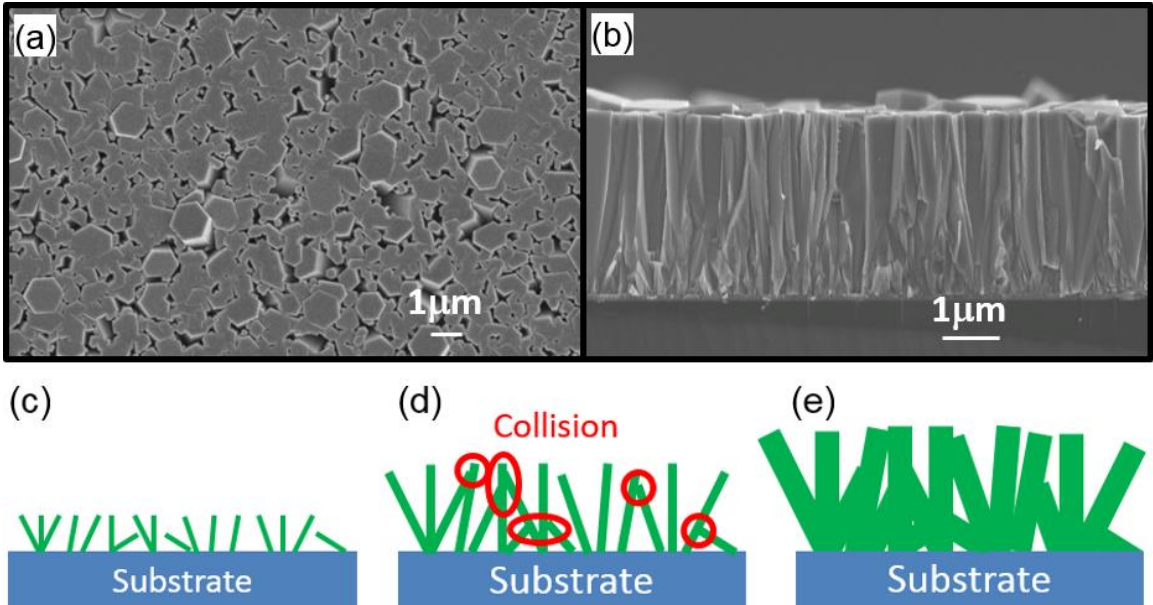


Figure 2-4. SEM images of the textured ZnO film and the spatial confinement effect. (a) and (b) SEM images showing the top view and cross-sectional view of a textured ZnO film. (c) Illustration of the early stage of the growth. (d) As the nanorods grow longer, collision stops those nanowires with large tilt angles. (e) Nanorods grow laterally and start to merge with each other.

The improved texture was further confirmed by an X-ray diffractometer (XRD) equipped with an area detector, with a 35° incident angle. Figure 2-5a and 2-5b are the 2-dimensional (2D) diffraction frames of a textured film and a sputtered film respectively, where the brightest Debye ring corresponds to the (002) peak. The converted XRD patterns of the two films in Figure 2-5c show only strong (002) reflections, indicating a preferential c-axis orientation. The intensity variation along the Debye ring is another measurement of the texture. Figure 2-5d shows how the intensity changes along the (002) ring of both

samples. The intensity variation of the textured film is more significant than the sputtered film, indicating a much stronger texture.

It should also be noted that, in addition to the silicon substrate, a variety of substrates can also be used for the textured film growth, as long as they can survive the hydrothermal process at 95 °C.

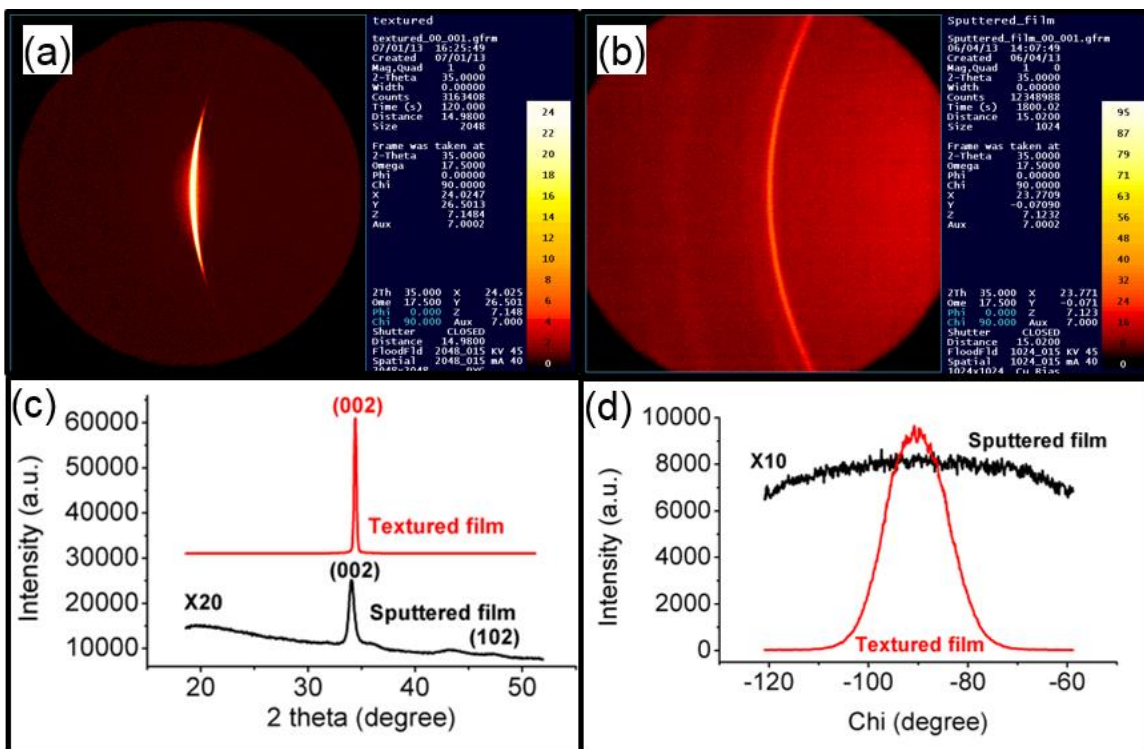


Figure 2-5. XRD characterization of the textured ZnO film. (a) 2D XRD frame of a textured ZnO film. (b) 2D XRD frame of a sputtered ZnO film. (c) XRD patterns of the textured film and the sputtered film. Both only have strong (002) peaks. The patterns were shifted vertically for comparison. (d) Intensity variation along the (002) Debye rings of (a) and (b), indicating a better c-orientation from textured film.

2.3. Epitaxial synthesis of ZnO nanowires

The improved texture and larger grain size in the film allow epitaxial growth of ZnO nanowire along the normal direction of the substrate. We employed a modified chemical vapor deposition (CVD) process, proposed by Kuo et al. [72] and Zhu et al. [73], and achieved ultra-long nanowires with unprecedented alignment. Although nanowires can also be synthesized by a hydrothermal process, CVD produces longer nanowires with better crystallinity and fewer defects.

To prepare the source material of the CVD process, activated carbon powder (Alfa Aesar) and ZnO nanopowder (Sigma-Aldrich) (1:1 by weight) were dispersed in methanol and ultrasonicated for 1 hour for thorough mixing. The slurry was put in a 65 °C oven overnight to evaporate the methanol. For the CVD growth, an alumina boat containing 0.6 gram of mixed activated carbon powder and ZnO nanopowder was placed in a tube furnace. The textured film on silicon was placed on the boat, approximately 4 mm above the source material. The tube was first pumped down and heated to remove moistures and organic contaminations, and then raised to 50 Torr with flowing oxygen (10 sccm) and argon (30 sccm). Reaction took place at 960 °C for 5 to 10 minutes. At such a high temperature, the carbon powder reduces the ZnO nanopowder into zinc vapor, and then zinc vapor reacts with oxygen on the surface of the substrate to form ZnO nanowires. The length of nanowires increases with the reaction time and the longest nanowire array achieved from this study reaches 120 μm. Table 2-1 summarizes the temperature, pressure, and gas used at different stages of the process. Figure 2-6a shows the schematic diagram of the tube

furnace, and Figure 2-6b is a picture of the alumina crucible loaded with source material and three substrates.

Stage	Duration	Temperature	Pressure	Gas flow
1. Pump down	1 hour	160 °C	≤ 20 mTorr	No flow
2. Ar flowing	Until pressure reaches setpoint	160 °C	50 Torr	30 sccm Ar
3. Temperature ramp	15 min	160 °C to 910 °C at 50 °C/min	50 Torr	30 sccm Ar
4. O ₂ flowing	Instant	910 °C	50 Torr	30 sccm Ar 10 sccm O ₂
5. Temperature ramp	1 min	910 °C to 960 °C at 50 °C/min	50 Torr	30 sccm Ar 10 sccm O ₂
6. Constant temperature (growth)	5 to 10 min	960 °C	50 Torr	30 sccm Ar 10 sccm O ₂
7. Cooling down	Several hours	960 °C to room temperature	≤ 20 Torr	30 sccm Ar

Table 2-1. Process parameters of the tube furnace during the CVD synthesis.

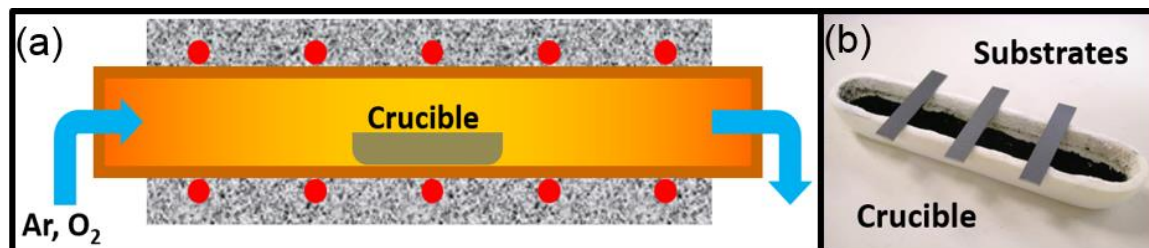


Figure 2-6. CVD system. (a) Schematic diagram of the tube furnace. (b) An alumina crucible loaded with source material and three substrates.

Although the spatial confinement can enhance the alignment in dense nanowire arrays [67, 71], the exceptional alignment of the nanowire arrays from the textured film is mainly due to the much improved seed layer. A comparison experiment was performed

between the nanowires grown from the textured ZnO film and the nanowires grown from the sputtered ZnO film. Both films were partially coated with 20 nm of silicon oxide (SiO_2) mask by magnetron sputtering to reduce the spatial confinement effect. In Figure 2-7a, ZnO nanowires grown on discrete regions from the textured film preserve the vertical orientation, even at the edge of the clump. In comparison, the nanowires grown at the same condition but from sputtered seed do not have a good alignment, as shown in Figure 2-7b. Some vertical nanowires are only observed in the middle of the ZnO nanowire clusters from the sputtered film where the surrounding nanowires provide certain spatial confinement. At the edge of the cluster, the effect of spatial confinement decreases and the nanowires have a wide distribution of angles. Although the XRD analysis in Figure 2-5c indicates that the sputtered seed layer is also dominated by crystallites with c-axis normal to the substrate, its c-orientation and crystallinity are not good enough to promote the vertical growth.

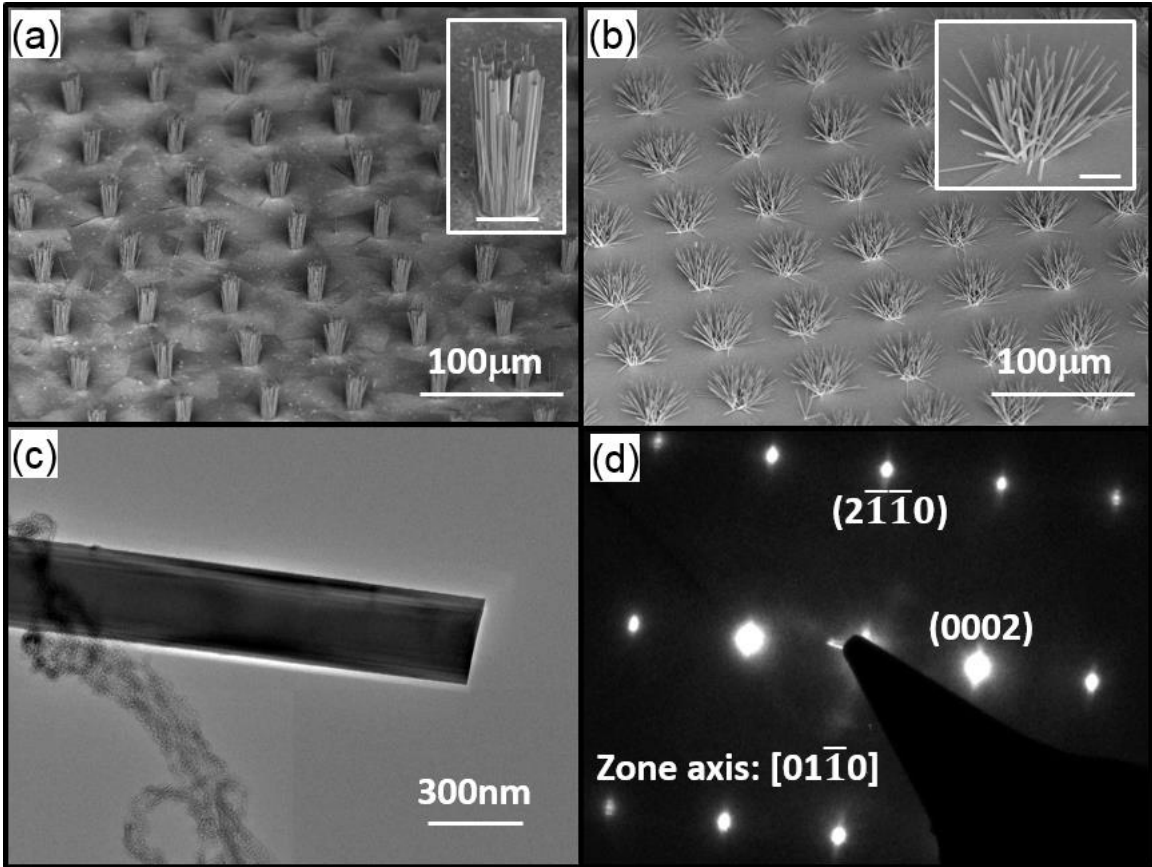


Figure 2-7. CVD synthesis of ZnO nanowires. (a) SEM image for nanowires grown with a CVD process on a patterned textured film. Inset: A nanowire clump with vertical alignment; scale bar is 10 μm . (b) SEM image for nanowires grown on a patterned sputtered film. Inset: A nanowire cluster with a wide distribution of angles; scale bar is 10 μm . (c) TEM image of a nanowire grown on a textured film. (d) Selected area diffraction pattern of the nanowire in (c); the zone axis was $[01\bar{1}0]$ and the growth direction was confirmed to be $[0001]$.

Some nanowires grown on the textured film were transferred onto a copper grid and observed in a transmission electron microscope (TEM). The selected area diffraction

function of the TEM can perform electron diffraction on a single nanowire to determine its crystal structure. As shown in Figure 2-7c and 2-7d, the TEM confirms that the nanowire grew along the [0001] direction, i.e. the c-direction. Therefore, there exists epitaxy relationship between the textured ZnO film and the ZnO nanowires.

2.4. Tilted and lateral nanowires

A unique advantage of textured film over single crystal GaN and sapphire is that it can be easily grown on a wide range of materials with different topographies, such that a general orientation control may be achieved. The orientation control was studied with the growth of nanowire arrays on silicon substrate along two different angles from the substrate normal direction. Inclined walls of 54.7° and 35.3° with respect to the silicon wafer plane can be achieved by wet-etching (100) and (110) silicon wafers respectively in potassium hydroxide (KOH) solution. The substrates with different inclined walls underwent the hydrothermal process for the textured film formation and then the CVD process for the nanowire growth. In Figure 2-8a, the textured film copies the shape of the wall inclined 54.7° and the nanowires grow perpendicularly to the textured film, such that the nanowire from the side wall is tilted 54.7° from the substrate normal direction. Figure 2-8b shows nanowires from two adjacent walls contact each other, and it provides a potential route for fabricating nanowire interconnection. In contrast, Figure 2-8c and Figure 2-8d show nanowires grown on sputtered ZnO seed under the same growth condition; they have random directions and certain alignment is only observed in the long and dense nanowires from the top surface where spatial confinement can play a role. The nanowire arrays have

also been grown on the inclined walls of 35.3° with respect to the silicon wafer plane. With the textured film, nanowires are well-aligned just like on a single crystal epitaxy substrate while taking predetermined orientations, as shown in Figure 2-8e and Figure 2-8f. It is noteworthy that with proper reactive ion etching (RIE) on silicon [74], various positive or negative tapered walls can be achieved, and therefore perfectly aligned nanowire arrays can be grown at any desired orientation.

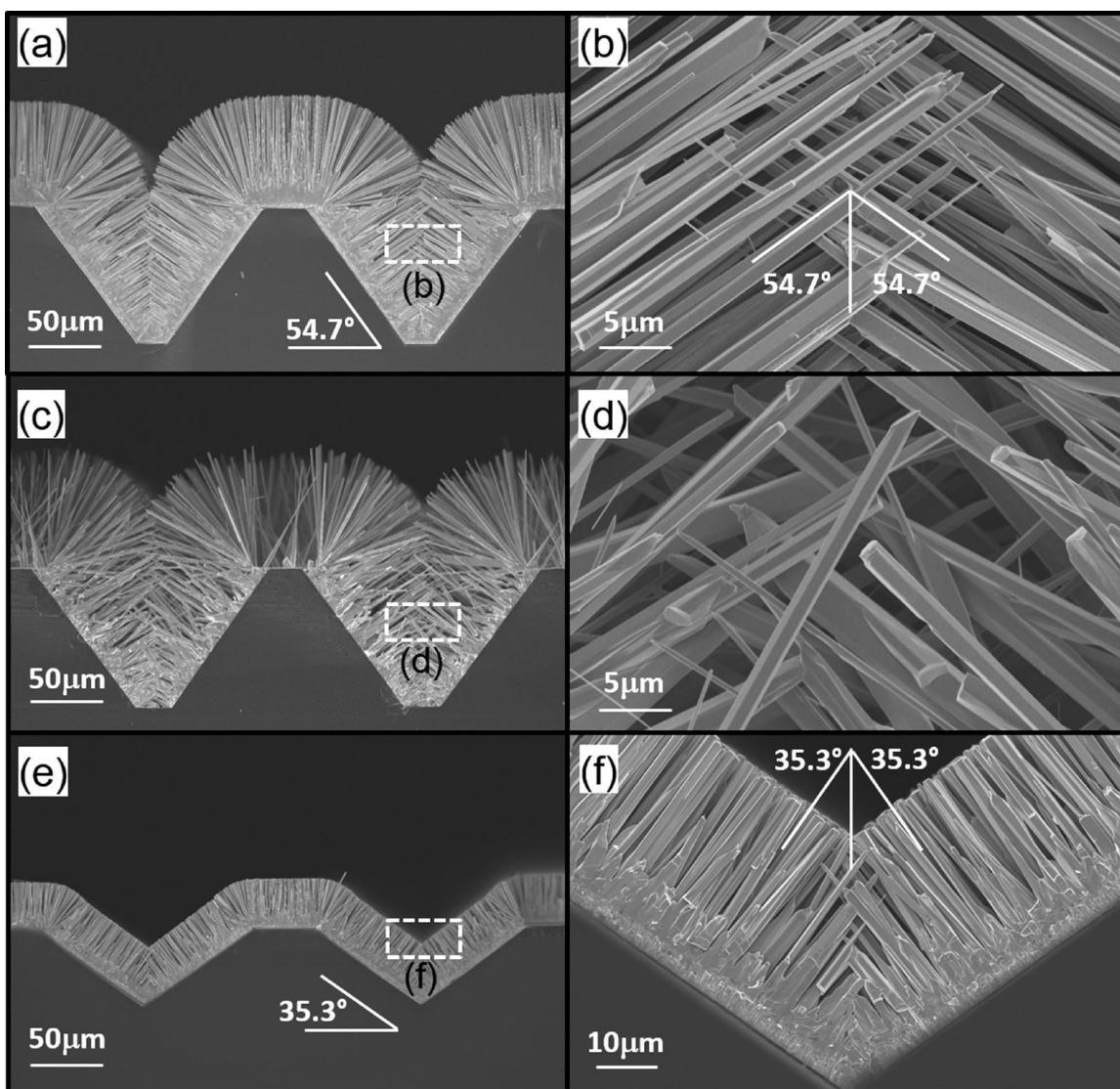


Figure 2-8. Tilted growth of ZnO nanowire arrays. (a) SEM image of nanowires on a textured film coated on etched (100) silicon substrate. (b) Enlarged view of nanowires tilted 54.7° from substrate normal direction from the region specified in (a). (c) SEM image of nanowires on a sputtered film coated on etched (100) silicon substrate. (d) Enlarged view of nanowires with random orientation from the region specified in (c). (e) SEM image of nanowires on a textured film coated on etched (110) silicon substrate. (f) Enlarged view of nanowires tilted 35.3° from substrate normal direction from the region specified in (e).

This method can also produce horizontal ZnO nanowire arrays. Making electric contacts to vertical ZnO nanowires is complex [75]. Lateral epitaxial growth was observed only on a single crystal ZnO ($2\bar{1}\bar{1}0$) surface [44] and on various flat or faceted sapphire surfaces with controlled growth direction and crystallographic orientations [59, 76], while other approaches only produce lateral nanowire without uniform alignment when the strict epitaxy relationship between the nanowire and the substrate is not satisfied [57, 58, 60]. Using textured film on a vertical wall is a simple and low-cost way to synthesize well-aligned lateral nanowires. We applied KOH etching on (110) silicon to make vertical walls, and a RIE process works as well. The KOH process is illustrated in Figure 2-9a. The (111) planes of the (110) silicon are perpendicular to the wafer surface; because (111) planes have a very low etch rate in KOH bath compared with other planes, the etching results in vertical walls. The wafer also has a buried layer of SiO₂ to stop the etching. Without such a stopping layer, the bottom surface is very rough after the etching, Figure 2-9b.

Next, ZnO seed was sputtered on the etched silicon and a hydrothermal reaction was performed. Textured film not only grew along the vertical wall but also covered the horizontal part. In order to suppress the formation of vertical nanowires from the horizontal surface, 300 nm of SiO₂ was deposited on the horizontal textured film by electron beam evaporation. It should be noted that evaporation has a poor step coverage compared with sputtering and thus a much thicker deposition was used to fill the pinholes in the textured film. If unidirectional nanowires are desired, a second deposition of SiO₂ can be performed on one side of the walls. The whole process is illustrated in Figure 2-10a.

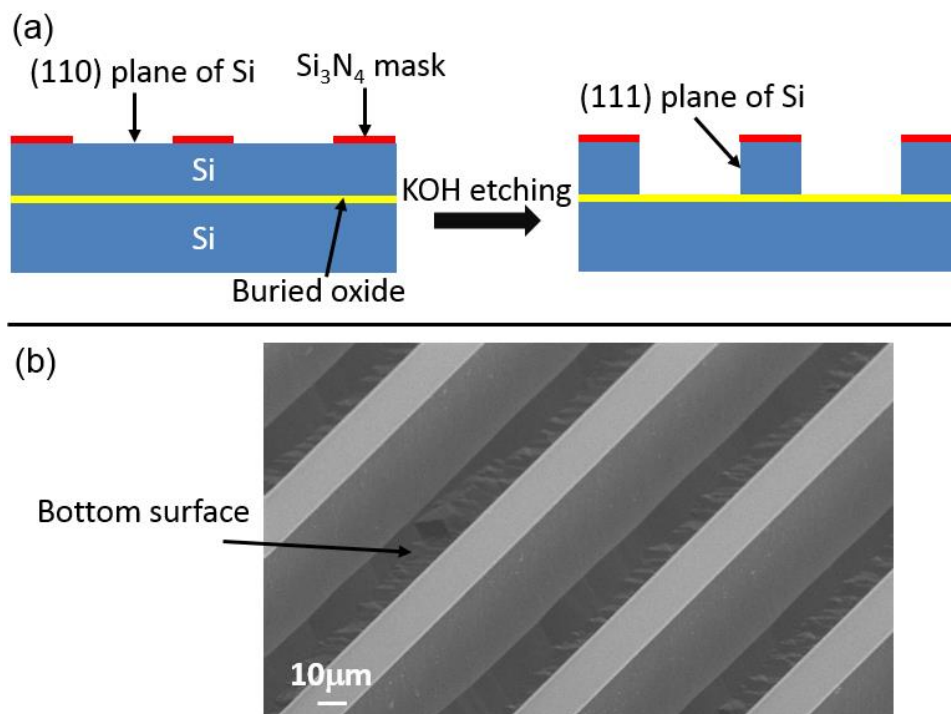


Figure 2-9. KOH etching on (110) silicon to produce a vertical wall. (a) Schematic diagram of the process; the vertical walls are the (111) planes of silicon, which have a very low etch

rate in KOH bath compared with other crystallographic planes. (b) KOH etching on a (110) silicon wafer without an oxide stopping layer; the bottom surface is very rough.

Figure 2-10b shows the lateral nanowires on both sides of the walls with a single SiO₂ coating. The alignment is not as uniform as in previous growths with textured films, possibly because the narrow space between walls limits the vapor transport during CVD. Figure 2-10c and Figure 2-10d are the images of unidirectional nanowires on a substrate with two SiO₂ depositions. Nanowires are well-aligned and parallel to the horizontal surface, except for a few tilted nanowires at the edge. A close investigation reveals that most of the tilted nanowires are from pin holes on the textured film that are not covered by SiO₂ coating. Nevertheless, the overall quality is high, and the improved alignment compared with double-sided growth may be attributed to the larger space between walls. In addition, unlike the lateral growth on single crystal ZnO or sapphire, the nanowire array on textured film has multilayers, and the nanowire population depends on the height of the wall. All the nanowires from the top part and the bottom part of the wall have the same length.

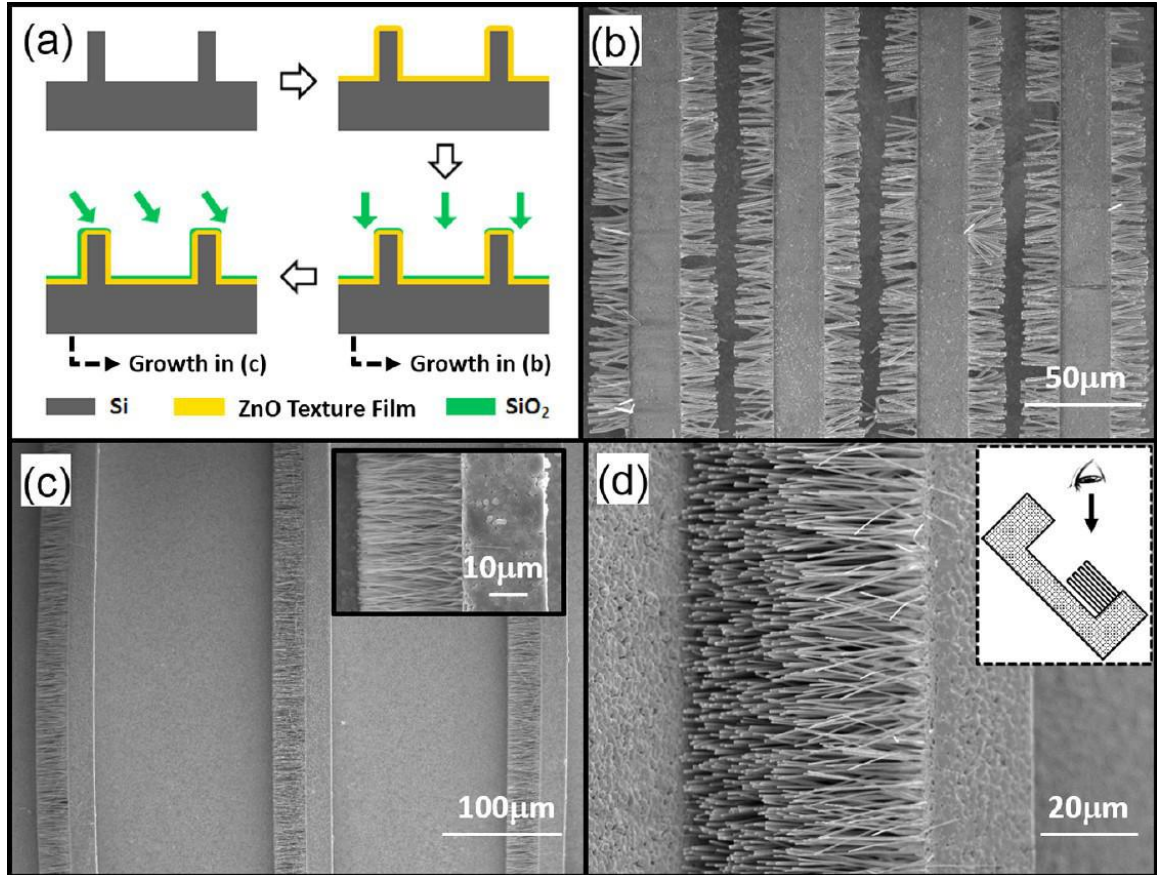


Figure 2-10. Lateral growth of ZnO nanowire arrays. (a) Schematic diagram showing the preparation of the substrate for growing double-sided and single-sided horizontal nanowires. (b) SEM image of double-sided horizontal nanowires grown with a textured film. (c) SEM image of single-sided horizontal nanowires grown with a textured film. Inset: Enlarged view of the horizontal nanowires with a uniform alignment. (d) 45 ° tilted SEM image of the horizontal nanowires covering from the top to the bottom of the wall. Inset: Illustration of the angle of view.

2.5. Complex nanostructures

This growth technique is general and not limited to silicon. Although the backing substrate for the nanowire growth needs to survive the CVD process at 960 °C, a wide range of substrates from ceramic, metal, to plastic can be used to grow the textured film through the hydrothermal process at 95 °C. The benign hydrothermal process provides numerous opportunities and can even enable the growth of 3D architectures with well-established photolithography technique. For example, SU-8 can be patterned into high-aspect-ratio and complex 3D microstructures [77], and the chemical and mechanical stability makes it an ideal mold for textured film. The versatility from photoresist can help design textured film with complex shapes, so as to grow nanowires with controlled spatial distribution and orientation to fulfill specific application requirements.

The versatility of this method is demonstrated for the growth of hierarchical nanostructures. The fabrication steps are illustrated in Figure 2-11a. We firstly fabricated an array of SU-8 micropillars on silicon. The textured film was conformally coated on the micropillars through the hydrothermal growth. Note that the SU-8 was fully cross-linked by hard baking and UV exposure, so it was stable during the wet chemical process. The SU-8 mold was then removed through oxidation at 600 °C in atmosphere with a slow temperature ramp, leaving a self-supported textured film structure on the supporting silicon substrate. It is important to keep the temperature ramp slow, otherwise the textured film structure would be damaged. Figure 2-11b shows the textured film with SU-8 mold removed, and the inset shows the hollow structure of a micropillar detached from the substrate by ultrasonication. The textured film possesses two critical features for this

technique to succeed. First, the textured film is composed of merged ZnO nanorods, so it has sufficient mechanical strength to support itself. Second, the textured film still has some pinholes and is permeable to the outgoing gas during the oxidation of SU-8.

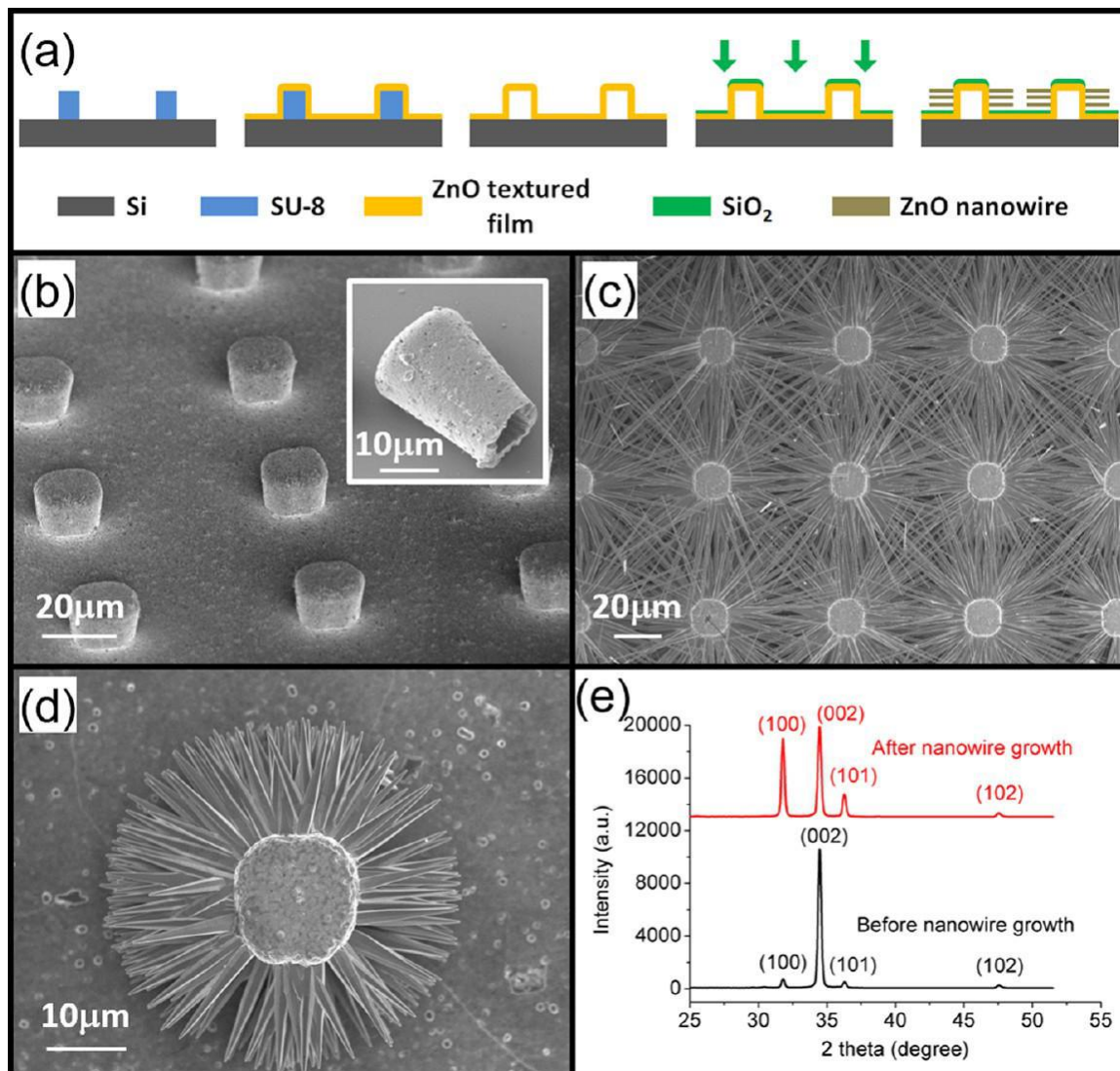


Figure 2-11. Nanowire growth on self-supported 3D textured film. (a) Schematic diagram of the fabrication steps. (b) 3D textured film forming an array of micropillars with the SU-8 mold removed. Inset: Hollow structure of a micropillar detached from the substrate. (c)

Ultra-long nanowires grown on the micropillars with radial and lateral orientation. (d) Nanowires grown on a micropillar with shorter length. (e) XRD patterns before and after the growth of nanowires showing the significant contribution to (100) and (101) peaks from the ultra-long lateral nanowires. The patterns were shifted vertically for comparison.

After a 300 nm SiO₂ mask was deposited on the horizontal surface of the textured film, laterally and radially aligned ZnO nanowires could be obtained from the side surface of the micropillars, as shown in Figure 2-11c. The nanowires from different micropillars intersect with each other and form a network. Tuning the growth condition could also produce shorter nanowires on the micropillar, mimicking a “mini sea urchin”, as shown in Figure 2-11d. The lateral growth on the micropillars was characterized by XRD in Figure 2-11e. Before the CVD growth, horizontal part prevails in the textured film on the substrate, giving a strong (002) peak while the other peaks are very weak. After the growth, nanowires are parallel to the substrate, raising the (100) and (101) peaks which are contributed mainly by the horizontal and radial nanowire arrays from the vertical pillar walls.

2.6. Discussion and future work

In this chapter we synthesized well-aligned ZnO nanowires with vertical, tilted, and lateral orientations on textured ZnO films. Some further investigation is needed to improve this method and extend its application.

(1) Selectivity of the CVD process

For the patterned growth of nanowires, we use SiO₂ coating as the mask. The CVD process should have a good selectivity so that the nanowires only nucleate on the exposed textured ZnO film, not on the SiO₂ mask. However, in many cases the ZnO nanowires with random orientation also grew on the SiO₂ film. In fact more than half of the growths were not successful due to the poor selectivity.

It has been observed that the partial pressure of zinc vapor and oxygen vapor during the reaction play an important role on the selectivity. The higher the vapor pressure, the easier the nanowires will grow on SiO₂. If the vapor pressure is too high, the reaction can even take place in the gas phase and form ZnO particles, which is called a homogeneous nucleation. On the other hand, if the vapor pressure is too low, no nanowire will grow on the textured ZnO film. Therefore, there exists a range of vapor pressure that nanowires can selectively grow on the textured film. However, with the current setup it is impossible to precisely control the partial pressure of zinc vapor and oxygen vapor, because the formations of these two vapors are coupled through the carbon powder. Carbon not only reacts with ZnO to produce zinc vapor, but also reacts with oxygen. For example, when the oxygen flow rate is increased, more carbon will be consumed by oxygen and less can react with ZnO powder to form zinc vapor.

In order to control the vapor pressure for a highly selective growth, zinc vapor and oxygen vapor must be supplied from two independent sources. Figure 2-12 gives a possible design of such a CVD system.

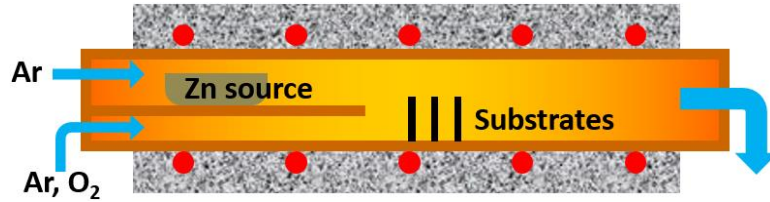


Figure 2-12. A possible design of a CVD system that can supply zinc vapor and oxygen vapor independently.

(2) Pinholes on the textured film

As shown in the SEM images in Figure 2-4, textured ZnO films often have pinholes. Some deep pinholes cannot be covered by SiO₂ through evaporation, and those spots may initiate unwanted growth of ZnO nanowires. Pinholes in the textured film are actually spaces between nanorods that are not closely-packed during the hydrothermal process. In order to eliminate those defects, nanorods in the textured film must have enough nutrition to grow laterally and merge, which requires a highly concentrated solution of HMTA and Zn(NO₃)₂. However, if the starting growth solution is too concentrated, the chemicals will react even at the room temperature to form homogeneous nucleation.

A possible route to solve the problem is to replenish the reagent. As the textured film develops, ions in the solution are consumed. If the solution is refreshed during the growth, the nanorods may have enough nutrient to fully develop laterally.

(3) Diameter control

Diameter is as important as length in determining the mechanical property of ZnO nanowires. A thinner nanowire has a better flexibility to respond to small forces. While the

length of nanowire is controlled by the CVD process time, the diameter control is not straightforward.

It has been noticed that pressure of the reactive vapor has a significant influence on the diameter of nanowires [78]. More concentrated vapor leads to a larger diameter in general. For example, we sometimes observed that in a single growth, the nanowire had a segment on top with smaller diameter (Figure 2-13), which was due to the reduced vapor pressure near the end of the growth. As mentioned before, it is difficult to precisely control the reactive vapor pressure with the present CVD setup. Therefore a system that can supply zinc vapor and oxygen vapor independently is needed.

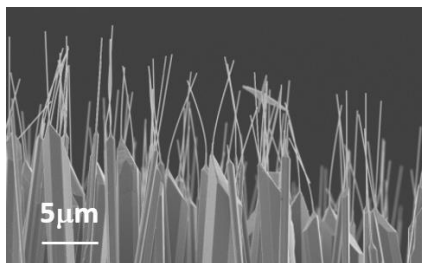


Figure 2-13. Thick wires with a thin segment on the tip, obtained in a single growth.

Alternatively, a *vapor-liquid-solid* mechanism may be utilized for the CVD synthesis of ZnO nanowires. In the present system, zinc vapor and oxygen vapor react directly on the substrate surface; such a growth mechanism is called a *vapor-solid* process. In a *vapor-liquid-solid* process, there is a thin layer of metal deposited on top of the epitaxy substrate as a catalyst during the growth, and the diameter of nanowires partially depends on thickness of metal catalyst [79]. The metal thickness provides another degree of freedom to control the diameter of nanowires.

(4) Other piezoelectric nanowires

It is feasible and also important to extend this method to other piezoelectric nanowires. There are two major requirements for the material choice. First, the nanowire can be synthesized by a bottom-up approach on an epitaxial substrate. Second, an epitaxial textured film with preferable crystal orientation can be formed on a non-epitaxial surface. GaN is a promising candidate. GaN nanowires can be synthesized by chemical vapor deposition on a sapphire substrate with epitaxy [80], and textured ZnO film can be used as an epitaxial substrate for GaN nanowires because they have the same crystal structure and very close lattice constants.

CHAPTER 3. ALIGNMENT AND TRANSFER OF NANOWIRES IN A SPINNING LANGMUIR FILM

3.1. Introduction

Assembly of one-dimensional nanostructures is a critical aspect in the development of bottom-up nanodevices. As mentioned in Chapter 1, for an energy harvester with piezoelectric nanowires embedded in a polymer matrix, its power output is maximized when all the nanowires are aligned along the tensile strain direction. Sophisticated approaches can accurately position nanowires through predefined patterns or localized forces [45, 81], as shown in Figure 3-1a and 3-1b from [81]. However the fabrication of energy harvesters only requires aligned nanowire arrays without registering each individual nanowire (i.e., the position of individual nanowire is not precisely controlled). Figure 3-1c shows an energy harvester made from aligned ZnO nanowires without registration [30].

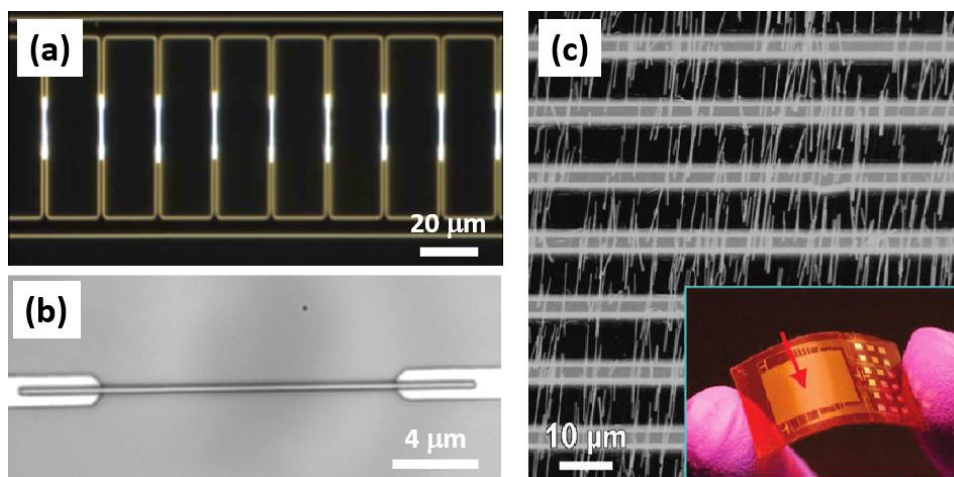


Figure 3-1. Examples of nanowire alignment in the literature. (a) and (b) Nanowires were accurately positioned between two electrodes by dielectrophoretic forces. Reprinted with

permission from [81]. Copyright 2010 Nature Publishing Group. (c) ZnO nanowires were aligned by a contact printing method to fabricate an energy harvester; the inset shows the energy harvester after packaging. Reprinted with permission from [30]. Copyright 2010 American Chemical Society.

Non-registering alignment of nanowires also finds applications other than energy harvesting. For electronic devices, aligned nanowires greatly simplify the design and fabrication of electrode pattern. In nanowire-based composites, the direction of nanowires determines their mechanical, thermal, and electrical behaviors [82-84]. A good alignment enables the anisotropic property of individual nanowire, such as lasing [41], to have macroscopic effect.

Many alignment techniques have been developed in the literature for the alignment of specific nanowires. Alignment with electric field or magnetic field [85-88], as one of the earliest techniques, requires certain electromagnetic properties from the nanowire. Contact printing has minimum misalignment [89, 90], but it mainly works for nanowires grown vertically on a substrate (such as the example in Figure 3-1c). Spincoating aligns and sorts nanowires simultaneously [91, 92], but the surface chemistry between the substrate and nanowires needs to be optimized.

Controlling the areal density of aligned array is also necessary. Langmuir-Blodgett alignment can only produce dense nanowire arrays [93, 94]. While a high density is helpful in many applications such as the integration of nanowire transistors, a lower density may be desired in other cases. Take energy harvesters for example, the density of nanowires

embedded in the polymer matrix determines the stiffness of the device and is an important design parameter. Similarly, the density of nanowires may affect device properties like electrical conductivity, transparency, thermal conductivity, piezoelectricity, and so on in other composite structures.

Compared with the other methods, alignment based on shear flow has minimum requirement on the property of nanowires, and usually allows the array density to be tuned [95-98]. The shear stress in fluids depends on the shear rate and the viscosity:

$$\tau = \mu \frac{\partial U}{\partial y}$$

where τ is the shear stress, μ is the viscosity, and $\partial U/\partial y$ is the local shear rate. Therefore, in order to align nanowires, most approaches use either a high shear rate in a confined space [95, 96, 98] or a viscous fluid [97] to produce sufficient shear stress. However, those methods have limitations. The confined space limits the scalability of the alignment, while the viscous fluid, such as epoxy, completely encapsulates the nanowires and is difficult to remove.

On the other hand, a thin layer of molecules floating on the surface of fluids, called a Langmuir film, can increase the surface viscosity without changing the bulk property of fluids [99]. By adopting the Langmuir film as a shear medium [100], this thesis has developed a simple and versatile alignment technique with the capability of density control [48]. In this chapter, I will first demonstrate the nanowire alignment and density control with this novel approach, and then discuss different factors that may affect the alignment process.

3.2. Overview of the alignment procedure

The alignment consists of five steps - nanowire spread, compression (optional), shear, nanowire transfer, and surfactant removal, as illustrated in Figure 3-2. First, a solvent containing nanowires and surfactant is spread on the deionized water surface to form a mixed Langmuir film, Figure 3-2a and 3-2f. Surfactant molecules can raise the surface viscosity of water to facilitate the nanowire alignment. The density of aligned nanowires can be increased when the top surface is shrunk, Figure 3-2b and 3-2g. The spread-compression process is different from the conventional Langmuir techniques in that the commonly used rectangular trough with a movable barrier is eliminated. The compression is realized by draining the water through a PTFE funnel outlet, which avoids the complex moving mechanism and provides a centrosymmetric compression [101-103]. Following the compression, a PTFE rod is spinning along the center of the funnel, generating an azimuthal flow, Figure 3-2c. Because of the small size of nanowires and the high surface viscosity, the nanowires are able to trace the flow, and the shear between the steady funnel and the rotating rod gradually aligns the nanowires along the streamlines, Figure 3-2h. After the rod stops, a receiving substrate is brought into contact with the water surface so that the aligned nanowires can be transferred (Langmuir-Schaefer deposition), Figure 3-2d and 3-2i. If the substrate is much smaller than the funnel, the nanowires will be approximately unidirectional on the substrate. The surfactant molecules are also transferred onto the substrate, but most of them can be easily removed on a hotplate, Figure 3-2e and 3-2j. Surfactant serves as a temporary shear medium. The setup in Figure 3-2 is low-cost

and easy to operate, and the clean and aligned nanowire array can be achieved in about 20 minutes. An image of the PTFE funnel is shown in Figure 3-3.

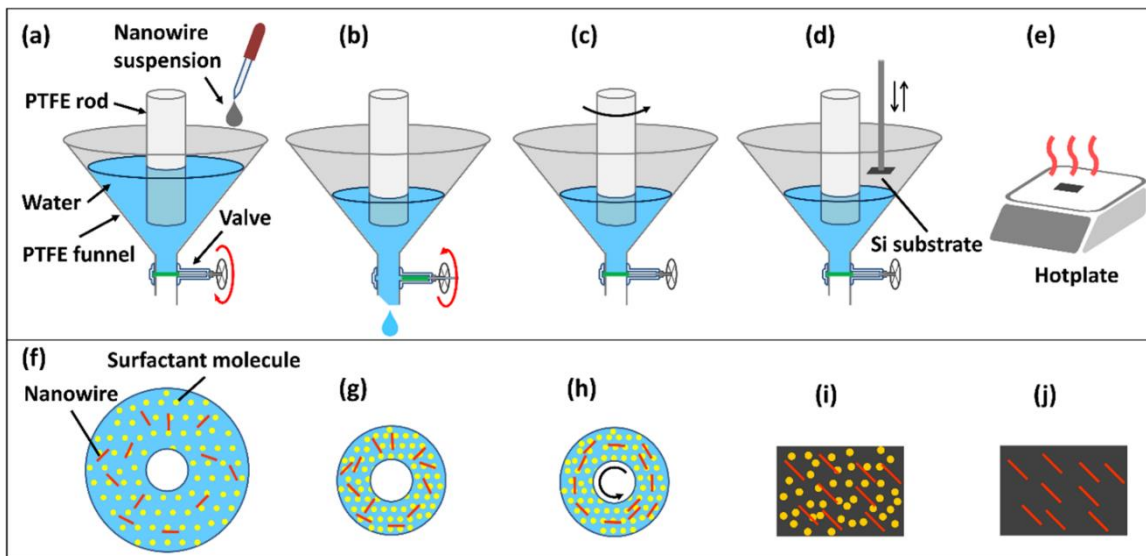


Figure 3-2. Schematic illustration of the alignment process. (a) Spread of nanowires and surfactant molecules on the water surface to form a composite Langmuir film. (b) Compression of the Langmuir film by draining the water. (c) Shear of the Langmuir film with a rotating rod. (d) Transfer of nanowires onto a receiving substrate. (e) Surfactant removal on a hotplate. (f)-(j) Top views of the water surface or substrate surface, corresponding to (a)-(e) respectively. Figures are not drawn to scale.



Figure 3-3. The PTFE funnel with a valve at the bottom. The PTFE rod connected to a motor is not shown in the picture.

Specifically, the PTFE funnel (SonomaTesting) was 70 mm in diameter and 50 mm in height, and the PTFE rod (McMaster-Carr) had a diameter of 25 mm. The surfactant was 5 mM 1-octadecylamine in hexane (both from Sigma-Aldrich). In a typical alignment, solvent (isooctane and isopropanol, 3:1 by volume, 0.2 mL) containing nanowires and surfactant solution (20 μ L) was ultrasonicated for 20 seconds for mixing, and then added onto the water surface. Depending on water surface area and ambient ventilation, the spreading solvent evaporated in 2-5 min, during which an optional compression could be performed. The shear flow was induced when the PTFE rod was rotating at 60-180 rpm, for a period of 1-3 min. After the aligned nanowires were transferred, the substrate was put on a hotplate at 95 $^{\circ}$ C for 5-15 min to evaporate the surfactant residue.

3.3. Alignment of piezoelectric nanowires

This approach can be applied to various one-dimensional nanomaterials, including piezoelectric/ferroelectric nanowires. Here we demonstrated its generality with ZnO nanorods and diphenylalanine peptide nanotubes (FF PNT). The nanostructure does not need to be hydrophobic. With a proper spreading solvent, the surface tension at the water-air interface is sufficient to support even the hydrophilic nanostructures [104]. For instance, ZnO is relatively hydrophilic.

To prepare a ZnO nanorods suspension, nanorods were synthesized on glass slides by a hydrothermal process. Briefly, ammonia solution (3.6 mL, approximately 30 wt%) was added into an aqueous solution (100 mL) of hexamethylenetetramine (10 mM) and zinc chloride (10 mM). Clean glass slides were placed floating on the top surface of the growth solution in a glass jar which was kept in an oven at 80 °C for 16-20 hours. After ZnO nanorods grew on the glass slides, they were detached from the substrates by mild ultrasonication, and dispersed in a mixed solvent of isooctane and isopropanol (3:1 by volume) [70].

Preparation of diphenylalanine peptide nanotubes suspension is modified from the method of [8]. A vial containing diphenylalanine (10 mg, Bachem, Switzerland) and water (5 mL) was put in an oven at 80 °C until the all the powder was dissolved and the white suspension became visually transparent. A second vial containing diphenylalanine (10 mg) and water (10 mL) was ultrasonicated vigorously until the white suspension became uniform without lumps. Then suspensions from both vials (2 mL and 2 mL) were mixed in a third vial and kept still overnight. The small particles from the second vial took nutrient

from the first vial and developed into longer nanotubes or bundles of nanotubes. The synthesized nanotubes were filtered out of the suspension and dispersed in a mixed solvent of isooctane and isopropanol (3:1 by volume).

Preparation of subphase for the formation of Langmuir film is also worth noting. Since ZnO nanorods are insoluble in water, deionized water was directly used as subphase. However, diphenylalanine peptide nanotubes dissolve in water, so the subphase needs to be saturated with diphenylalanine prior to the nanotube spread. Diphenylalanine (20 mg) was added into water (20 mL), followed by vigorous ultrasonication for 1 hour. The suspension was filtered, and the clear filtrate was used as subphase.

Figure 3-4a and 3-4b are the typical optical microscope images of aligned ZnO nanorods and FF PNT on silicon substrates. Insets of Figure 3-4 are scanning electron microscope images, which show that the zinc oxide nanorods are short and conical, and that FF PNT have various lengths. Therefore, the Spinning-Langmuir-Film method can align one-dimensional nanostructures with different sizes and aspect ratios.

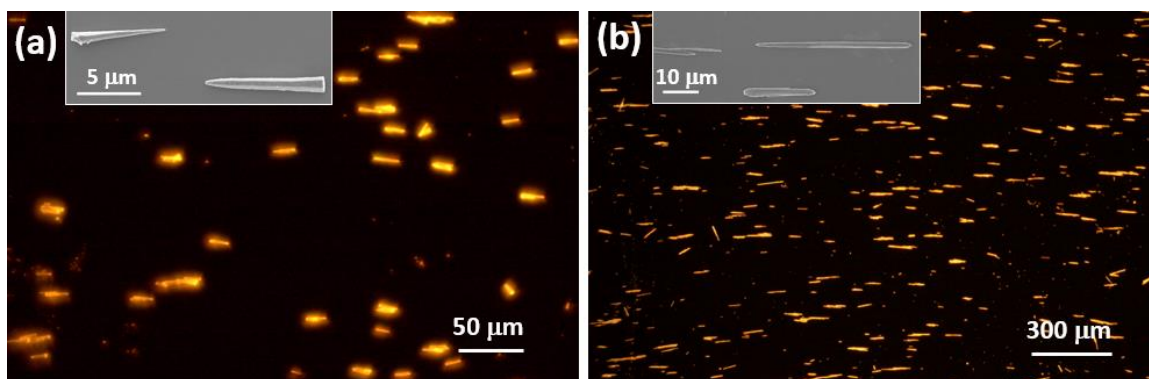


Figure 3-4. Alignment of one-dimensional nanostructures. (a) Dark-field optical microscopy image of aligned zinc oxide nanorods on a silicon substrate. Inset: Scanning

electron microscopy image of individual nanorods. (b) Dark-field optical microscopy image of aligned diphenylalanine peptide nanotubes on a silicon substrate. Inset: Scanning electron microscopy image of individual nanotubes.

3.4. Control of array density

This technique controls nanowires areal density via the height of water in the funnel. Figure 3-5 show the aligned FF PNT at relatively low (ca. $16/\text{mm}^2$), medium (ca. $41/\text{mm}^2$), and high (ca. $258/\text{mm}^2$) densities, collected at different water levels. At the low density end, this technique is a complement to the conventional Langmuir-Blodgett assembly approach [93, 94], where sparse nanowires could not be aligned due to the absence of nanowires interaction. At the other end, large area reduction from the dropping water level can produce denser array, as shown in Figure 3-5c.

In order to characterize the alignment quality, those optical microscopy images were processed by MATLAB to recognize the nanotubes and calculate their orientation with respect to the shear direction. The MATLAB code is provided in the Appendix at the end of this thesis. It should be pointed out that, all optical images had 3039-by-2014 pixels, and objects that had fewer than 80 pixels were considered particles and excluded from statistics. In addition, objects that had an aspect ratio less than 3 were not considered wire structures, and thus were excluded from statistics. Insets of Figure 3-5 are histograms showing the angular distribution of nanotubes; for all the three cases, more than 85% of the nanotubes are within $\pm 10^\circ$ of the shear direction, which is comparable to the alignment quality in Figure 3-1c and acceptable for the fabrication of piezoelectric energy harvesters.

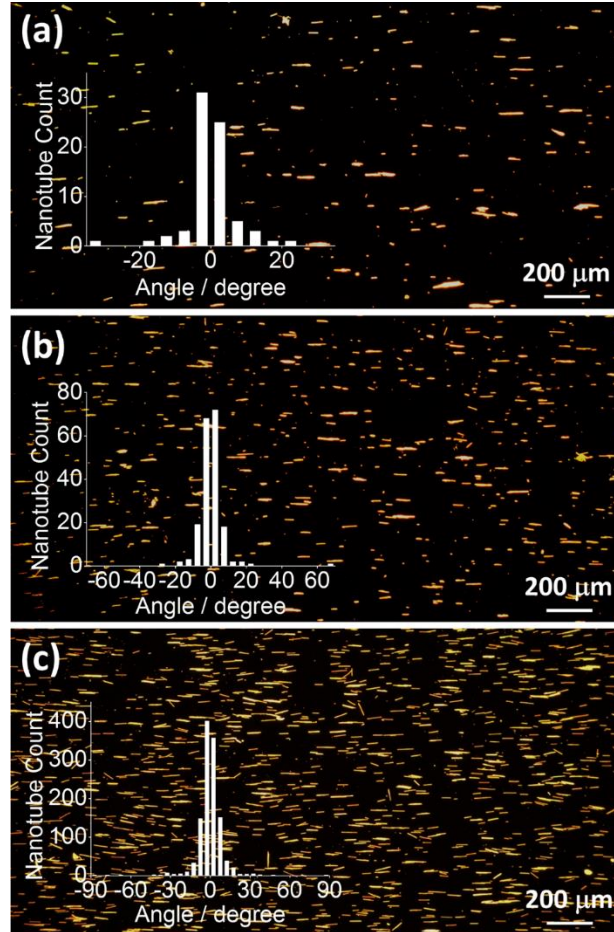


Figure 3-5. Aligned nanotubes with different areal densities through compression. (a) Low density nanotube array from a high water level in the funnel. Inset: Angular distribution of the nanotubes. (b) Medium density nanotube array from a medium water level in the funnel. Inset: Angular distribution of the nanotubes. (c) High density nanotube array from a low water level in the funnel. Inset: Angular distribution of the nanotubes.

Alternatively, the density can be controlled by adding different amounts of nanowires onto the water surface. For arrays with relatively low or medium density, this simple method can also provide uniformly aligned nanowire arrays. However, when very

dense nanowire arrays are desired, surface compression through draining water is the preferred method, because water compression reduces the probability of nanowire overlap. Figure 3-6 compared the two methods for aligning dense nanotube arrays. In Figure 3-6a, when many nanowires were added during the spread stage, some of them overlapped with each other. In contrast, Figure 3-6b shows that the dense array from water surface compression has much fewer overlapped nanotubes. Starting with a sparse array ensures the formation of monolayer nanowires on the water surface.

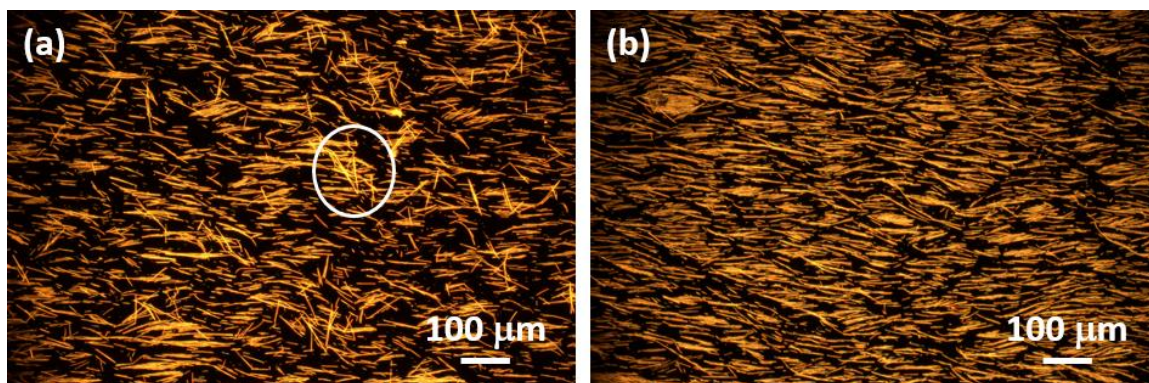


Figure 3-6. Relatively high density arrays obtained by two different methods. (a) Dense nanotube array obtained by adding a large amount of nanotubes directly onto a small water surface A_1 ; the circle indicates an area with overlapped nanotubes. (b) Dense nanotube array compressed from a larger water surface A_2 to the smaller area A_1 ($A_2/A_1=1.7$). In (a) and (b), the same amount of nanotubes were added.

3.5. Effect of receiving substrates

It is important to transfer the aligned nanostructures onto desired substrates for device fabrication. For flexible energy harvesters, polymer substrates should be used.

Various substrates have been tried as the receiving substrates, including silicon, silicon with native oxide, glass slide, Kapton polyimide film, polyethylene terephthalate (PET) film, and PET film coated with copper. The alignment of FF PNT on those substrates is shown in Figure 3-7.

Whether the nanostructures can be transferred depends on the adhesion between the nanostructures and the substrate, or in case that the surfactant bonds to the surface of the nanostructures, it depends on the adhesion between the surfactant and the substrate. Therefore, due to the different chemical compositions of the surfaces, some nanostructures/surfactants may adhere poorly to certain substrates. On most of the substrates we have tried, the nanotube transfer was successful and consistent, including the relatively hydrophobic silicon, Kapton, and PET, and the relative hydrophilic glass slide and PET coated with copper. However, when using the silicon with native oxide, sometimes not the whole substrate was covered by the nanotubes.

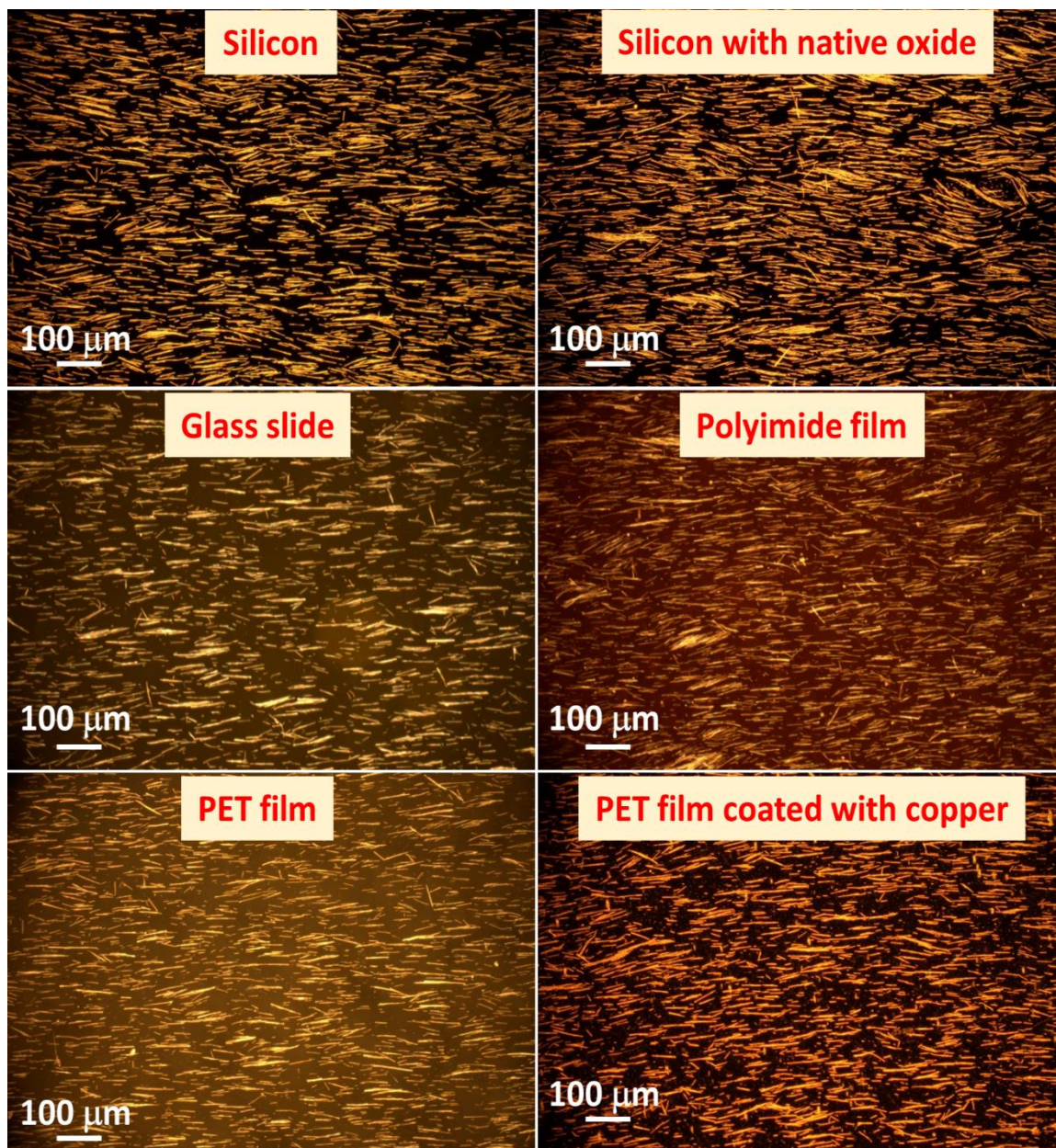


Figure 3-7. FF PNT transferred onto different types of substrates after the alignment. Note that for the PET film coated with copper, some ‘particles’ in the image are actually the surface roughness of the PET film.

3.6. Effect of surfactant

The shear force on the water surface is critical to achieve the unidirectional alignment. In Figure 3-8a, the Langmuir film was simply compressed to a high density monolayer without rotation of the PTFE rod. There is no obvious long-range orientation in the array, whereas some short-range alignment is present due to the interaction between adjacent nanotubes.

Without surfactant, the rotation alone cannot induce the alignment either. The role of surfactant must be emphasized here. Before the added surfactant reaches a threshold amount, the surface viscosity is insufficient so that the nanowires would move freely and aggregate on the water surface without alignment. The quality of alignment with different amounts of surfactant being added has been characterized. The result is given in Figure 3-8b. When the surfactant is less than 8 μL (ca. 20 molecules/ nm^2 on the water), nanotubes have random orientation and agglomeration is observed after the shear, as shown in Figure 3-8c. When the surfactant amount is increased into the transition region, the agglomeration is significantly reduced and the dispersed nanotubes start to be oriented in the shear flow direction, Figure 3-8d. When the surfactant amount exceeds the transition region, the agglomeration completely disappears and the dispersed nanotubes are well aligned, as shown in Figure 3-8e. Therefore, the high viscosity from the surfactant not only aligns the nanotubes but also prevents them from aggregating.

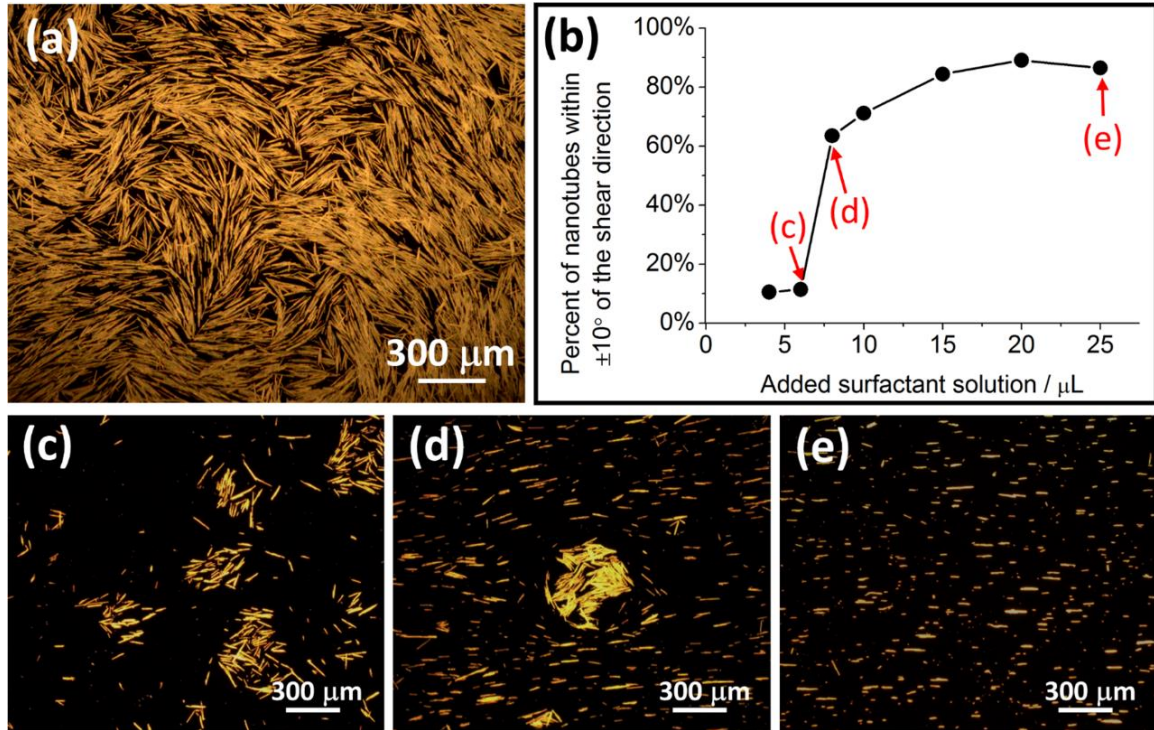


Figure 3-8. Shear effect on the nanotubes alignment. (a) Compressed monolayer of nanotubes without shear. (b) Relationship between the quality of alignment and the amount of added surfactant. A higher percentage of nanotubes within $\pm 10^\circ$ of the shear direction indicates a better alignment. (c) Nanotubes after shear alignment with 6 μL surfactant. (d) Nanotubes after shear alignment with 8 μL surfactant. (e) Nanotubes after shear alignment with 25 μL surfactant.

After the alignment and transfer, a good interface between the nanostructures and other materials is critical for the device fabrication. Therefore, surfactant adsorbed on the surface of the nanostructures and the substrate must be removed, otherwise it could become a contamination and adversely affect the device performance. The sample is simply baked on a 95 $^\circ\text{C}$ hotplate to evaporate the 1-octadecylamine, and the removal of the surfactant

layer can be observed under an optical microscope. More careful and quantitative investigation has also been conducted by measuring the surface roughness of substrates with Atomic Force Microscope. In Figure 3-9, (a) is from the surface of a clean silicon substrate, (b) is from the silicon contaminated with the surfactant, and (c) is from the contaminated silicon baked at 95 °C for 15 min. The surfactant formed some microstructures on the silicon in Figure 3-9b, which disappeared in Figure 3-9c after the baking. For each kind of sample, we have scanned 5 different points, and the average surface roughness (R_a) is 402 pm, 930 pm, and 403 pm, respectively, indicating that the 95 °C baking had restored the original surface of the silicon substrate.

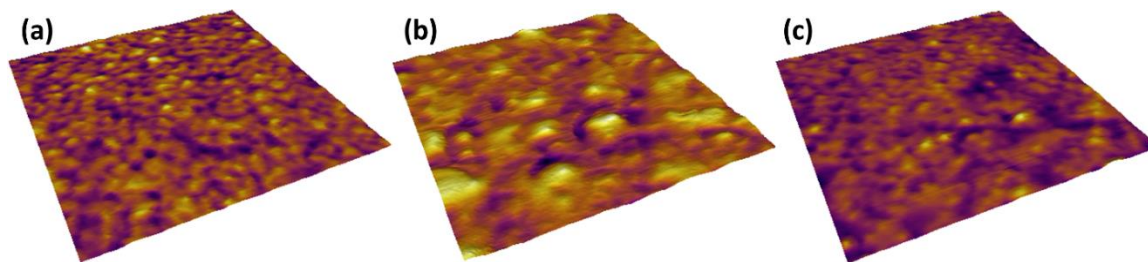


Figure 3-9. Atomic Force Microscope images of the silicon surface. (a) The surface of a clean silicon substrate. (b) The surface of a silicon substrate contaminated with the surfactant. (c) The surface of a contaminated silicon substrate that was baked at 95 °C for 15 min. The scan area is a 500 nm by 500 nm square.

Simple electrical measurement was also performed to make sure that surface of the nanostructure is clean for electrical contact after the removal of surfactant. Aligned zinc oxide nanorods were tested with conductive Atomic Force Microscopy (c-AFM). As illustrated in Figure 3-10a, an AFM platinum probe forms one electrical contact with the nanorod, while the silicon substrate serves as the bottom electrode. The current-voltage

curve of the nanorod in Figure 3-10b shows rectifying characteristics, which is due to the Schottky barrier between n-type zinc oxide and platinum. The electric characterization confirmed that the aligned nanorod formed good electrical contacts with both the metallic probe and the silicon substrate.

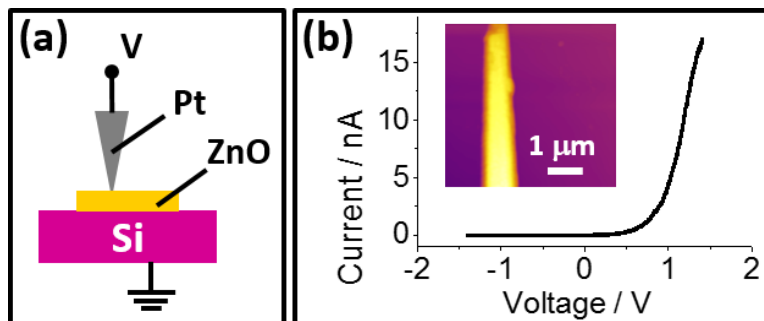


Figure 3-10. Electrical test of aligned nanostructure after baking. (a) Schematic diagram showing the electrical characterization of aligned zinc oxide nanorods based on Atomic Force Microscopy. (b) A typical current-voltage curve of a nanorod. Inset: Topographical scan of the nanorod on the silicon substrate.

The surface roughness measurement and electrical test above show that at least most part of the surfactant could be removed by the baking. However, it is possible that on the surface of silicon substrates or the nanostructures, there are surfactant molecules coordinatively bonded to the surface. Those bonds may be stronger than the hydrogen bonds among surfactant molecules, and therefore could not be broken under the 95 °C baking. In that case, short exposure to an oxygen plasma is recommended to clean the surface.

3.7. Effect of spin speed and spin duration

Figure 3-11 shows alignment of FF PNT with nine different rotation speeds of the PTFE rod, from about 61 rpm to 424 rpm. The corresponding shear rate is from about 7 s^{-1} to 51 s^{-1} . There is no explicit correlation between the shear rate and the quality of alignment, as nanotubes are all aligned to the shear direction in the nine images. However, the density of nanotubes after alignment is lower at high rotation speeds (312 rpm, 370 rpm, and 424 rpm). At a high speed, the water surface became wavy, which possibly caused some nanotubes to sink. Therefore, a moderate spin rate in the range of 60-180 rpm was applied in most experiments.

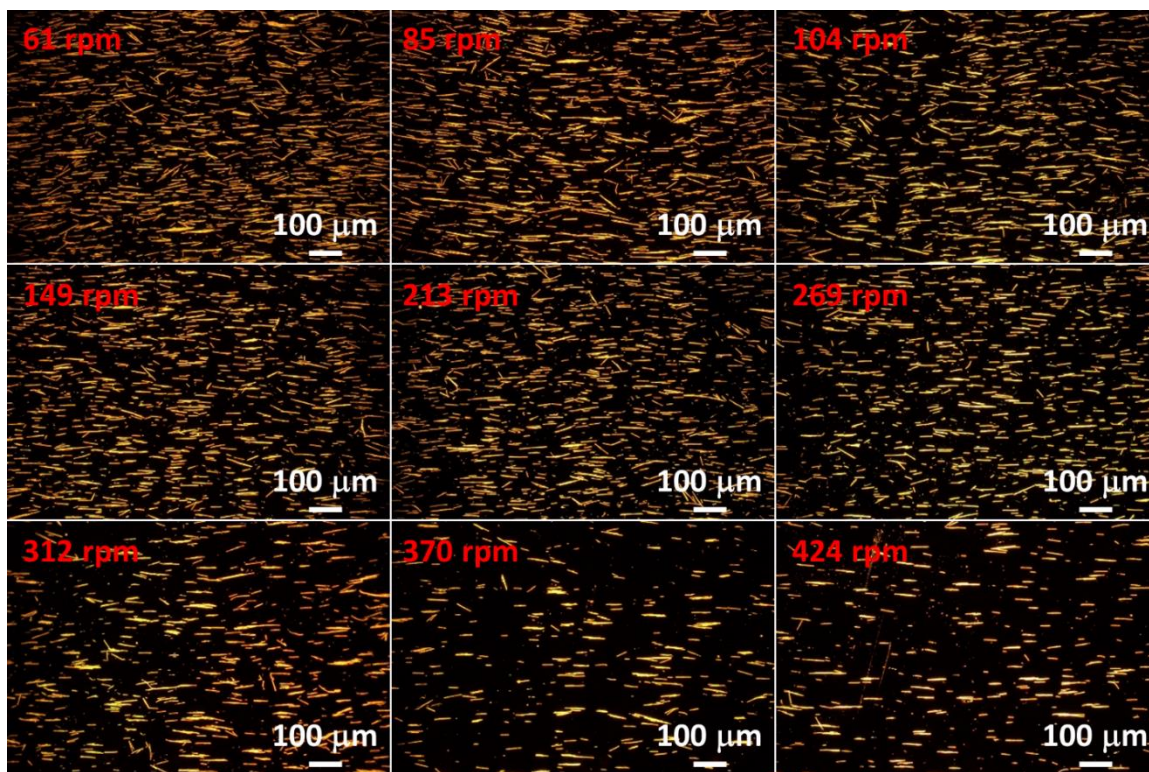


Figure 3-11. Alignment of FF PNT with different spin speeds. The spin duration was 2 min in all cases.

Following the study on the spin rate, the effect of spin time was investigated, and Figure 3-12 shows the result. The PTFE rod was kept at a low speed of 61 rpm, so that development of the alignment over time could be observed. As shown in Figure 3-12a, without any spinning, the nanotubes were randomly oriented on the water surface. After only 10 sec of spinning, the nanotubes were aligned over the whole water surface (Figure 3-12b). As the spinning time was reduced to 1 sec (one revolution of the PTFE rod), only those nanotubes near the PTFE rod were aligned and most nanotubes were randomly oriented (Figure 3-12c and 3-12d). When the spinning time was 2 sec, the area of aligned nanotubes increased (Figure 3-12e and 3-12f). Therefore, the alignment starts from the area adjacent to the rotating rod and moves toward the steady funnel wall with a speed of a few millimeters per second.

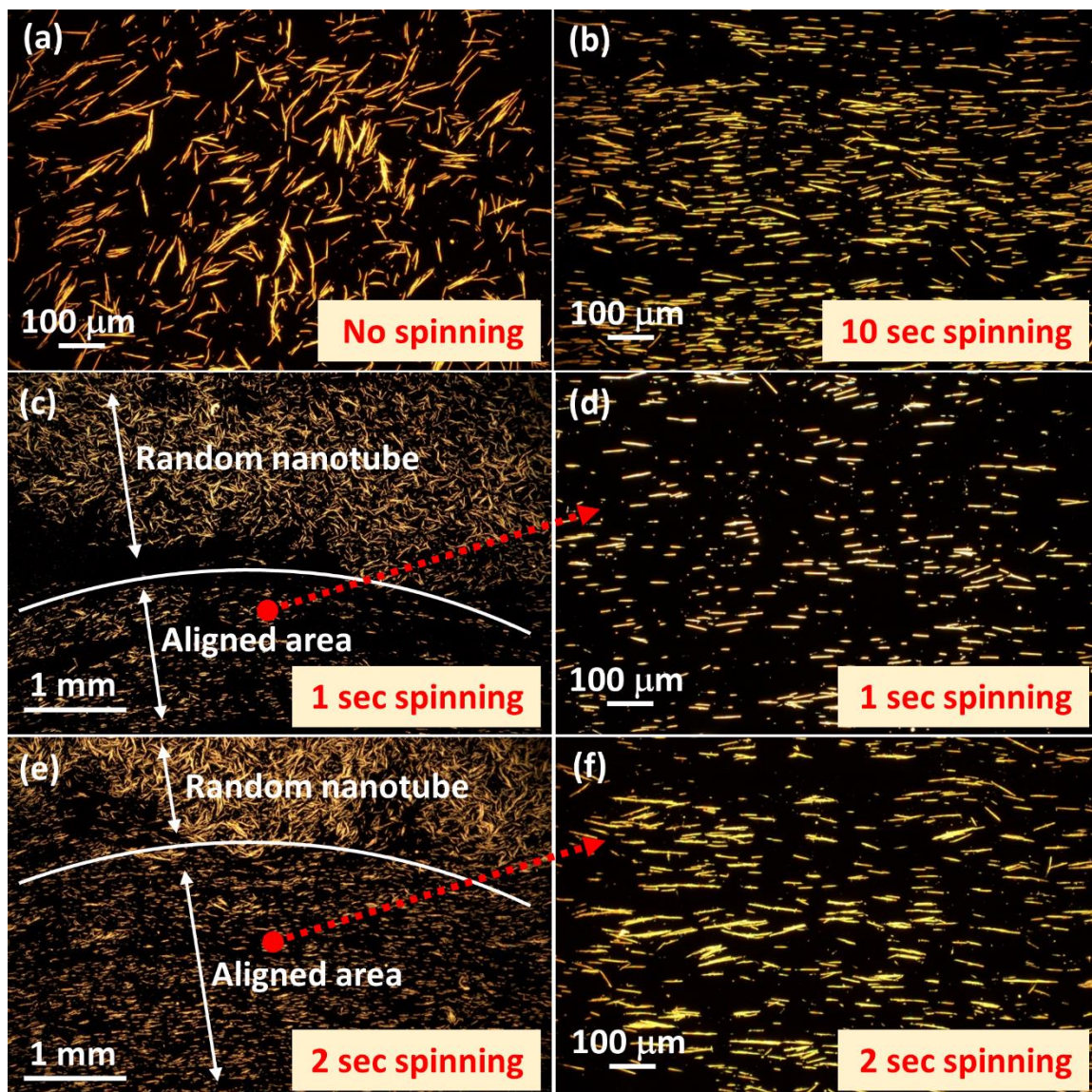


Figure 3-12. Nanotube array after different durations of spinning. (a) Random nanotubes before spinning alignment. (b) Nanotubes after 10 sec of spinning; nanotubes were aligned over the whole water surface. (c) Partially aligned nanotubes after 1 sec spinning; the boundary between aligned area and unaligned area is indicated by a curved line. (d) The

aligned area in (c) at a higher magnification. (e) Partially aligned nanotubes after 2 sec spinning; the aligned area has grown. (f) The aligned area in (e) at a higher magnification.

3.8. Discussion and future work

(1) Alignment of ferroelectric nanowires

The motivation of developing such a low-cost and general alignment technique is to align piezoelectric nanowires for applications in energy generation. However, ZnO nanorods and FF PNT demonstrated in this work cannot be used to fabricate an energy harvester. Although both of them are piezoelectric, they are not ferroelectric, which means their direction of polarization cannot be changed by an external electric field (poling process). For individual ZnO nanorod and FF PNT, its polar direction is fixed after the crystal growth. The Spinning-Langmuir-Film method is not able to align their polar directions to the same side. Therefore, a composite material fabricated from such an array will barely show a macroscopic piezoelectric property.

Ferroelectric nanowires, such as BaTiO₃, PZT, and NaNbO₃, need to be synthesized in the future to fabricate a high-output energy harvester. After alignment, transfer, and electrodes deposition, the polar directions of the nanowire array can be switched by a poling process to the same direction.

(2) Stick-slip phenomenon

Compared with the conventional Langmuir trough with a movable barrier, a distinguishing trait of the conical trough is the movement of the three-phase contact line during the compression. As illustrated in Figure 3-13, we observed a “stick-slip” behavior

when the contact line was moving along the funnel, indicating the pinning of the contact line [105]. The pinning force is due to the surface roughness and/or the chemical heterogeneity of PTFE [106, 107], and it caused the nanowire monolayer to deposit on the funnel wall before high-density nanowires formed on the water surface. The stick-slip problem can be mitigated by keeping a layer of nonpolar solvent, such as isooctane (the one in the spreading solvent), on top of the water during the compression. The nonpolar solvent is believed to wet the PTFE and serve as a “lubricant” at the contact line [108, 109], such that the nanowire array can be compressed smoothly until they are closely packed.

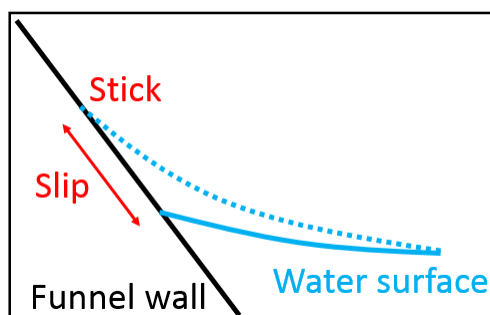


Figure 3-13. “Stick-slip” behavior of the contact line when the water surface is descending.

(3) Higher density alignment

As shown in Figure 3-8a above, FF PNT array can be compressed until there is little open space between nanotubes. However, because the nanotubes are packed side by side, it is very difficult for individual nanotube to adjust its position to accommodate the shear force. Thus, even for alignment with high density, the nanotubes were not compressed to the extreme extent; instead, some space between nanotubes was left so that they had room to rotate. That aspect limited the highest areal density this method achieved.

If the alignment is performed before the compression, it is possible to produce densely packed array with good alignment. However, due to the stick-slip effect, the compression requires a layer of solvent covering the water surface. The solvent reduces the surface viscosity and makes the nanowires randomly oriented immediately. Alignment is impossible when the solvent is on top of the water surface. In order to solve the dilemma, the next step is to reduce the surface roughness and chemical heterogeneity of PTFE, or to find a new hydrophobic material to replace PTFE, so that the stick-slip effect can be avoided without applying a solvent on the water surface.

(4) Alignment distribution on the entire water surface and further scale-up

In a typical alignment, the PTFE rod is concentric with the PTFE funnel, and the width of the water surface for nanowire alignment is 10 mm. During nanowire transfer, the rectangular silicon substrate (8 mm by 10 mm) is brought to the water surface with the longer edge tangent to the circular water edge. To characterize the alignment distribution on the water surface, we collected three representative samples at different locations. The schematic drawing is shown in Figure 3-14a.

On the silicon substrate, the transferred nanotubes form three zones. The zone close to the PTFE rod and the zone close to the PTFE funnel have sparse or no nanotubes, while the middle area of the substrate contains aligned nanotubes along the shear direction with the best uniformity. The aligned zone is approximately 6 mm wide. Such a distribution might be due to the convex menisci at the water boundaries, and further investigation is needed for confirmation. Figure 3-14b to Figure 3-14g show the alignment at three

different points (Pt1, Pt2, and Pt3) on the substrate. The nanotubes are aligned in the tangential direction along the ring. Fig. 3-14d and Figure 3-14f also show how the nanotubes become sparse near the PTFE rod. The other two silicon substrates have a similar distribution of nanotubes. Therefore, the zone with well aligned nanotubes is a 6 mm wide ring.

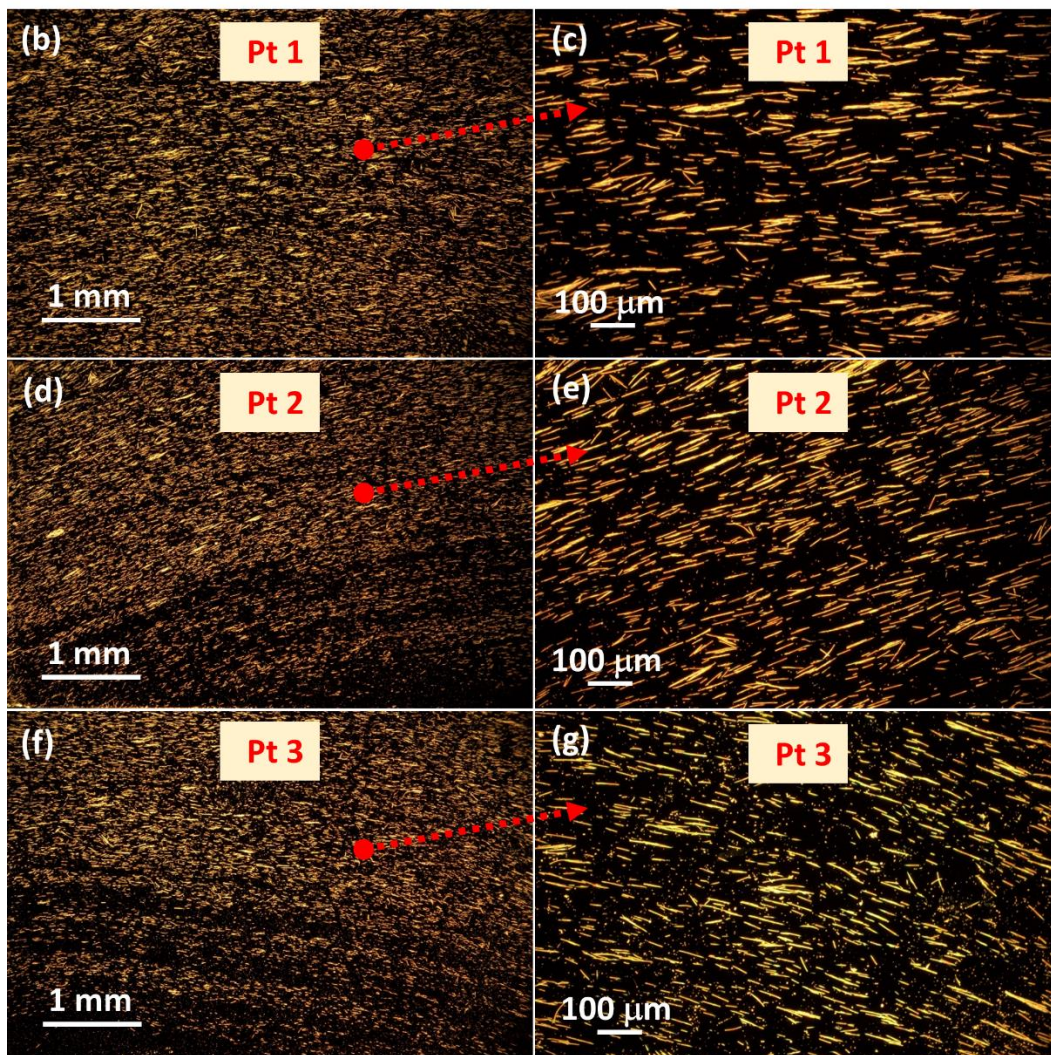
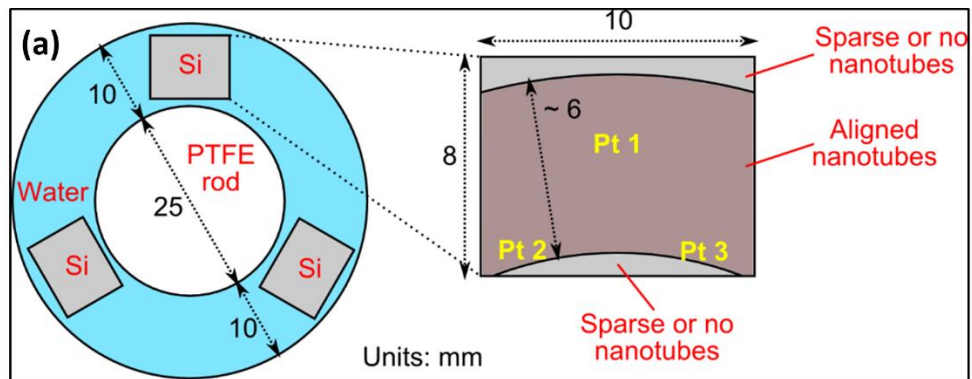


Figure 3-14. The alignment of nanotubes on the entire water surface. (a) Schematic drawing showing the water surface and the receiving silicon substrates. The optical images of the aligned nanotubes at points Pt1, Pt2, and Pt3 are provided at lower magnifications in (b), (d), and (f), and higher magnifications in (c), (e), and (g), respectively. Note that (e) and (g) are from the dense area in (d) and (f).

In terms of scalability, the size of substrates is mainly limited by the width of the water surface ring rather than its length. Increasing the ring width is not straightforward, as it may cause instability of the flow field. Reynolds number (R_e) of the flow field has the following expression:

$$R_e = \frac{\rho \bar{U} L}{\mu}$$

where ρ is the density of fluid, \bar{U} is the mean velocity of the flow, L is the characteristic length, and μ is the viscosity of the fluid. Here L depends on the gap between the PTFE funnel and the PTFE rod. As the gap becomes wider, R_e increases, and water is more vulnerable to external disturbance and may produce a turbulent flow field. An unstable flow often results in to poor alignment quality.

In the current setup, the PTFE rod is not precisely centered with the motor, and during the rotation the rod is wobbling laterally and shaking the water. For the next step, in order to scale up the alignment area without introducing turbulence, rotation of the rod must be smoother and kept at a low rate.

(5) Unidirectional alignment

With the circular funnel and rod, the nanowires are aligned along the tangent direction of the water flow. If the substrate is large, the distribution of nanowires on the substrate will not be unidirectional. To solve this problem, a different setup is proposed in Figure 3-15. The container is no longer circular, and the PTFE rod is replaced by a PTFE belt driven by two shafts. In the straight segments of the flow path, the nanowires will likely be aligned uniformly to the same direction.

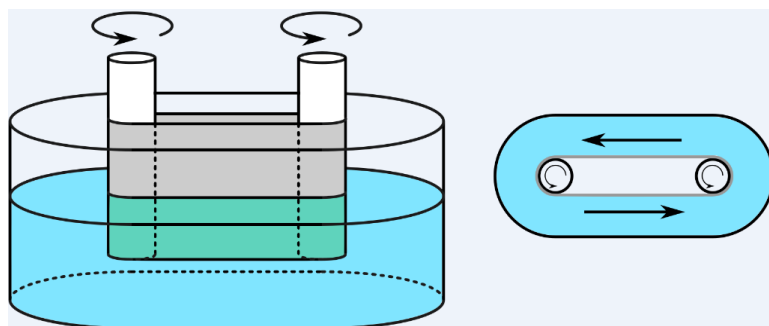


Figure 3-15. Shear flow induced by a PTFE belt to provide unidirectional alignment.

CHAPTER 4. SEPARATION OF THE PIEZOTRONIC EFFECT AND THE PIEZORESISTIVE EFFECT

4.1. Introduction

The phenomenon that a mechanical strain can affect the charge carrier transport plays important roles in various fields including artificial skin [110], human-machine interface [111], strain engineering [112], etc. As mentioned in Chapter 1, for a homogeneous material with electrodes, three mechanisms may alter its transport characteristics - the geometric change, the piezoresistive effect that changes the material resistivity [113], and the piezotronic effect that changes the interfacial barrier between the material and the electrode [21, 26].

Piezoresistance roots in the bending/splitting of electronic band structures under strain and is significant in semiconductors like silicon nanowires [114, 115]. Unlike piezoresistance, piezotronic effect only appears in semiconductors with a non-centrosymmetric crystal structure, such as wurtzite ZnO and GaN, or a single atomic layer of MoS₂ [116]. In those materials, piezoelectric charges control the barrier height at the metal-semiconductor interface and modulate the carrier transport [36, 117, 118]. The single crystal ZnO nanowire is the most studied piezotronic material, due to its simple synthesis [3, 61], flexibility [119], and robustness [18, 120]. Piezotronic nanowire devices demonstrate superior strain sensitivity and have wide applications in strain-gated transistors [35, 121, 122], tactile sensor array [123], logic circuits [124], memories [125],

etc. Figure 4-1 shows strain sensors based on a lateral ZnO nanowire [124] and a free-standing ZnO nanowire [126] in the literature.

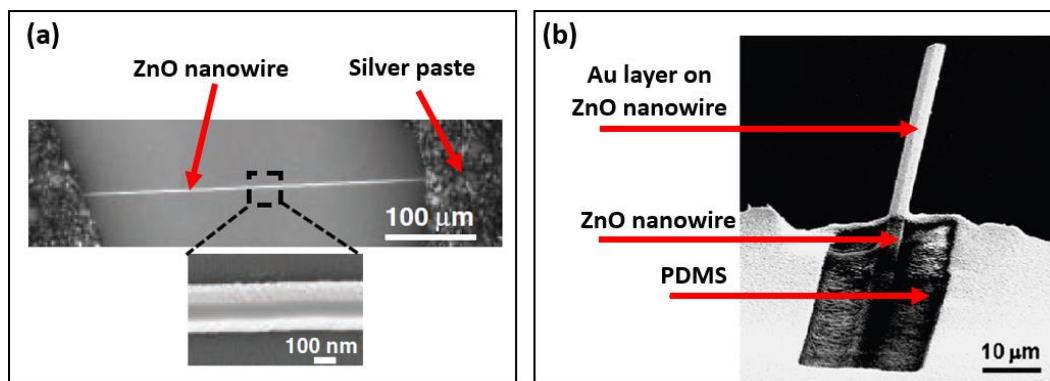


Figure 4-1. SEM images of ZnO nanowire strain sensors in the literature. (a) A lateral ZnO nanowire that senses the tensile strain; two electrodes are made from silver paste. Reprinted with permission from [124]. Copyright 2010 WILEY-VCH Verlag GmbH & Co. KGaA, Weinheim. (b) A free-standing ZnO nanowire that detects bending strain; silver paste (not shown) at the root of the nanowire is the bottom electrode, and gold layer on the top of the nanowire is the other electrode. Reprinted with permission from [126]. Copyright 2009 American Chemical Society.

A typical piezotronic device consists of a ZnO nanowire and two metal electrodes on the ends. Consequently, the change of transport characteristics under strain combines the piezotronic effect at two contacts and the piezoresistive effect in the nanowire (the geometric influence is relatively small and can be neglected). Previous studies assumed that the piezotronic effect dominated the current transport because of the asymmetric current change at forward and reverse biases [123, 127]. Figure 4-2 from [128] shows current-voltage characteristics of a ZnO nanowire under different strain conditions: no

strain (black curve), compressive strain (green curve), and tensile strain (red curve). A tensile strain increased the current at a positive bias, but decreased the current at a negative bias. Such a phenomenon could not be explained by the piezoresistive effect, which simply changes the resistivity and raises/reduces the forward current and reverse current in the same way. Therefore, the asymmetric change from the black curve to the red curve implied that the piezotronic effect was dominant. However, from the green curve in Figure 4-2, a compressive strain decreased the forward and reverse current at the same time. It is not clear if the current change was due to the piezoresistive, the piezotronic effect, or both.

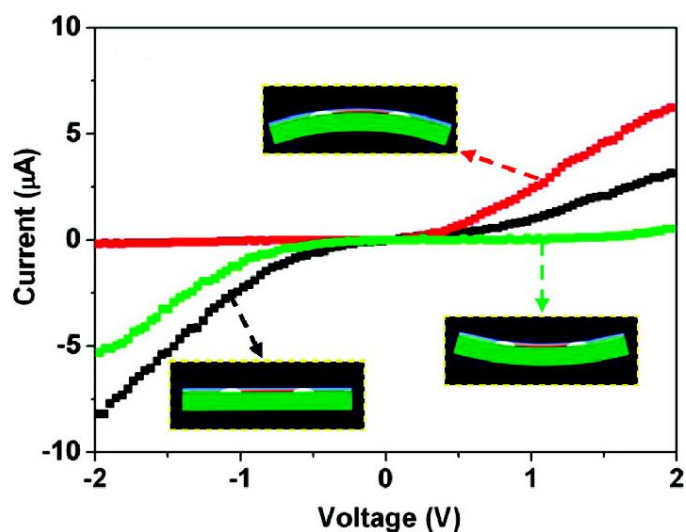


Figure 4-2. Current-voltage curves of a ZnO nanowire strain sensor under different strain conditions in the literature. Black curve: no strain. Green curve: compressive strain. Red curve: tensile strain. Reprinted with permission from [128]. Copyright 2008 American Chemical Society.

To the best of our knowledge, in the literature there is no report on the piezoresistance of ZnO nanowires, and quantitative comparison of piezotronic and

piezoresistive effects is still lacking. Therefore, it is necessary to develop a general method which can separate those effects and reveal the strain-dependent transport characteristics of individual contacts and the nanowire itself.

4.2. Principle

Four-point measurement is a standard technique to eliminate the contact resistance during the resistivity measurement. As shown in Figure 4-3, the current is forced through probe 1 and probe 4, and the voltage between probe 2 and probe 3 is sensed. Because the voltmeter has a large internal impedance compared to the sample under test, there is almost no current flowing from probe 2 to probe 3, and therefore the voltage drop at the contacts and lead wires is negligible. Only the resistance of the sample between probe 2 and probe 3 is measured.

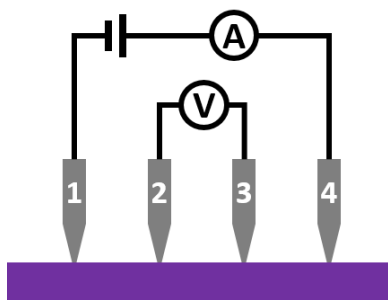


Figure 4-3. Schematic diagram of a four-point measurement circuit.

In a ZnO nanowire device, the contact resistance is mainly from the Schottky barrier. The change of contact resistance under strain represents the change of Schottky barrier height, i.e. the piezotronic effect. On the other hand, the change of the nanowire volume resistance is mainly from the piezoresistive effect. Based on that principle, in this

chapter a modified four-point measurements is configured on a single ZnO nanowire to separate the two effects [49].

4.3. Device fabrication

Separation of the two effects is based on a multi-terminal nanowire device. An ideal ZnO nanowire for device fabrication should be long enough to accommodate multiple electrodes on it, and at the same time thin enough so that it could be strained easily. Chemical vapor deposition (CVD) was utilized to synthesize the nanowire. The growth process was similar to the one used in Chapter 2, but some parameters were modified to ensure the nanowire has a small diameter. First, graphite was used as the carbon source instead of activated carbon powder to slow down the production of zinc vapor. One gram of mixture was used as the source material. Second, the gas flow rate was reduced to 15 sccm for Ar and 5 sccm for O₂, and the tube pressure was increased to 60 Torr. Third, the growth time at 960 °C was increased to 30 min. Other parameters were the same with Table 2-1. Figure 4-4 are the SEM images of ZnO nanowires with proper size for device fabrication. In most cases, lengths are more than 100 μm and diameters are between 300 and 800 nm.

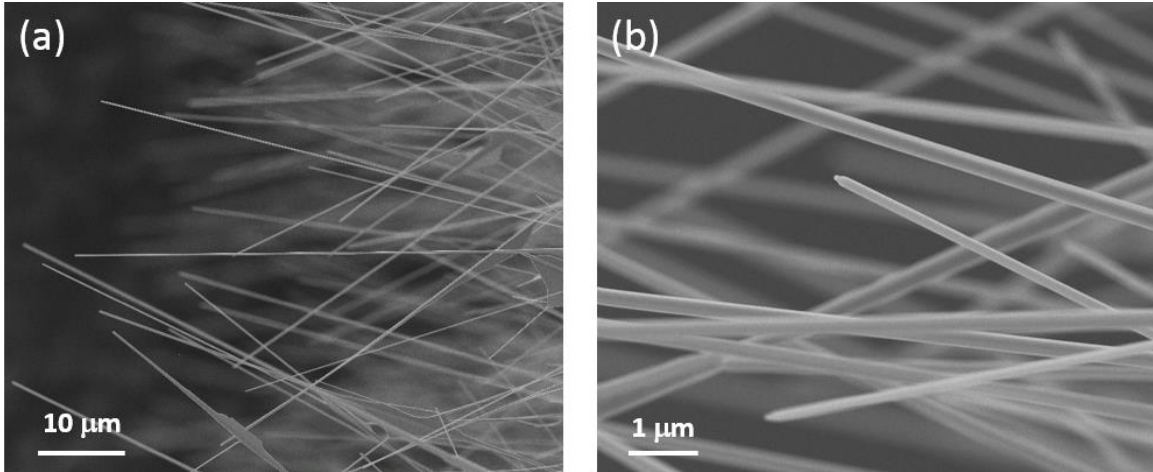


Figure 4-4. SEM images of ultra-long ZnO nanowires synthesized by CVD. (a) Low magnification. (b) Higher magnification.

As-synthesized nanowires were transferred with a sharp probe from the growth substrate onto flexible polyethylene terephthalate (PET) substrates with a thickness of 200 μm, as illustrated in Figure 4-5a. Prior to the electrodes deposition, a 200 nm SU-8 layer was spin-coated on the substrate and cross-linked by hard bake and UV exposure. SU-8 produced a non-conformal coverage around the nanowire, Figure 4-5b and 4-5c. The SU-8 was thicker on the two sides of the nanowire than on the top, so a short oxygen plasma ashing could expose the top part of the nanowire while the SU-8 on two sides remained, Figure 4-5c. The SU-8 film, called a lifting layer [129, 130], planarized the step between the nanowire and the substrate for electrodes deposition, Figure 4-5d. Without the lifting layer, deposited metal is very likely to be discontinuous at the step, Figure 4-5e. More importantly, it also anchors the nanowire to the substrate and transfers the strain from the substrate to the nanowire during the test.

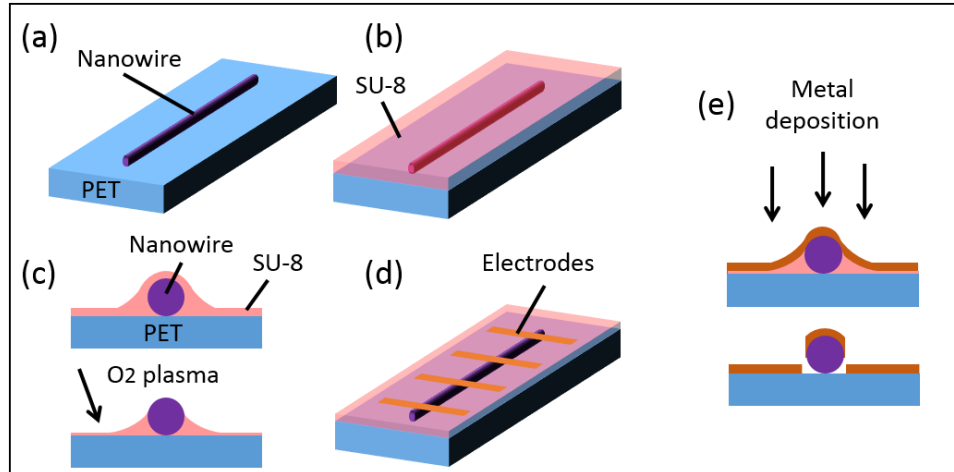


Figure 4-5. Fabrication of the multi-terminal device with a ZnO nanowire. (a) Schematic diagram of a nanowire transferred onto a polymer substrate. (b) An SU-8 layer is spin-coated on the substrate. (c) An oxygen plasma ashing exposes the top part of the nanowire. (d) Electrodes are deposited on the exposed nanowire through photolithography. (e) Electrodes deposition with and without the SU-8 lifting layer.

Figure 4-6a is an AFM image of a thick wire surrounded by a lifting layer on the substrate. The inset of Figure 4-6a plots a cross section of the AFM scan, in which the exposed part of the wire and the two SU-8 slopes are distinguishable. It is worth noting that the lifting layer process is self-adaptive, as the same coating and ashing parameters worked successfully for wires with different diameters. As an example, Figure 4-6b is a confocal optical microscopy image of a nanowire with a lifting layer. From left to right, the nanowire becomes thinner, and the surrounding SU-8 also gets thinner correspondingly.

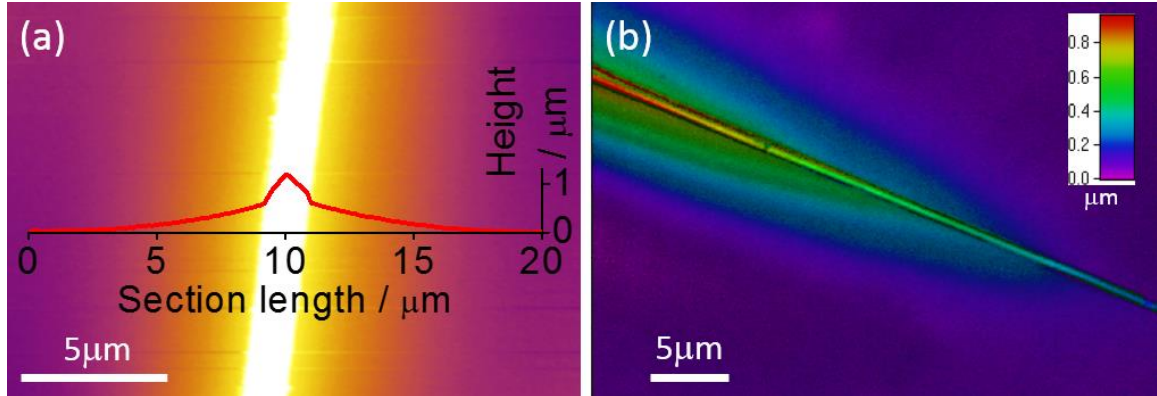


Figure 4-6. Characterization of the SU-8 lifting layer. (a) Atomic Force Microscopy image of a nanowire in SU-8 lifting layer with top part exposed; the inset shows a section view of the scan. (b) Confocal optical microscopy image of a nanowire in SU-8 lifting layer; the color represents height in the direction perpendicular to the page.

After applying the lifting layer, metal electrodes were patterned on the ZnO nanowire with a photolithography liftoff process, using NR9-1500PY as the photoresist. More details on the liftoff process will be provided in Section 4.8 below. Next, 100 nm titanium, 200 nm copper, and 10 nm gold were deposited through evaporation as the electrode. The titanium layer formed the electrical contact with the nanowire, the thick copper layer improved the mechanical strength of the electrodes, and the thin gold layer prevented the electrodes oxidation. Then the device was soaked in a solvent to lift off the unwanted metal. It should be pointed out that fully cross-linked SU-8 lifting layer is a permanent epoxy and resistant to the chemicals used in the photolithography and liftoff process. Lastly, a layer of SU-8 was coated on the device and cross-linked to protect the nanowire and electrodes.

The final device has a series of electrodes on a secured ZnO nanowire, as shown in Figure 4-7. And the process details are summarized in Table 4-1.

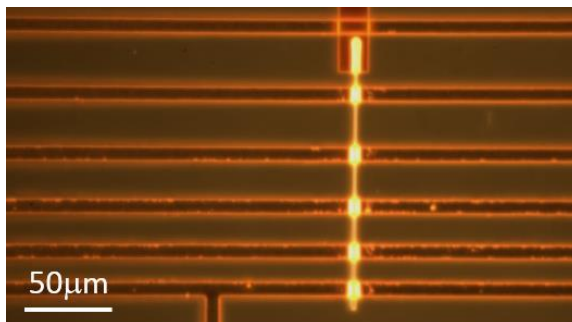


Figure 4-7. Optical microscope image of a final device. The shiny vertical line is the ZnO nanowire.

Step	Description
Nanowire transfer	1 Cut PET substrates and clean them in solvent and deionized water
	2 Further clean PET substrates in a plasma asher
	3 Transfer a ZnO nanowire onto the PET substrate
Lifting layer	1 Prepare a diluted SU-8 solution by mixing SU-8 2002 (MicroChem) and cyclopentanone, 3:2 by volume
	2 Prebake the substrate to remove moisture, 115 °C, 2 min
	3 Spincoat diluted SU-8 onto the substrate, 3000 rpm, 30 sec
	4 Softbake the substrate to remove solvent, 95 °C, 2 min
	5 UV exposure to cross-link SU-8, 30 sec (Karl Suss MA-6 Aligner)
	6 Post-exposure bake, 95 °C, 2 min
	7 Hard bake to fully cross-link SU-8, 120 °C, 5 min
	8 Oxygen plasma etching of SU-8 to expose the top surface of the nanowire, etched about 200-250 nm in 3 min
Lithography	1 Prebake, 115 °C, 2 min
	2 Spincoat NR9-1500PY (Futurrex), 3000 rpm, 40 sec
	3 Softbake, 130 °C, 5 min
	4 UV exposure, 20 sec (Karl Suss MA-6 Aligner)
	5 Post-exposure bake, 100 °C, 3 min
	6 Development in RD6 (Futurrex), 12 sec

	7	Rinse in deionized water, blow dry, and inspect
Metal deposition	1	Clean the surface of ZnO in a plasma asher
	2	Metal deposition by evaporation, 100 nm Ti, 200 nm Cu, 10 nm Au
Metal liftoff	1	Strip photoresist in RR5 (Futurrex), overnight
	2	Rinse in isopropanol and deionized water, blow dry, and inspect
Packaging	1	SU-8 spincoating and cross-linking

Table 4-1. Device fabrication procedure in details.

4.4. Measurement system

After device fabrication, the voltage-current curves of nanowires were obtained with an AC/DC current source (Keithley 6221) and a nanovoltmeter (Keithley 2182A). The current source and the voltmeter can communicate with each other to perform automatic measurement on the nanowire device. As shown in Figure 4-8a, the RS-232 cable between 6221 and 2182A transfer commands and measurement data, and the Tigger Link cable synchronizes the operation of two instruments. Figure 4-8b illustrates the operation mode. 6221 supplies a series of current pulse to the device, and the pulse height, pulse width, and pulse interval can be defined. Within each pulse, the 2182A waits until the voltage is stable and then performs the measurement. Using pulses instead of continuous current signal, the heat generation on the device is minimized, which is beneficial for the measurement on some temperature-sensitive devices.

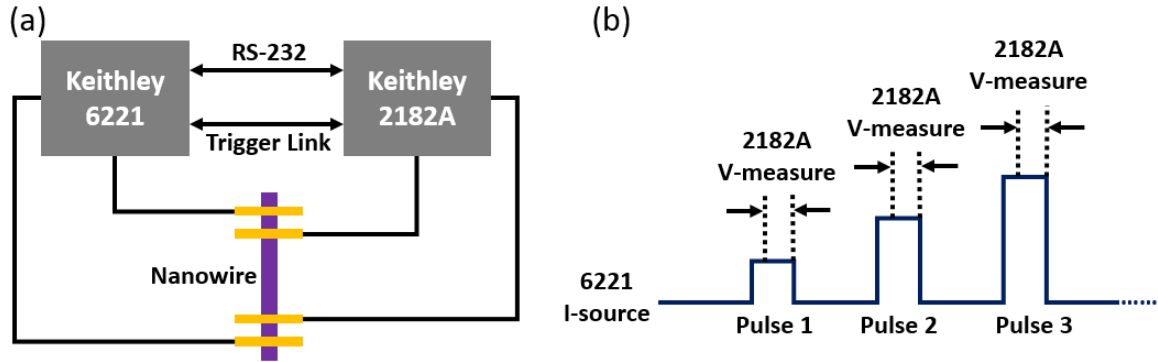


Figure 4-8. Measurement setup. (a) Measurement system configuration. (b) Pulse measurement mode.

4.5. Piezoresistive effect of ZnO nanowires

Ideally, metal electrodes on a ZnO nanowire form either rectifying Schottky contact or linear Ohmic contact, solely determined by their work functions. In reality, the contact depends on the surface condition, crystallinity, and chemical reaction as well, and thus the contact can have more varieties [131]. By using titanium as the electrodes, both linear Ohmic contacts and nonlinear barrier contacts were obtained on ZnO nanowires. A four-point connection (Figure 4-9a) was configured to test the piezoresistance in nanowires with Ohmic contacts. The strain was applied to the nanowire by bending the substrate, as illustrated in Figure 4-9b. Because the nanowire stays on the surface of the substrate and its dimension is much smaller than the substrate, it mainly experiences tensile strain with minimal shear strain when the device is deflected down. Similarly, it mainly experiences compressive strain when the device is deflected up. Relationship between the strain and the substrate deflection was determined by both classical beam theory and finite element analysis. Since the strain, current density, and electric field are all along the c-axis of the

ZnO nanowire, this setup characterizes the longitudinal piezoresistive effect [132], which is the most relevant for piezotronic devices based on lateral nanowires.

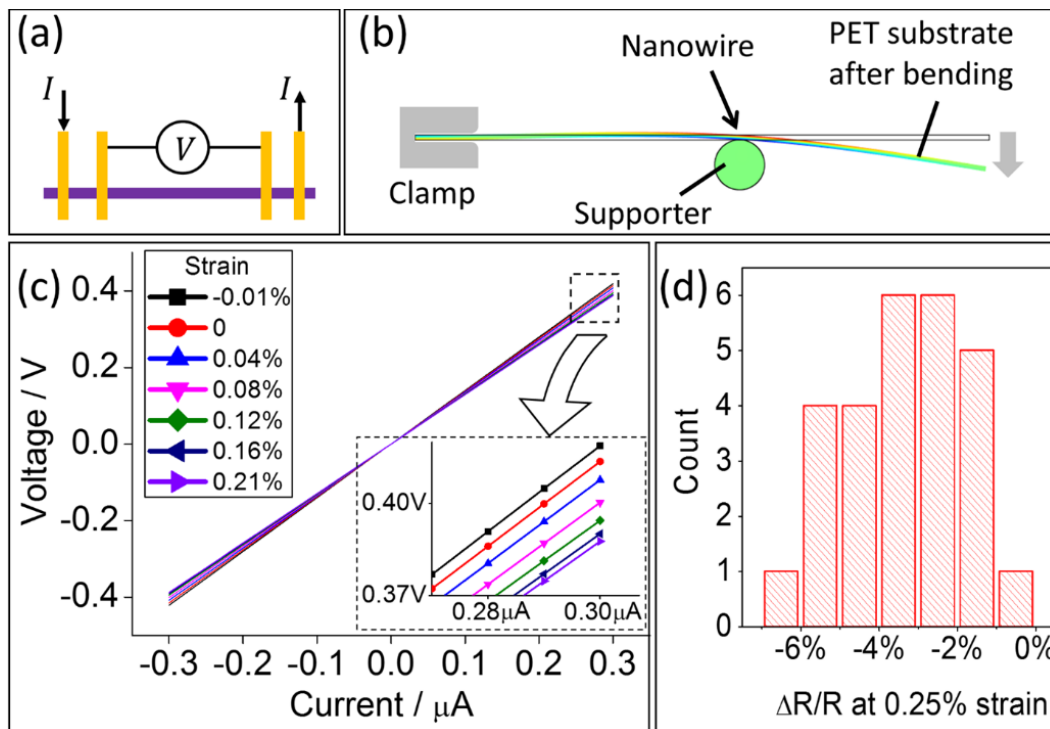


Figure 4-9. Measurement of the piezoresistive effect in devices with Ohmic contacts. (a) Schematic diagram of the four-point measurement. (b) Schematic diagram of the experimental setup used to stretch the ZnO nanowire; the polymer substrate is deflected by a programmable linear motor. (c) Voltage-current curves of a nanowire under different strains, obtained with the four-point configuration in (a); the inset is a zoom-in view of the curves at the high current end. (d) Histogram of the relative change of resistance, measured from 27 nanowire segments under tensile strain.

Figure 4-9c shows typical voltage-current (V-I) curves from the four-point measurement. The resistance decreases when the nanowire is stretched, and increases when

it is compressed. The histogram in Figure 4-9d represents the relative change of resistance under 0.25% tensile strain among 27 nanowires. All the nanowires have lower resistance under the tensile strain, with the $\Delta R/R$ value between -0.3% and -6.8%.

The change of volume resistance under strain can be derived:

$$\begin{aligned} \therefore R &= \frac{\rho L}{A} = \frac{\rho L}{\pi r^2} \\ \therefore \frac{\Delta R}{R} &\approx \frac{dR}{R} = \frac{d\rho}{\rho} + \frac{dL}{L} - 2\frac{dr}{r}, \\ \therefore \frac{dL}{L} &= \varepsilon, \frac{dr}{r} = -\nu \\ \therefore \frac{\Delta R}{R} &\approx \frac{d\rho}{\rho} + \varepsilon(1 + 2\nu) \end{aligned}$$

where ρ is the resistivity, L is the length of the nanowire, A is the cross section area, r is the radius, ε is the strain, and ν is the Poisson's ratio. In the expression, $\varepsilon(1 + 2\nu)$ is the geometric term, and for ZnO nanowire at 0.25% strain, it equals to 0.4%. Therefore, the piezoresistive term, $d\rho/\rho$, is approximately between -0.7% and -7.2% in those nanowires. For the first time we show that the c-orientated n-type ZnO nanowire has a negative longitudinal piezoresistive coefficient, and in most cases the piezoresistive effect is more significant than the geometric change.

Two factors may cause the variance of the $\Delta R/R$ value among nanowires. First, piezoresistance depends on semiconductor parameters such as the carrier concentration [133]. Based on the resistance and geometry of those ZnO nanowires, we found that the resistivity can be more than an order of magnitude different, suggesting great variance in

the carrier density among nanowires. Second, the 0.25% strain is the strain on the surface of the flexible substrate. The actual strain in the nanowire depends on its diameter (discussed later) and also the adhesion between the SU-8 and the nanowire, and thus can deviate to different extents from the 0.25% value. We believe the wide range of $d\rho/\rho$ between -0.7% and -7.2% is mainly from the first factor, because some thick nanowires also had a great change in resistivity although they are more difficult to strain than thinner nanowires.

4.6. Isolation of the piezotronic effect

Variation of the four-point measurement, as illustrated in Figure 4-10a, can introduce the contact 1 and contact 2 in addition to the nanowire resistance. At a certain current, subtracting V_a from V_b gives the potential difference across contact 1 (ΔV_1). Similarly, subtracting V_a from V_c reveals the potential difference across contact 2 (ΔV_2). When the Ti/ZnO contact has a barrier, the change of ΔV_1 and ΔV_2 under strain represents the piezotronic effect. Therefore, measurements in Figure 4-10a can separate the piezotronic and piezoresistive effects.

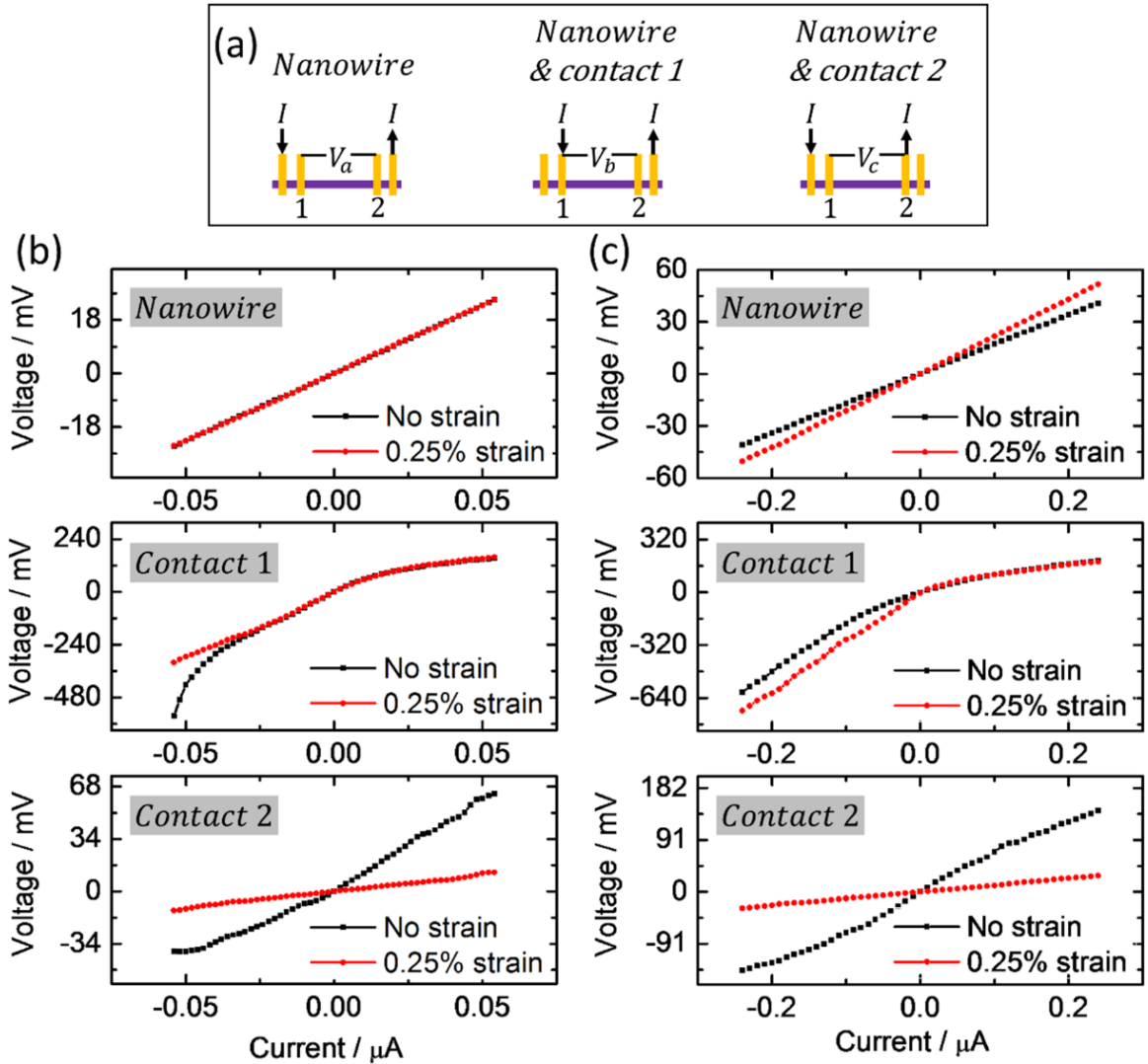


Figure 4-10. Comparison of the piezotronic effect and the piezoresistive effect in devices with barrier contacts. (a) Schematic diagram of three different connections to extract the nanowire resistance and two contacts. (b) Voltage-current (V-I) measurement of a typical device; the V-I curve of nanowire resistance is directly obtained, while the V-I curves of contact 1 and contact 2 are derived by subtracting V_a from V_b and V_c in (a). (c) Voltage-

current curves of another device obtained with the similar methods; the measured nanowire resistance increases under the tensile strain.

Figure 4-10b compares the V-I curves of nanowire resistance, contact 1, and contact 2 in a nanowire with barrier contacts. The curves of contact 1 and contact 2 are obtained after the subtraction of V_a from V_b and V_c in Figure 4-10a. Under the same current, much higher voltage across contact 1 and contact 2 than that across the nanowire indicates that the interfacial barriers are more significant than the nanowire resistance. More importantly, V-I curves of the two contacts have prominent change under 0.25% tensile strain while the change of nanowire resistance is negligible. For instance, under a fixed bias, the current flowing through contact 2 increases almost five-fold. Thus the piezotronic effect at the contacts is much greater than the piezoresistive effect in the nanowire, which supports directly the assumption made in previous studies [26].

Moreover, decoupling the piezotronic effects at the two contacts enables us to extract detailed information at the individual contact. Figure 4-10b shows that contact 1 behaves as a rectifying barrier under zero strain, and the tensile strain lowers the barrier and increases the reverse current. Contact 2 has a lower barrier height than contact 1 and is close to an Ohmic contact, suggesting that the tunneling may dominate the current transport [134]. The strain further reduces the barrier height. In terms of strain sensing, contact 2 has higher sensitivity than contact 1. Such distinctive transport characteristics of contact 1 and contact 2, when lumped in a two-terminal device, complicates the analysis and makes it challenging to predict the device behavior. In fact, most ZnO piezotronic

devices in the literature formed different electric contacts at two ends even with the same metal, so it is necessary to analyze the two contacts independently.

Figure 4-10c shows the V-I curves of another multi-terminal device. While the piezotronic effect still dominates, this nanowire has an unusual piezoresistive effect. The tensile strain increases nanowire resistance with $\Delta R/R$ as high as 23%. The positive piezoresistive coefficient opposes the result in Figure 4-9d where all the nanowires with Ohmic contacts have a negative piezoresistive coefficient. Such a phenomenon has been observed in several devices with barrier contacts, and here we propose a possible explanation. Although the four-point measurement excludes the contact resistance, the effect of contacts can extend *into* the thin nanowire. Numerical calculation shows that when ZnO nanowire forms Schottky contacts with electrodes, the region near the contact has a lower carrier density than the rest part of the nanowire (depletion region). Strain-induced polarization charge at the contact further changes the carrier distribution [36]. Therefore, a strain could alter the carrier profile within the nanowire, which in turn affects the volume resistance. The measured piezoresistive effect depends on the contacts, and it may be more properly called an “apparent” piezoresistive effect.

4.7. Finite element analysis of embedded nanowires

In the literature, a vast majority of the devices have the electrodes on two ends of the nanowires, and there is a good reason for doing that. The piezotronic effect is caused by the polarization charge [36, 118]. When a ZnO nanowire is under uniform tensile/compressive strain, the charge only appears at the two ends.

However for the multi-terminal piezotronic device here, electrodes are on the side surface of the nanowire. The observed piezotronic effect with the electrodes on the side surface is ascribed to the non-uniform strain along the nanowire. COMSOL Multiphysics was used to simulate the elastic and piezoelectric behavior of a ZnO nanowire embedded in a polymer matrix. In real devices the nanowire is encapsulated in SU-8; here the polymer is defined as PET, whose mechanical properties are comparable to those of SU-8. For simplicity, two assumptions were made. First, both the polymer and the nanowire behave elastically. And second, there is no slippage between the nanowire and the polymer. The material properties used for the simulation are in Table 4-2.

Material	Young's Modulus / GPa	Poisson's Ratio
ZnO nanowire (from [135])	129.0	0.349
PET (from COMSOL database)	2.8	0.4

Table 4-2. Mechanical properties of ZnO and polymer used in the finite element analysis.

In the model, two ends of the polymer are subject to uniform tensile loads, as shown in Figure 4-11a, and the strain is transferred from the polymer to the nanowire. Figure 4-11b shows the normal strain along the central axis of nanowires with different diameters but the same length of 50 μm . The strain near the two ends of the nanowire is much lower than that in the polymer far away from the nanowire (indicated by the dashed line). As the diameter becomes larger, the average strain in the nanowire is lower. The strain distribution results from the different elastic moduli of ZnO and polymer. The strain distribution can also be calculated by the Shear Lag Analysis in the composite mechanics [136].

Figure 4-11c shows the electrical polarization along the central axis of the nanowires, which has the similar characteristics as the normal strain. By calculating the divergence of the polarization field, we found that the polarization charge density is the highest at the two ends, but non-zero on the side surface. Positive charge appears near the (0001) end of the nanowire, and the charge density decays further away from the end surface. The (000 $\bar{1}$) end has a similar distribution of negative charge.

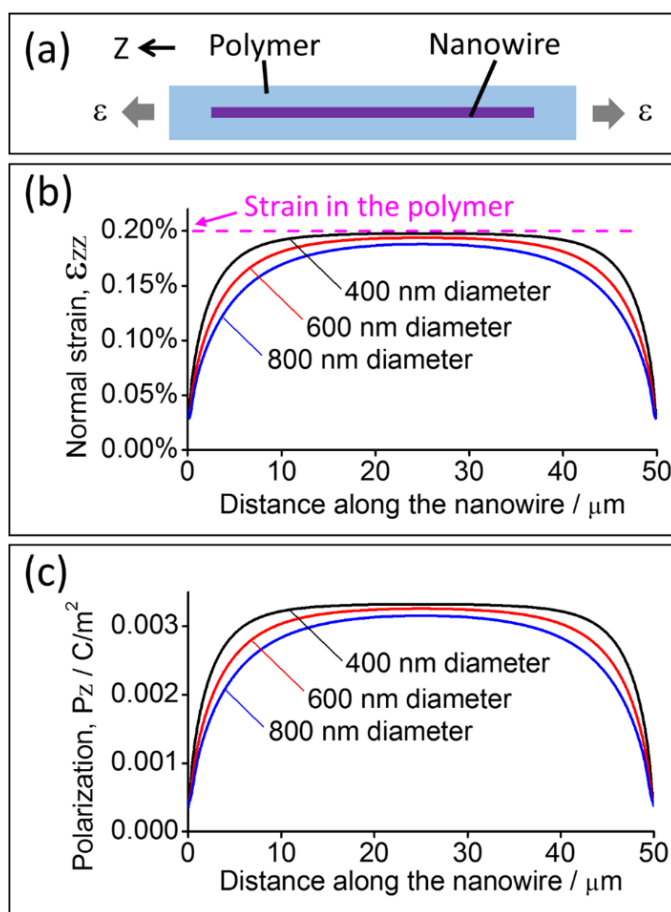


Figure 4-11. Simulation of the non-uniform strain in ZnO nanowires. (a) Schematic diagram of a nanowire embedded in a polymer matrix. (b) Normal strain along the central axis of nanowires with the same length but different diameters; the dashed line indicates

the normal strain in the polymer far away from the nanowire. (c) Electrical polarization along the central axis of nanowires with the same length but different diameters.

The charge distribution from the ends to the middle of the nanowire can produce a rich variety of piezotronic effects, depending on the positions of the electrodes. When the charges near the two electrodes have the same polarity, piezotronic effects raise or reduce the barrier height of both electrodes, e.g. the device in Figure 4-10b. If the charges have different polarities, the piezotronic effects are opposite at the two contacts, such as the device in Figure 4-10c. When the electrodes are in the region where the polarization charge is negligible and the change of the barrier height is insignificant, the device will not show significant piezotronic effects. If the strain distribution can be under good control, it is not only feasible but also beneficial to put contacts on the side surface of a nanowire, in order to have multiple piezotronic effects with desired properties.

4.8. Discussion and future work

(1) Selection of the fabrication process for electrodes on ZnO nanowires

In general there are two approaches to fabricate metal electrodes. In the first one, photoresist is coated on the metal layer and patterned by photolithography; then exposed part of the metal is etched for the pattern transfer. In the second method, metal is deposited onto patterned photoresist; then the photoresist is stripped in a solvent to remove unwanted metal, called a liftoff process. As an amphoteric oxide, ZnO is readily dissolved in many acids and bases, and it is difficult to find a chemical that can etch metal without attacking ZnO. Therefore, liftoff is chosen for the electrodes patterning.

As shown in Figure 4-12, a critical step of the liftoff is to form undercut on the photoresist. Without undercut, deposited metal will be a continuous layer and difficult to break. Many techniques can produce the undercut, and when selecting a proper liftoff process, we must consider its effect on the material property, previous fabrication steps, and next fabrication steps. In this study, three different liftoff technologies have been evaluated. The first one is *Image Reversal Process*, in which the polarity of a positive-tone photoresist is reversed after a soak in ammonia gas to produce an undercut profile; because ammonia significantly affects the electrical property of ZnO [137], this method cannot be used. The second one is *Bilayer Process* and involves spinning of two different resists onto the substrate; however, the bake temperature of the resists is higher than 150 °C, which is far above the glass transition temperature of the PET substrate and causes it to deform. The third option is based on a negative-tone photoresist; the chemicals used in the process do not directly react with ZnO, and the bake temperature can be as low as 130 °C. Therefore, the third one was selected for the device fabrication.

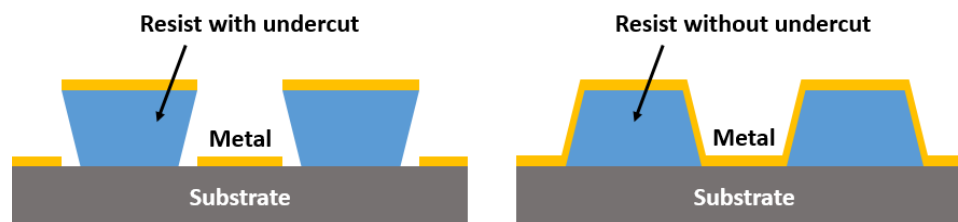


Figure 4-12. A photoresist with undercut is desired for metal liftoff.

(2) Schottky contact on ZnO nanowires

The piezotronic effect only works with Schottky barriers. ZnO crystals almost always have unintentional n-type conductivity. To form Schottky contact with n-type

semiconductors, high work function metals should be adopted as electrodes. Gold has a work function larger than 5. However, most gold contacts were Ohmic on the ZnO nanowires. Titanium has a much lower work function than gold, but could still have formed Schottky contacts in some devices. Overall, among several hundreds of devices that have been fabricated in this study, less than 20% of the contacts are Schottky.

Prevalence of the Ohmic contact may be due to the high carrier density in the nanowires. As the nanowire forms Schottky barrier with gold, a high carrier concentration leads to a thin depletion layer. If the depletion width is too small, carriers can tunnel through the depletion layer, and the contact becomes Ohmic essentially [134].

Free carriers in the ZnO nanowire are introduced by intrinsic defects and impurities [138], and can also come from adsorption of chemical species on its surface. Since nanostructure has a large surface-to-volume ratio, adsorption could change its electrical property significantly. Reducing agents in the environment, such as H₂S [139] and ethanol [140], inject electrons into ZnO nanowire and increase its carrier density. For example, H₂S reacts with the chemisorbed oxygen on the ZnO surface, causing the electrons in the oxygen ions to flow back into ZnO:



Water, which is frequently used in the fabrication process, can increase the carrier density of ZnO as well. Water molecules are physically adsorbed on the nanowire surface. Dipoles of the water molecules will line up and neutralize the surface electric field, rendering the electron on O₂⁻ in an unfavorable energy state. Some oxygen ions release

electrons back into the conduction band of ZnO and increase the carrier concentration [141].

In order to promote the Schottky contact, the carrier density should be reduced by eliminating the defect sites and oxidizing the surface. Common methods include annealing at an elevated temperature in air and exposure to intense oxygen plasma [142]. Unfortunately, they will damage the SU-8 lifting layer, the PET substrate, and the photoresist. Figure 4-13 below shows the damage caused on the polymer by only 3 min of moderate oxygen plasma treatment. An effective treatment to reduce the carrier density typically requires at least ten minutes. Therefore, a treatment method that does not attack the polymer needs to be developed. For example, hydrogen peroxide has been demonstrated to promote the Schottky contact on ZnO nanowires [143], and it may not damage the polymer as aggressively as annealing or oxygen plasma.

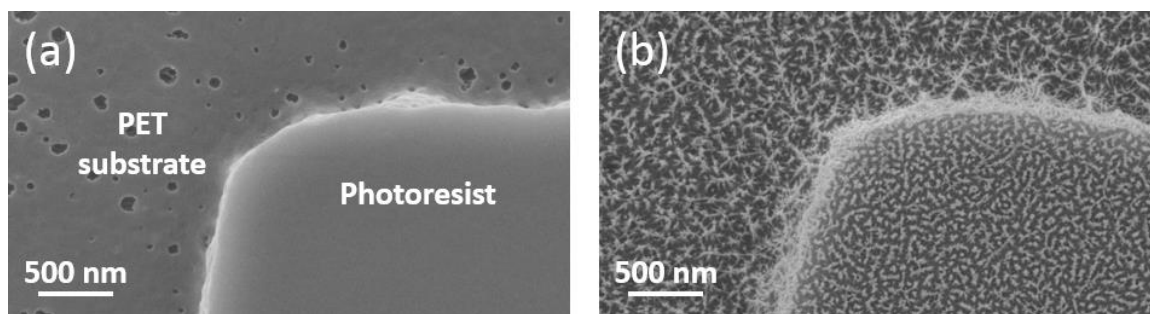


Figure 4-13. Damage on polymer caused by oxygen plasma. (a) SEM image of PET substrate and photoresist before oxygen plasma treatment. (b) After 3 min of oxygen plasma treatment.

(3) Strain transfer from the polymer to the nanowire

In the device strain is transferred from the polymer matrix to the embedded nanowire. By assuming that there is no yielding or slippage, the strain on the nanowire can be simulated and estimated. However, if the assumption is not true, there could be a large discrepancy between the estimated strain and the real one. Figure 4-14 shows the simulation of normal strain distribution both along the nanowire and in the adjacent polymer. At the interface between the nanowire and the polymer, the strain on the polymer side is greatly amplified. It is possible that the polymer will have plastic deformation or even become separated from the nanowire.

Such a device structure is not suitable for more quantitatively analysis or real application in precise strain sensing, because it is difficult to know the actual strain on the nanowire. In order to accurately define the strain, the nanowire needs to be bonded to a substrate with a comparable elastic modulus. Alternative, as shown in Figure 1-4c of Chapter 1, the nanowire may work in the bending mode to take advantage of its small bending stiffness.

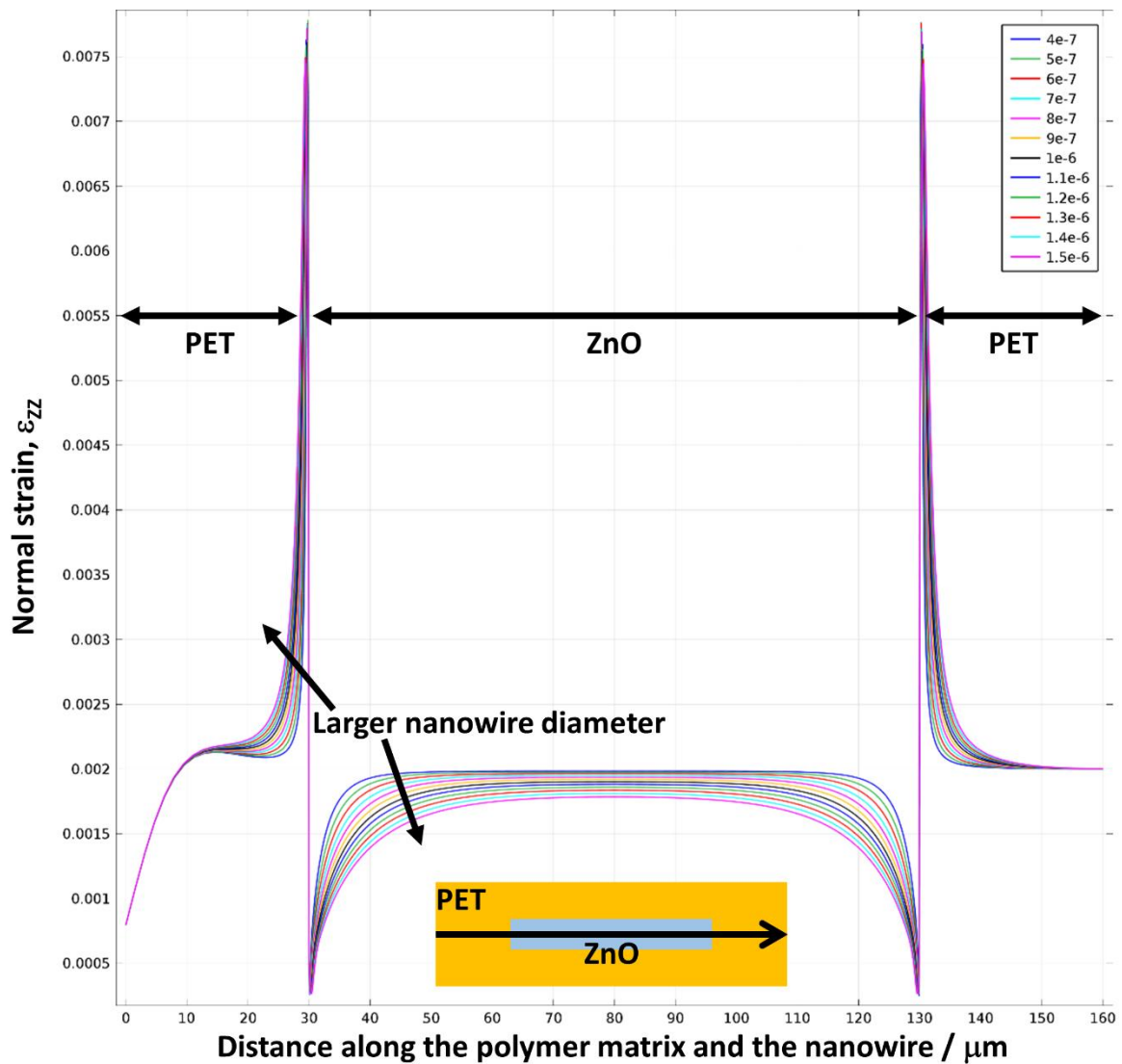


Figure 4-14. Normal strain along the central axis of the polymer matrix and the embedded nanowire. Different curves represent nanowires with the same length but different diameters.

CHAPTER 5. CONCLUSION

Piezoelectric nanostructures have promising applications in mechanical energy harvesting and strain sensing thanks to their reduced dimension, enhanced flexibility, and single crystallinity. However, their extremely small size prevent us from controlling and studying them by conventional approaches used for bulk materials. In this thesis, several practical problems that are unique to the piezoelectric nanostructures have been discussed, and novel methods have been developed to address those issues.

Well-aligned and orientation-defined growth of ZnO nanowires has been achieved on an inexpensive textured film. The textured film prepared through a hydrothermal process is comparable to expensive single crystals in initiating epitaxial growth of ZnO nanowires. Nanowires on textured film have good alignment even at low growth density. Vertical, tilted, and lateral ZnO nanowire arrays have been achieved on silicon substrate. The textured film is more than a low-cost alternative to single crystal substrate. The low-temperature hydrothermal process and the conventional photolithography technique allow hierarchical nanostructures to be synthesized, and mini-sea-urchins with radial ZnO nanowire arrays have been demonstrated. The growth method is expected to be applicable to other materials and inspire versatile growth method for novel nanostructure. Well-aligned and oriented nanowire array from this study will facilitate the design and fabrication of energy harvesters and strain sensors that can respond to mechanical stimuli from different directions.

For the alignment of piezoelectric nanostructures, the Spinning-Langmuir-Film technique developed in this thesis combines several advantages: (1) the setup is simple, low-cost, and feasible for scale-up; (2) the areal density of aligned nanostructures can be controlled in a wide range; (3) the aligned nanostructures can be transferred onto receiving substrates and form good electric interface with other materials. Alignment of zinc oxide nanorods and diphenylalanine peptide nanotubes on silicon substrate with different areal density have been demonstrated. A time-dependent study reveals the alignment history, and it turns out that the alignment develops radially in a speed of several millimeters per second. The surfactant is critical to the success of this technique, and its applying and removing are discussed in details. Finally, this general method can potentially be applied to ferroelectric nanostructures and flexible substrates for the fabrication of energy harvesters.

The last task of this thesis is to independently study the piezotronic effect and the piezoresistive effect in a ZnO nanowire. Fabrication of multiple electrodes on a nanowire that will be subject to large strain is challenging. A novel lifting-layer process and careful selection of the liftoff process greatly improve the device fabrication yield. With a four-point connection, the piezoresistive effect in ZnO nanowires has been extracted for the first time, and tensile strain is found to reduce the resistivity. However, a barrier contact could influence the apparent piezoresistive effect even with the four-point connection. Modified four-point measurements revealed the piezotronic effect at a barrier contact, which proves to be more significant than the piezoresistive effect. In addition, the feasibility and

advantage of using piezotronic effects on the side surface of nanowires has been discussed. The general methods developed in this work contribute to the fundamental understanding of the piezotronic effect.

In spite of the progress, the real application of piezoelectric nanostructures in energy harvesting and strain sensing still requires a lot of research effort on the material science. For example, the selectivity of the synthesis process needs improvement by upgrading the CVD system. Ferroelectric nanostructures must be synthesized to take advantage of the alignment technique for the energy harvesting purpose. And developing a more reliable and reproducible way to form Schottky contacts on ZnO nanowires is a priority in the research on piezotronic devices. Moreover, advances in various research fields outside the material science are needed - development of low power consumption nano systems, fabrication of electrodes around the nanowires, packaging of the device for biological environment, etc. Both challenges and opportunities exist in this emerging field.

REFERENCES

- [1] R. Wojnar, Piezoelectric Phenomena in Biological Tissues, in: G. Ciofani, A. Menciassi (Eds.) Piezoelectric Nanomaterials for Biomedical Applications, Springer Berlin Heidelberg, 2012, pp. 173-185.
- [2] K. Uchino, Ferroelectric Devices 2nd Edition, CRC press, 2009.
- [3] M.H. Huang, Y. Wu, H. Feick, N. Tran, E. Weber, P. Yang, Adv. Mater., 13 (2001) 113-116.
- [4] D. Xu, Y. Xu, D. Chen, G. Guo, L. Gui, Y. Tang, Adv. Mater., 12 (2000) 520-522.
- [5] Y. Wang, L. Zhang, C. Liang, G. Wang, X. Peng, Chem. Phys. Lett., 357 (2002) 314-318.
- [6] X. Duan, C.M. Lieber, J. Am. Chem. Soc., 122 (2000) 188-189.
- [7] S.W. Choi, S.M. Jo, W.S. Lee, Y.R. Kim, Adv. Mater., 15 (2003) 2027-2032.
- [8] M. Reches, E. Gazit, Nat. Nanotechnol., 1 (2006) 195-200.
- [9] G. Xu, Z. Ren, P. Du, W. Weng, G. Shen, G. Han, Adv. Mater., 17 (2005) 907-910.
- [10] W.S. Yun, J.J. Urban, Q. Gu, H. Park, Nano Lett., 2 (2002) 447-450.
- [11] H. Shi, X. Li, D. Wang, Y. Yuan, Z. Zou, J. Ye, Catal. Lett., 132 (2009) 205-212.
- [12] B. Mayers, Y. Xia, J. Mater. Chem., 12 (2002) 1875-1881.
- [13] S. Xu, Y. Wei, M. Kirkham, J. Liu, W. Mai, D. Davidovic, R.L. Snyder, Z.L. Wang, J. Am. Chem. Soc., 130 (2008) 14958-14959.
- [14] A. Koka, H.A. Sodano, Nat. Commun., 4 (2013).
- [15] J. Zhou, P. Fei, Y. Gao, Y. Gu, J. Liu, G. Bao, Z.L. Wang, Nano Lett., 8 (2008) 2725-2730.
- [16] D.-H. Kim, R. Ghaffari, N. Lu, J.A. Rogers, Annu. Rev. Biomed. Eng., 14 (2012) 113-128.

- [17] R. Agrawal, B. Peng, H.D. Espinosa, *Nano Lett.*, 9 (2009) 4177-4183.
- [18] Z. Gao, Y. Ding, S. Lin, Y. Hao, Z.L. Wang, *Phys. Status Solidi RRL*, 3 (2009) 260-262.
- [19] Y. Motola, L. Banks-Sills, V. Fourman, *Strain*, 45 (2009) 85-92.
- [20] Z.L. Wang, J. Song, *Science*, 312 (2006) 242.
- [21] X. Wang, J. Zhou, J. Song, J. Liu, N. Xu, Z.L. Wang, *Nano Lett.*, 6 (2006) 2768-2772.
- [22] Y. Hu, Y. Gao, S. Singamaneni, V.V. Tsukruk, Z.L. Wang, *Nano Lett.*, 9 (2009) 2661-2665.
- [23] J. Pu, X. Yan, Y. Jiang, C. Chang, L. Lin, *Sensors & Actuators A: Physical*, 164 (2010) 131-136.
- [24] R. Zhu, W. Zhang, R. Yang, *Science of Advanced Materials*, 4 (2012) 798-804.
- [25] X. Wang, *Nano Energy*, 1 (2012) 13-24.
- [26] W. Wu, C. Pan, Y. Zhang, X. Wen, Z.L. Wang, *Nano Today*, 8 (2013) 619-642.
- [27] J.A. Paradiso, T. Starner, *IEEE Pervas. Comput.*, 4 (2005) 18-27.
- [28] N.S. Hudak, G.G. Amatucci, *J. Appl. Phys.*, 103 (2008) 101301-101324.
- [29] R. Yang, Y. Qin, L. Dai, Z.L. Wang, *Nat. Nanotechnol.*, 4 (2008) 34-39.
- [30] G. Zhu, R. Yang, S. Wang, Z.L. Wang, *Nano Lett.*, 10 (2010) 3151-3155.
- [31] Y. Hu, Y. Zhang, C. Xu, G. Zhu, Z.L. Wang, *Nano Lett.*, 10 (2010) 5025-5031.
- [32] J.H. Jung, M. Lee, J.-I. Hong, Y. Ding, C.-Y. Chen, L.-J. Chou, Z.L. Wang, *ACS Nano*, 5 (2011) 10041-10046.
- [33] T.I. Lee, S. Lee, E. Lee, S. Sohn, Y. Lee, S. Lee, G. Moon, D. Kim, Y.S. Kim, J.M. Myoung, Z.L. Wang, *Adv. Mater.*, 25 (2013) 2920-2925.
- [34] X. Wang, *Piezoelectric and Piezotronic Effects in Energy Harvesting and Conversion*, in: *Nanotechnology for the Energy Challenge*, Wiley-VCH Verlag GmbH & Co. KGaA, 2013, pp. 89-132.

- [35] J. Zhou, Y. Gu, P. Fei, W. Mai, Y. Gao, R. Yang, G. Bao, Z.L. Wang, *Nano Lett.*, 8 (2008) 3035-3040.
- [36] Y. Zhang, Y. Liu, Z.L. Wang, *Adv. Mater.*, 23 (2011) 3004-3013.
- [37] X. Wen, W. Wu, Y. Ding, Z.L. Wang, *Adv. Mater.*, 25 (2013) 3371-3379.
- [38] Z.L. Wang, *Nano Today*, 5 (2010) 540-552.
- [39] K.-I. Park, S. Xu, Y. Liu, G.-T. Hwang, S.-J.L. Kang, Z.L. Wang, K.J. Lee, *Nano Lett.*, 10 (2010) 4939-4943.
- [40] W.I. Park, G.C. Yi, *Adv. Mater.*, 16 (2004) 87-90.
- [41] M.H. Huang, S. Mao, H. Feick, H. Yan, Y. Wu, H. Kind, E. Weber, R. Russo, P. Yang, *Science*, 292 (2001) 1897-1899.
- [42] H.T. Ng, B. Chen, J. Li, J. Han, M. Meyyappan, J. Wu, S.X. Li, E.E. Haller, *Appl. Phys. Lett.*, 82 (2003) 2023-2025.
- [43] J. Zúñiga-Pérez, A. Rahm, C. Czekalla, J. Lenzner, M. Lorenz, M. Grundmann, *Nanotechnology*, 18 (2007) 195303.
- [44] S. Xu, Y. Ding, Y. Wei, H. Fang, Y. Shen, A.K. Sood, D.L. Polla, Z.L. Wang, *J. Am. Chem. Soc.*, 131 (2009) 6670-6671.
- [45] P.J. Pauzauskie, A. Radenovic, E. Trepagnier, H. Shroff, P. Yang, J. Liphardt, *Nat. Mater.*, 5 (2006) 97-101.
- [46] I.M. Daniel, O. Ishai, *Engineering Mechanics of Composite Materials*, Oxford University Press, New York, 2006.
- [47] R. Zhu, W. Zhang, C. Li, R. Yang, *Nano Lett.*, 13 (2013) 5171-5176.
- [48] R. Zhu, Y. Lai, V. Nguyen, R. Yang, *Nanoscale*, 6 (2014) 11976-11980.
- [49] R. Zhu, R. Yang, *Nanotechnology*, 25 (2014) 345702.
- [50] Z.L. Wang, *J. Phys.: Condens. Matter*, 16 (2004) R829.
- [51] Y. Wang, G. Meng, L. Zhang, C. Liang, J. Zhang, *Chem. Mater.*, 14 (2002) 1773-1777.

- [52] C.C. Chen, C.C. Yeh, *Adv. Mater.*, 12 (2000) 738-741.
- [53] L.E. Greene, M. Law, D.H. Tan, M. Montano, J. Goldberger, G. Somorjai, P. Yang, *Nano Lett.*, 5 (2005) 1231-1236.
- [54] Y. Tak, S.J. Hong, J.S. Lee, K. Yong, *J. Mater. Chem.*, 19 (2009) 5945-5951.
- [55] S.Y. Li, P. Lin, C.Y. Lee, T.Y. Tseng, *J. Appl. Phys.*, 95 (2004) 3711-3716.
- [56] X.D. Wang, J. Zhou, C.S. Lao, J.H. Song, N.S. Xu, Z.L. Wang, *Adv. Mater.*, 19 (2007) 1627-1631.
- [57] Y. Qin, R. Yang, Z.L. Wang, *J. Phys. Chem. C*, 112 (2008) 18734-18736.
- [58] J.J.F. Conley, L. Stecker, Y. Ono, *Appl. Phys. Lett.*, 87 (2005) 223114-223113.
- [59] B. Nikoobakht, C.A. Michaels, S.J. Stranick, M.D. Vaudin, *Appl. Phys. Lett.*, 85 (2004) 3244-3246.
- [60] J.B.K. Law, J.T.L. Thong, *Nanotechnology*, 18 (2007) 055601.
- [61] S. Xu, Z. Wang, *Nano Res.*, 4 (2011) 1013-1098.
- [62] W.I. Park, D.H. Kim, S.W. Jung, G.-C. Yi, *Appl. Phys. Lett.*, 80 (2002) 4232-4234.
- [63] Y. Sun, G.M. Fuge, M.N.R. Ashfold, *Chem. Phys. Lett.*, 396 (2004) 21-26.
- [64] H.Z. Zhang, X.C. Sun, R.M. Wang, D.P. Yu, *J. Cryst. Growth*, 269 (2004) 464-471.
- [65] C. Li, G. Fang, Q. Fu, F. Su, G. Li, X. Wu, X. Zhao, *J. Cryst. Growth*, 292 (2006) 19-25.
- [66] J. Song, S. Lim, *The Journal of Physical Chemistry C*, 111 (2006) 596-600.
- [67] D. Byrne, R. Fath Allah, T. Ben, D. Gonzalez Robledo, B. Twamley, M.O. Henry, E. McGlynn, *Cryst. Growth Des.*, 11 (2011) 5378-5386.
- [68] D.-S. Kang, S.K. Han, J.-H. Kim, S.M. Yang, J.G. Kim, S.-K. Hong, D. Kim, H. Kim, J.-H. Song, *Journal of Vacuum Science and Technology B*, 27 (2009) 1667-1672.
- [69] Y. Wei, W. Wu, R. Guo, D. Yuan, S. Das, Z.L. Wang, *Nano Lett.*, 10 (2010) 3414-3419.

- [70] S. Xu, C. Lao, B. Weintraub, Z.L. Wang, *J. Mater. Res.*, 23 (2008) 2072-2077.
- [71] Q. Li, J.R. Creighton, G.T. Wang, *J. Cryst. Growth*, 310 (2008) 3706-3709.
- [72] T.-J. Kuo, C.-N. Lin, C.-L. Kuo, M.H. Huang, *Chem. Mater.*, 19 (2007) 5143-5147.
- [73] G. Zhu, Y. Zhou, S. Wang, R. Yang, Y. Ding, X. Wang, Y. Bando, Z.L. Wang, *Nanotechnology*, 23 (2012) 055604.
- [74] H. Jansen, M.d. Boer, R. Legtenberg, M. Elwenspoek, *Journal of Micromechanics and Microengineering*, 5 (1995) 115.
- [75] H.T. Ng, J. Han, T. Yamada, P. Nguyen, Y.P. Chen, M. Meyyappan, *Nano Lett.*, 4 (2004) 1247-1252.
- [76] D. Tsivion, M. Schwartzman, R. Popovitz-Biro, E. Joselevich, *ACS Nano*, 6 (2012) 6433-6445.
- [77] A.d. Campo, C. Greiner, *Journal of Micromechanics and Microengineering*, 17 (2007) R81.
- [78] S.H. Dalal, D.L. Baptista, K.B.K. Teo, R.G. Lacerda, D.A. Jefferson, W.I. Milne, *Nanotechnology*, 17 (2006) 4811.
- [79] P. Yang, H. Yan, S. Mao, R. Russo, J. Johnson, R. Saykally, N. Morris, J. Pham, R. He, H.J. Choi, *Adv. Funct. Mater.*, 12 (2002) 323-331.
- [80] S.D. Hersee, X. Sun, X. Wang, *Nano Lett.*, 6 (2006) 1808-1811.
- [81] E.M. Freer, O. Grachev, X. Duan, S. Martin, D.P. Stumbo, *Nat. Nanotechnol.*, 5 (2010) 525-530.
- [82] E.T. Thostenson, T.-W. Chou, *J. Phys. D: Appl. Phys.*, 35 (2002) L77.
- [83] H. Huang, C. Liu, Y. Wu, S. Fan, *Adv. Mater.*, 17 (2005) 1652-1656.
- [84] F. Du, J.E. Fischer, K.I. Winey, *Phys. Rev. B: Condens. Matter Mater. Phys.*, 72 (2005) 121404.
- [85] P.A. Smith, C.D. Nordquist, T.N. Jackson, T.S. Mayer, B.R. Martin, J. Mbindyo, T.E. Mallouk, *Appl. Phys. Lett.*, 77 (2000) 1399-1401.

- [86] L. Dong, J. Bush, V. Chirayos, R. Solanki, J. Jiao, Y. Ono, J.F. Conley, B.D. Ulrich, *Nano Lett.*, 5 (2005) 2112-2115.
- [87] M. Tanase, D.M. Silevitch, A. Hultgren, L.A. Bauer, P.C. Searson, G.J. Meyer, D.H. Reich, *J. Appl. Phys.*, 91 (2002) 8549.
- [88] C.M. Hangarter, N.V. Myung, *Chem. Mater.*, 17 (2005) 1320-1324.
- [89] Z. Fan, J.C. Ho, Z.A. Jacobson, R. Yerushalmi, R.L. Alley, H. Razavi, A. Javey, *Nano Lett.*, 8 (2007) 20-25.
- [90] J. Yao, H. Yan, C.M. Lieber, *Nat. Nanotechnol.*, 8 (2013) 329-335.
- [91] M.C. LeMieux, M. Roberts, S. Barman, Y.W. Jin, J.M. Kim, Z. Bao, *Science*, 321 (2008) 101-104.
- [92] J.P. Opatkiewicz, M.C. LeMieux, Z. Bao, *ACS Nano*, 4 (2010) 1167-1177.
- [93] F. Kim, S. Kwan, J. Akana, P. Yang, *J. Am. Chem. Soc.*, 123 (2001) 4360-4361.
- [94] A. Tao, F. Kim, C. Hess, J. Goldberger, R. He, Y. Sun, Y. Xia, P. Yang, *Nano Lett.*, 3 (2003) 1229-1233.
- [95] Y. Huang, X. Duan, Q. Wei, C.M. Lieber, *Science*, 291 (2001) 630-633.
- [96] J. Huang, R. Fan, S. Connor, P. Yang, *Angew. Chem. Int. Ed.*, 46 (2007) 2414-2417.
- [97] G. Yu, A. Cao, C.M. Lieber, *Nat. Nanotechnol.*, 2 (2007) 372-377.
- [98] M. Liu, Y. Chen, Q. Guo, R. Li, X. Sun, J. Yang, *Nanotechnology*, 22 (2011) 125302.
- [99] J.T. Petkov, K.D. Danov, N.D. Denkov, R. Aust, F. Durst, *Langmuir*, 12 (1996) 2650-2653.
- [100] C. Mingotaud, B. Agricole, C. Jégo, *J. Phys. Chem.*, 99 (1995) 17068-17070.
- [101] B.M. Abraham, K. Miyano, S.Q. Xu, J.B. Ketterson, *Rev. Sci. Instrum.*, 54 (1983) 213-219.
- [102] R. Zhu, Z. Lu, Y. Wei, *Thin Solid Films*, 284-285 (1996) 43-45.
- [103] G. Agarwal, R.S. Phadke, *Thin Solid Films*, 327-329 (1998) 9-13.

- [104] G.D. Moon, T.I. Lee, B. Kim, G. Chae, J. Kim, S. Kim, J.-M. Myoung, U. Jeong, *ACS Nano*, 5 (2011) 8600-8612.
- [105] M.E.R. Shanahan, *Langmuir*, 11 (1995) 1041-1043.
- [106] R.E. Johnson, R.H. Dettre, Contact Angle Hysteresis, in: F.M. Fowkes (Ed.) *Contact Angle, Wettability, and Adhesion*, American Chemical Society, Washington, DC, USA, 1964, pp. 112-135.
- [107] R.E. Johnson, R.H. Dettre, *J. Phys. Chem.*, 68 (1964) 1744-1750.
- [108] T. Krupenkin, S. Yang, P. Mach, *Appl. Phys. Lett.*, 82 (2003) 316-318.
- [109] J.D. Smith, R. Dhiman, S. Anand, E. Reza-Garduno, R.E. Cohen, G.H. McKinley, K.K. Varanasi, *Soft Matter*, 9 (2013) 1772-1780.
- [110] T. Someya, T. Sekitani, S. Iba, Y. Kato, H. Kawaguchi, T. Sakurai, *Proc. Natl. Acad. Sci. U. S. A.*, 101 (2004) 9966-9970.
- [111] D.-H. Kim, N. Lu, R. Ma, Y.-S. Kim, R.-H. Kim, S. Wang, J. Wu, S.M. Won, H. Tao, A. Islam, K.J. Yu, T.-i. Kim, R. Chowdhury, M. Ying, L. Xu, M. Li, H.-J. Chung, H. Keum, M. McCormick, P. Liu, Y.-W. Zhang, F.G. Omenetto, Y. Huang, T. Coleman, J.A. Rogers, *Science*, 333 (2011) 838-843.
- [112] Y. Sun, S.E. Thompson, T. Nishida, *J. Appl. Phys.*, 101 (2007) 104503.
- [113] A.A. Barlian, W.-T. Park, J.R. Mallon, A.J. Rastegar, B.L. Pruitt, *Proc. IEEE*, 97 (2009) 513-552.
- [114] R. He, P. Yang, *Nat. Nanotechnol.*, 1 (2006) 42-46.
- [115] J.X. Cao, X.G. Gong, R.Q. Wu, *Phys. Rev. B: Condens. Matter Mater. Phys.*, 75 (2007) 233302.
- [116] W. Wu, L. Wang, Y. Li, F. Zhang, L. Lin, S. Niu, D. Chenet, X. Zhang, Y. Hao, T.F. Heinz, J. Hone, Z.L. Wang, *Nature*, 514 (2014) 470-474.
- [117] E.T. Yu, X.Z. Dang, L.S. Yu, D. Qiao, P.M. Asbeck, S.S. Lau, G.J. Sullivan, K.S. Boutros, J.M. Redwing, *Appl. Phys. Lett.*, 73 (1998) 1880-1882.
- [118] J. Shi, M.B. Starr, X. Wang, *Adv. Mater.*, 24 (2012) 4683-4691.

- [119] S. Hoffmann, F. Östlund, J. Michler, H.J. Fan, M. Zacharias, S.H. Christiansen, C. Ballif, *Nanotechnology*, 18 (2007) 205503.
- [120] P. Li, Q. Liao, S. Yang, X. Bai, Y. Huang, X. Yan, Z. Zhang, S. Liu, P. Lin, Z. Kang, Y. Zhang, *Nano Lett.*, 14 (2014) 480-485.
- [121] W. Han, Y. Zhou, Y. Zhang, C.-Y. Chen, L. Lin, X. Wang, S. Wang, Z.L. Wang, *ACS Nano*, 6 (2012) 3760-3766.
- [122] K.C. Pradel, W. Wu, Y. Zhou, X. Wen, Y. Ding, Z.L. Wang, *Nano Lett.*, 13 (2013) 2647-2653.
- [123] W. Wu, X. Wen, Z.L. Wang, *Science*, 340 (2013) 952-957.
- [124] W. Wu, Y. Wei, Z.L. Wang, *Adv. Mater.*, 22 (2010) 4711-4715.
- [125] W. Wu, Z.L. Wang, *Nano Lett.*, 11 (2011) 2779-2785.
- [126] P. Fei, P.-H. Yeh, J. Zhou, S. Xu, Y. Gao, J. Song, Y. Gu, Y. Huang, Z.L. Wang, *Nano Lett.*, 9 (2009) 3435-3439.
- [127] Y. Hu, B.D.B. Klein, Y. Su, S. Niu, Y. Liu, Z.L. Wang, *Nano Lett.*, 13 (2013) 5026-5032.
- [128] J. Zhou, P. Fei, Y. Gu, W. Mai, Y. Gao, R. Yang, G. Bao, Z.L. Wang, *Nano Lett.*, 8 (2008) 3973-3977.
- [129] M.A. Zimmler, D. Stichtenoth, C. Ronning, W. Yi, V. Narayanamurti, T. Voss, F. Capasso, *Nano Lett.*, 8 (2008) 1695-1699.
- [130] K. Storm, F. Halvardsson, M. Heurlin, D. Lindgren, A. Gustafsson, P.M. Wu, B. Monemar, L. Samuelson, *Nat. Nanotechnol.*, 7 (2012) 718-722.
- [131] L.J. Brillson, Y. Lu, *J. Appl. Phys.*, 109 (2011) 121301.
- [132] W.P. Mason, R.N. Thurston, *J. Acoust. Soc. Am.*, 29 (1957) 1096-1101.
- [133] J.A. Harkey, T.W. Kenny, *J. Microelectromech. Syst.*, 9 (2000) 226-235.
- [134] S.M. Sze, K.K. Ng, *Physics of Semiconductor Devices*, 3rd ed., John Wiley & Sons, New York, 2007.

- [135] Y. Gao, Z.L. Wang, *Nano Lett.*, 9 (2009) 1103-1110.
- [136] I.M. Daniel, O. Ishai, *Engineering Mechanics of Composite Materials* (2nd Edition), in, Oxford University Press, 2006, pp. 58-60.
- [137] H. Nanto, T. Minami, S. Takata, *J. Appl. Phys.*, 60 (1986) 482-484.
- [138] J. Anderson, G.V.d.W. Chris, *Rep. Prog. Phys.*, 72 (2009) 126501.
- [139] X. Xue, Y. Nie, B. He, L. Xing, Y. Zhang, Z.L. Wang, *Nanotechnology*, 24 (2013) 225501.
- [140] Y. Zhao, X. Lai, P. Deng, Y. Nie, Y. Zhang, L. Xing, X. Xue, *Nanotechnology*, 25 (2014) 115502.
- [141] S.R. Morrison, *Sens. Actuators*, 2 (1981) 329-341.
- [142] Y. Hu, L. Lin, Y. Zhang, Z.L. Wang, *Adv. Mater.*, 24 (2012) 110-114.
- [143] R. Schifano, E.V. Monakhov, U. Grossner, B.G. Svensson, *Appl. Phys. Lett.*, 91 (2007) 193507.

APPENDIX

A. MATLAB code for image processing in Chapter 3

A1. Main function (with an Image Processing Toolbox)

```
clear, close all;
a=imread('Slide1.jpg');%%% file name
b=rgb2gray(a);
B=b;
c=imadjust(B);

level=graythresh(c);
bw=im2bw(c,level);

bw2=bwareaopen(bw,80,4);%%% filter parameter
x=edge(bw2);
cc=bwconncomp(bw, 4);
cc2=bwconncomp(bw2, 4);
pangle=[];
rsquare=[];
jj=[];
rs=[];
ii=0;
j=[1:cc2.NumObjects];
cc2.NumObjects
for i=1:cc2.NumObjects
    i
    grain=false(size(bw2));grain(cc2.PixelIdxList{i})=true;
```

```

A=grain;
[row,column]=find(A);
rowp=flipud(row);
p=linortfit2(column,rowp);
angle=atand(p(1));

A2=imrotate(A,45-angle);
[row2,column2]=find(A2);
rowp2=flipud(row2);
p2=polyfit(column2,rowp2,1);

[pp,ss]=polyfit(column2,rowp2,1);
rsquare=[rsquare,1-(ss.normr)^2/(norm(rowp2-mean(rowp2)))^2];

if(rsquare(i)>0.7)
    jj=[jj,ii+1];
    pangle=[pangle,angle];
    ii=ii+1;
    rs=[rs,rsquare(i)];
end
end

xx=-90:1:90;
figure;
subplot(4,2,1),imshow(a),title('original graph');
subplot(4,2,2),imshow(bw2),title('after filter');
subplot(4,2,3),plot(jj,pangle,'o'),ylabel('degree'),xlabel('number of objects'),title('number vs degree scatter plot');

```

```

subplot(4,2,4),histfit(pangle,180),h=get(gca,'Children');set(h(2)
,'FaceColor',[.8 .8 1]),xlabel('degree'),ylabel('number of
objects'),title('degree vs number');
[muhat,sigmahat]=normfit(pangle)
[counts, binValues]=hist(pangle,180);
normalizedCounts=100*counts/sum(counts);
subplot(4,2,[5,6]);
bar(binValues,normalizedCounts,'barwidth',0.5);
title('percentage plot')
xlabel('Input Value');
ylabel('Normalized Count [%]');

subplot(4,2,[7,8]);
mu=muhat;
sigma=sigmahat;
xs=[-80:.1:60];
ys=normpdf(xs,mu,sigma);
plot(xs,ys);
title('normal distribution')
xlabel('angle');
set(gcf,'Position',get(0,'Screensize'));
%%%%%%%%%%%% calculate the percentage
[aa,bb]=size(pangle);
count=0;
for m=1:bb
    if((pangle(m)<=10+muhat)&&(pangle(m)>=muhat-10))
        count=count+1;
    end
end

```

```

end
[aa,bb]=size(pangle);
percent=count/bb

```

A2. Called function 1

```

function [hyperplane_normal,hyperplane_offset]=linortfitn(data)
[M,N]=size(data);
if M<=N,
    error('linortfitn:DegenerateProblem','There are fewer
datapoints than dimensions: the data is perfectly fit by a
hyperplane. ');
end
[U,S,V]=svd(data-repmat(mean(data),M,1),0);
hyperplane_normal=V(:,end);
hyperplane_offset=-mean(data*hyperplane_normal);

```

A3. Called function 2

```

function [p]=linortfit2(xdata,ydata)
if ~isequal(size(xdata),size(ydata))
    error('linortfit2:XYSizeMismatch','X and Y vectors must be
the same size. ');
end
[N,C]=linortfitn([xdata(:) ydata(:)]);
p=-[N(1) C]/N(2);

```